

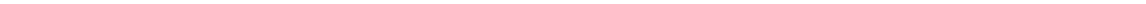
Dissertation
submitted to the
Combined Faculties of the Natural Sciences and
Mathematics
of the Ruperto-Carola-University of Heidelberg, Germany
for the degree of
Doctor of Natural Sciences

Put forward by
Binh Anton Tran
born in: Reutlingen, Germany
Oral examination: June 30, 2022

From Efimov Physics to Polarons in an Ultracold Mixture of Li and Cs Atoms

Referees:

Prof. Dr. Matthias Weidemüller
Prof. Dr. Markus Oberthaler



Abstract

This thesis reports on the reconstruction and improvement of a quantum gas experiment for studying Bose polarons as well as on theoretical investigations at the interface between Efimov physics and Fermi polarons. In both experiment and theory an ultracold mixture of fermionic ${}^6\text{Li}$ and bosonic ${}^{133}\text{Cs}$ with a large mass ratio is considered. With the improved experimental setup we realize Bose-Einstein condensates (BEC) of ${}^{133}\text{Cs}$ with $N = 10^4$ atoms and molecular BECs of ${}^6\text{Li}_2$ with $N = 10^5$ dimers. For the creation of Bose polarons we trap a small number of Li atoms in a tightly confined optical dipole trap and propose a scheme to combine them with the ${}^{133}\text{Cs}$ BEC. In a theoretical study, employing the Born-Oppenheimer approximation, we calculate Efimov bound state energies ($E < 0$) in a three body Cs-Cs-Li system and in a many-body environment where two ${}^{133}\text{Cs}$ atoms are immersed in a Fermi sea of ${}^6\text{Li}$ atoms. In these systems the intraspecies scattering length determine the ground state and the Fermi sea leads to a modification of the binding energies. For the scattering states ($E > 0$) we calculate the induced scattering length between two ${}^{133}\text{Cs}$ atoms mediated by the Fermi sea, and find resonant behavior. We find that for large mass ratios bound states can persist at positive energies to form quasibound states.

Zusammenfassung

Die vorliegende Arbeit beschreibt die Rekonstruktion und Verbesserung eines Quantengas-experiments zur Untersuchung von Bose Polaronen, sowie theoretische Untersuchungen an der Schnittstelle zwischen Efimov Physik und Fermi Polaronen. Hierbei wird ein ultrakaltes Gemisch bestehend aus fermionischen ${}^6\text{Li}$ und bosonischen ${}^{133}\text{Cs}$ Atomen mit großem Massenverhältnis betrachtet. Mit dem verbesserten experimentellen Aufbau ist es möglich Bose-Einstein Kondensate (BEC) aus $N = 10^4$ ${}^{133}\text{Cs}$ Atomen und molekulare BECs aus $N = 10^5$ ${}^6\text{Li}_2$ Molekülen zu erzeugen. Zur Implementierung von Bose Polaronen fangen wir wenige ${}^6\text{Li}$ Atome in einer stark fokussierten optischen Dipolfalle und entwickeln ein Schema zur Mischung von ${}^6\text{Li}$ Atomen mit dem ${}^{133}\text{Cs}$ BEC. Auf der theoretischen Seite verwenden die Born-Oppenheimer Näherung um gebundene Efimov Zustandsenergien ($E > 0$) zu berechnen. Dabei betrachten wir ein Dreikörper Cs-Cs-Li System und ein Vielteilchensystem bestehend aus zwei ${}^{133}\text{Cs}$ Atomen in einem Fermisee aus ${}^6\text{Li}$ Atomen. In diesen Systemen wird der Grundzustand bestimmt durch die Intraspeziesstreuungslänge und der Fermisee führt zu einer Modifikation der Bindungsenergien. Für die Streuzustände ($E > 0$) berechnen wir die durch den Fermisee induzierte Streulänge zwischen zwei ${}^{133}\text{Cs}$ Atomen und finden resonantes Verhalten. Wir stellen fest, dass gebundene Zustände für hohe Massenverhältnisse auch bei positiven Energien als quasi-gebundene Zustände fortbestehen können.

Parts of this thesis are based on the following manuscripts and publications:

- **Fermions Meet Two Bosons—the Heteronuclear Efimov Effect Revisited**
B. Tran, M. Rautenberg, M. Gerken, E. Lippi, B. Zhu, J. Ulmanis, M. Drescher, M. Salmhofer, T. Enss, and M. Weidemüller
Brazilian Journal of Physics (2021) 51:316-322
- **Scattering of two heavy Fermi polarons: Resonances and quasibound states**
T. Enss, B. Tran, M. Rautenberg, M. Gerken, E. Lippi, M. Drescher, B. Zhu, M. Weidemüller, and M. Salmhofer
Physical Review A **102**, 063321 (2020)

The author furthermore contributed to the following publications:

- **Observation of dipolar splittings in high-resolution atom-loss spectroscopy of ^6Li p-wave Feshbach resonances**
M. Gerken, B. Tran, M. Rautenberg, S. Häfner, E. Tiemann, B. Zhu, and M. Weidemüller
Physical Review A **102**, 063321 (2020)
- **Observation of spin-rotation coupling in p-wave Feshbach resonances**
B. Zhu, S. Häfner, B. Tran, M. Gerken, J. Ulmanis, E. Tiemann, and M. Weidemüller
Manuscript in preparation, submitted to Physical Review A.

Contents

1	Introduction	1
2	Experimental setup	5
2.1	Vacuum chamber	6
2.2	Magnetic fields	7
2.3	Laser cooling	10
2.4	Optical dipole traps	15
2.5	Radio-frequency and microwave setup	18
2.6	Diagnostics	23
3	Towards the creation of Bose polarons in a ${}^6\text{Li} - {}^{133}\text{Cs}$ mixture	25
3.1	Low-energy two-body scattering	25
3.2	A Bose-Einstein condensate of ${}^{133}\text{Cs}$	29
3.3	A quantum degenerate gas of ${}^6\text{Li}$	47
3.4	A quantum degenerate ${}^6\text{Li} - {}^{133}\text{Cs}$ mixture	52
4	Fermions meet two bosons - the heteronuclear Efimov effect revisited	61
4.1	The heteronuclear Efimov scenario	62
4.2	Born-Oppenheimer approximation	64
4.3	Two bosons meet one fermion	68
4.4	Two bosons meet the Fermi sea	70
5	Scattering of two heavy Fermi polarons: Resonances and quasibound states	77
5.1	Variable phase method	78
5.2	Efimov spectrum	80
5.3	Scattering phase shift and induced scattering length	81
5.4	Quasibound states	84
6	Conclusions	87

CONTENTS

A Appendix	91
Bibliography	95

Chapter 1

Introduction

The concept of quasiparticles is a powerful tool to reduce the complexity of a many-body problem to the level of single particles. It was first introduced by Landau [Landau, 1933] and Pekar [Pekar, 1946] to describe the motion of an electron in a dielectric crystal lattice. The negative charge of the electron polarizes the surrounding atoms and leads to a lattice deformation which is dragged along the electron's motion. The electron is said to be *dressed* by the surrounding cloud of phonons and forms a *polaron* which is characterized by a modified effective mass and energy compared to the bare electron. The underlying electron-phonon interaction is an important research topic e.g. in transport properties of semiconductors, colossal magnetoresistance or high temperature superconductors [Devreese and Alexandrov, 2009]. More generally, the problem of a particle or impurity in a medium gives rise to a vast number of interesting phenomena ranging from the Kondo effect in metals [Kondo, 1964] to the Higgs mechanism [Higgs, 1964] through which elementary particles in the standard model acquire their mass. Even everyday phenomena such as the formation of raindrops, consisting of a dust particle surrounded by water vapor, can be seen as a classical analogue of dressed particles.

However, even simple theoretical descriptions of polarons such as the Fröhlich model [Fröhlich, 1954] cannot be solved analytically, but rely on approximations. Experimentalists therefore use a complementary approach realized with ultracold quantum gases. The rapid developments in this field after the achievements of Bose-Einstein condensates [Anderson et al., 1995; Davis et al., 1995; Bradley et al., 1995, 1997] and degenerate Fermi gases [DeMarco and Jin, 1999] have opened up new paths to study many-body physics problems with a high degree of control [Bloch et al., 2008]. In particular, the possibility to change the interaction strength between atoms via magnetically tunable Feshbach resonances [Inouye et al., 1998; Courteille et al., 1998] provides access to polarons with strong impurity-medium interactions.

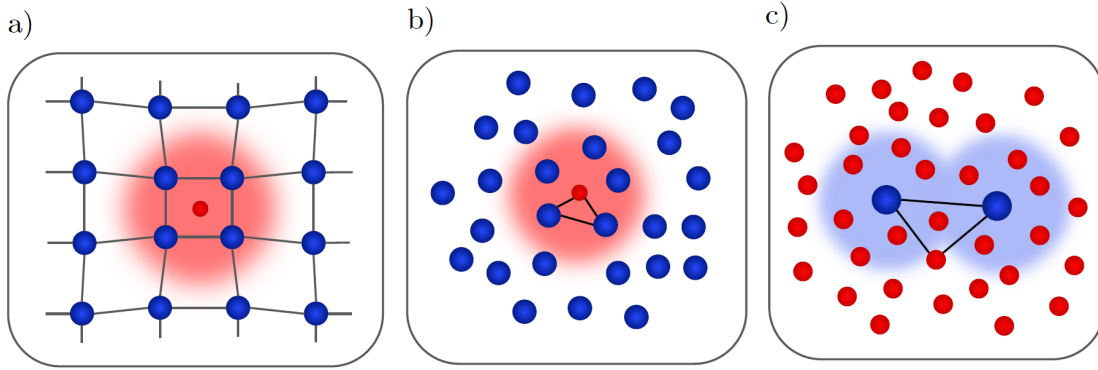


Figure 1.1: Cartoon of polarons in solids and quantum gases. a) Electron (red) moving through a crystal lattice drags along a cloud of surrounding atoms and forms a quasiparticle. b) In a quantum gas a Bose polaron is formed by a ${}^6\text{Li}$ atom (red) dressed by the phonon excitations of a Bose-Einstein condensate of ${}^{133}\text{Cs}$ atoms (blue). Three-body Efimov states become important in a highly mass-imbalanced systems. c) Two Fermi polarons, consisting of two Cs atoms immersed in a Li Fermi sea, can interact via the Fermi sea and form bound states.

Impurities immersed in a degenerate Fermi gas, called Fermi polarons, were first realized in a spin-imbalanced gas of ${}^6\text{Li}$ where spin-down atoms served as impurities in a spin-up Fermi sea [Schirotzek et al., 2009]. The polaron energy was mapped out by means of radio-frequency (RF) spectroscopy showing that the transition frequency between two hyperfine states of the impurity is altered by the presence of the Fermi sea. Since then Fermi polarons have been studied extensively in many experiments [Nascimbène et al., 2009; Kohstall et al., 2012; Koschorreck et al., 2012; Cetina et al., 2016; Scazza et al., 2017; Yan et al., 2019; Ness et al., 2020; Fritsche et al., 2021] and in theory (reviewed in [Massignan et al., 2014; Schmidt et al., 2018]).

On the other hand, Bose polarons, i.e. impurities immersed in a Bose-Einstein condensate (BEC), are more similar to the solid-state polaron. The system of an impurity interacting with the collective phonon excitations of the BEC can be directly mapped onto the Hamiltonian in the Fröhlich model [Tempere et al., 2009]. While earlier experiments realized impurities in a BEC in the weakly interacting regime [Palzer et al., 2009; Catani et al., 2012; Spethmann et al., 2012; Scelle et al., 2013; Rentrop et al., 2016], Bose polarons in the strongly interacting regime have only been realized in 2016 simultaneously by two independent groups [Hu et al., 2016; Jørgensen et al., 2016]. Further spectroscopic measurements in the quantum critical regime [Yan et al., 2020] and experiments on the dynamics of Bose polarons have been performed recently [Skou et al., 2021, 2022]. The experimental progress

also stimulated new theoretical work on the Bose polaron, for which an overview is given in the reviews [Grusdt and Demler, 2015; Scazza et al., 2022].

One key difference between Fermi and Bose polarons lies in their quantum statistics. While the Pauli principle hinders the formation of bound states between identical fermions in the Fermi sea, bound states play an important role for bosons. Especially, the influence of so-called Efimov trimers, a weakly bound three-body state, on the properties of Bose polarons remains one of the open questions which has not been observed so far. Efimov trimers, originally proposed to be observed in nuclear systems [Efimov, 1970], have been created in ultracold quantum gases in homonuclear [Kraemer et al., 2006; Williams et al., 2009; Zaccanti et al., 2009; Gross et al., 2009; Pollack et al., 2009; Knoop et al., 2009; Lompe et al., 2010; Nakajima et al., 2010; Wild et al., 2012] and heteronuclear systems [Barontini et al., 2009, 2010; Bloom et al., 2013; Pires, 2014; Tung et al., 2014]. Theoretical studies [Levinsen et al., 2015; Sun et al., 2017; Sun and Cui, 2017] suggest that for investigating the interplay between few-body Efimov states and many-body Bose polaronic states, systems with a large mass ratio are particularly well suited. In the ${}^6\text{Li} - {}^{133}\text{Cs}$ system, for example, with a mass ratio of $m_{\text{Cs}}/m_{\text{Li}} \approx 22$ the size of some of the Efimov trimers l_T is on the same order as the interparticle distance $n^{-1/3}$ of the BEC giving rise to intriguing few-body correlations in a many-body system. In addition, the ${}^6\text{Li} - {}^{133}\text{Cs}$ system offers magnetically tunable Feshbach resonances [Repp et al., 2013; Tung et al., 2013] which allow for the preparation and detection of the Bose polaron in the strongly interacting regime via RF spectroscopy.

Besides the interplay between few- and many-body physics, interactions between Fermi or Bose polarons induced by the medium remain largely unexplored in current experiments. Important examples of mediated interactions include the occurrence of Cooper pairing responsible for superconductivity or the fundamental interactions where elementary particles serve as mediators. First signatures of polaron-polaron interactions have been observed in [Cetina et al., 2016] and theoretical predictions suggest two Bose polarons to bind to a *bipolaron* due to interactions mediated by BEC phonons [Casteels et al., 2013; Camacho-Guardian et al., 2018]. In Bose-Fermi mixtures fermion-mediated boson interaction have recently been studied in the weakly interacting regime [DeSalvo et al., 2019; Edri et al., 2020; Mukherjee et al., 2020]. Mediated interactions in the strongly interacting regime, however, remain still unobserved.

This thesis investigates topics from Efimov physics to Bose polarons and interactions between Fermi polarons in an ultracold ${}^6\text{Li} - {}^{133}\text{Cs}$ Fermi-Bose mixture. We setup an experimental platform designed for creating Bose polarons in the strongly

interacting regime, studying the interplay between Efimov states and Bose polaron states in the radio-frequency spectrum across a ${}^6\text{Li} - {}^{133}\text{Cs}$ Feshbach resonance. Besides that, in theoretical studies, we investigate the heteronuclear Efimov effect in a three-body Cs-Cs-Li system using the Born-Oppenheimer approximation. We calculate the bound state spectrum with emphasis on the intraspecies interaction. We then study how the bound state spectrum is altered if the two ${}^{133}\text{Cs}$ atoms are embedded in a ${}^6\text{Li}$ Fermi sea. In this scenario, the bound states can be interpreted as bipolaronic states of two Fermi polarons. Finally, we compute the interactions between the two heavy Fermi polarons mediated by the Fermi sea.

The starting point of this thesis work is an existing experiment which enabled studies of the heteronuclear Efimov effect with thermal gases of a ${}^6\text{Li} - {}^{133}\text{Cs}$ mixture [Pires, 2014; Ulmanis et al., 2015, 2016a,b,c; Häfner et al., 2017]. Investigations of polarons in the quantum degenerate regime, however, require the development of new schemes to trap and cool ${}^6\text{Li}$ and ${}^{133}\text{Cs}$ atoms and a major reconstruction of the experiment. We start in Ch. 2 by giving an overview of the existing experimental setup and by describing upgrades and new insights. In Ch. 3, we create a Bose-Einstein condensate of ${}^{133}\text{Cs}$ atoms at a high magnetic field of $B = 895$ G where we can simultaneously tune the interactions between ${}^6\text{Li}$ and ${}^{133}\text{Cs}$ atoms. Moreover, we prepare a gas of ultracold Li atoms in a tightly focused optical dipole trap and propose a scheme to immerse them as impurities in the ${}^{133}\text{Cs}$ BEC. In Ch. 4, we present the calculations of the bound state spectrum of the Cs-Cs-Li system and of two ${}^{133}\text{Cs}$ atoms immersed in a Fermi sea. The interactions between two Fermi polarons mediated by the Fermi sea are calculated in Ch. 5 across a Feshbach resonance. We investigate the occurrence of resonances in the induced scattering length and furthermore study the emergence of quasi-bound states for positive interspecies interactions.

Chapter 2

Experimental setup

In this chapter we describe the experimental setup used for preparing ultracold Bose-Fermi mixtures of ^{133}Cs and ^6Li . We give a short overview of the existing apparatus [Repp, 2013; Pires, 2014; Häfner, 2017] and present new insights and upgrades. A schematic representation of the experimental apparatus is shown in Fig. 2.1. The apparatus can be coarsely divided into six sub-modules each of which is described in one section of this chapter. The experiments take place in the *Vacuum Chamber* around which the apparatus is built. A starting point in ultracold atom experiments is usually the preparation of atoms in a magneto-optical trap (MOT) which requires a combination of *Laser Cooling* and *Magnetic Fields*. Colder and denser atomic

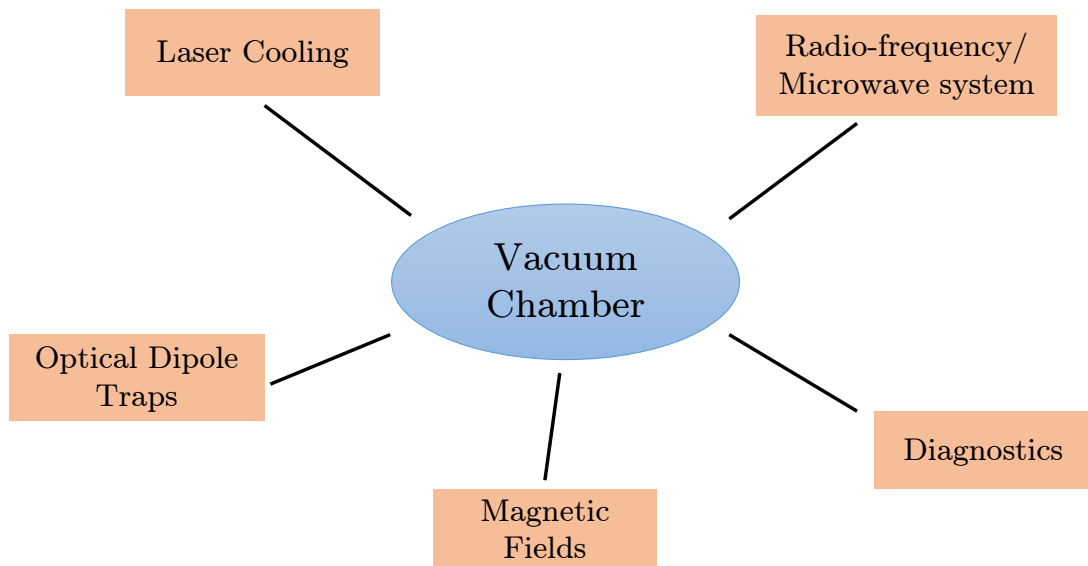


Figure 2.1: Schematic representation of the different sub-systems in our experiment positioned around the main vacuum chamber.

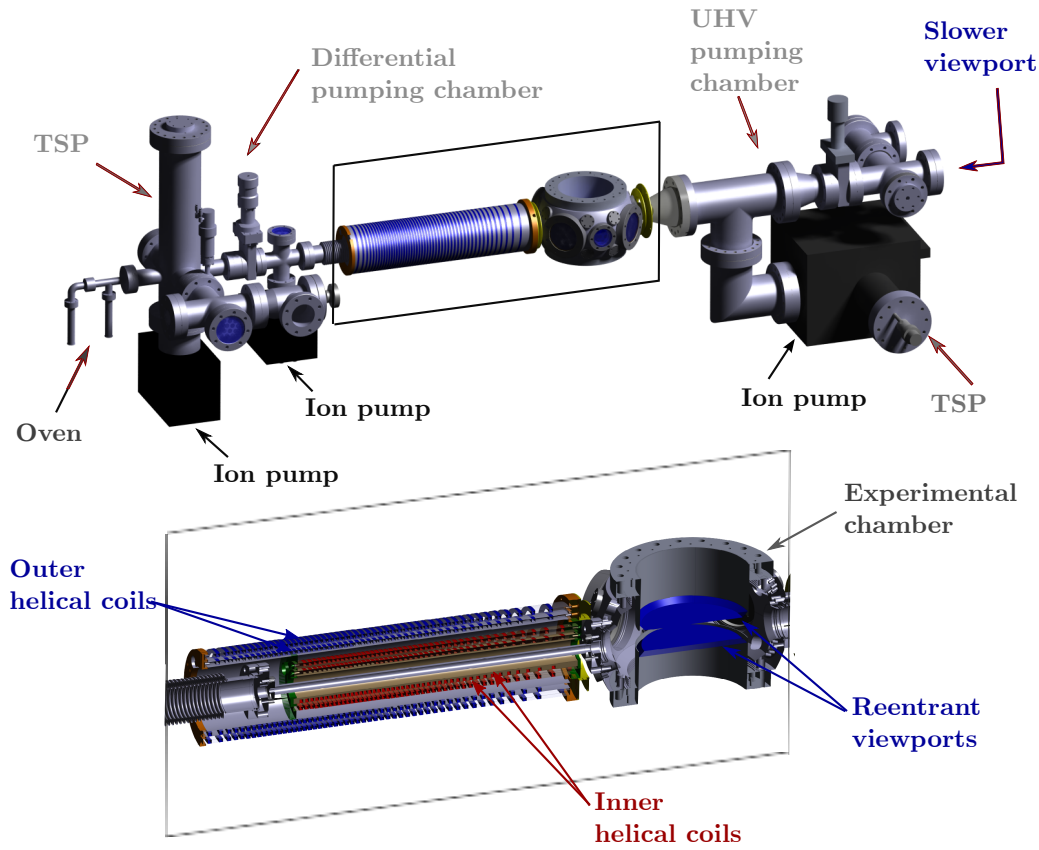


Figure 2.2: Vacuum system. Top: Overview of the whole vacuum system with different pumping chambers. With a combination of ion pumps and titanium sublimation pumps (TSP) an ultra-high vacuum (UHV) with a pressure of $p \sim 10^{-11}$ mbar is achieved in the experimental chamber. Bottom: The double-species Zeeman slower consisting of inner and outer helical coils facilitates subsequent deceleration of both Cs and Li atoms. Figure adapted from [Repp, 2013].

gases are realized in *Optical Dipole Traps* where interactions are tuned via magnetic Feshbach resonances (see Ch. 3.1) and internal spin states can be controlled by a *Radio-frequency/Microwave system*. Information on the trapped atoms such as their density distributions or temperatures is extracted from our *Diagnostics* system.

2.1 Vacuum chamber

The vacuum chamber lies at the heart of the experiment (Fig. 2.2) and is pumped to ultra-high vacuum (UHV) which is necessary to minimize collisions of the trapped, ultracold Li and Cs atoms with the background gas leading to losses. The vacuum

system starts with a double-species oven, similar to the design in [Stan and Ketterle, 2005], in which temperatures of Li and Cs can be controlled independently. Typically temperatures of 633 K (373 K) are used to create vapor pressures of 10^{-5} mbar (10^{-3} mbar) for Li (Cs) [Gehm, 2003; Steck, 2008]. In order to reach lower final pressures the oven section is followed by two differential pumping stages (with diameters $d_1 = 7$ mm, $d_2 = 10$ mm and lengths $l_1 = 103$ mm, $l_2 = 500$ mm), one of which is surrounded by the helical coils of a double-species Zeeman slower. An ion pump is used in this area to lower the pressure. Finally, the main vacuum chamber is connected to the UHV pumping chamber where another ion pump together with a titanium sublimation pump (TSP) realize pressures on the order of $\sim 10^{-11}$ mbar. The vacuum chamber provides optical access through four CF63 and two CF40 viewports as well as a separate CF63 slower viewport in the horizontal plane. The slower viewport is heated to 373 K to avoid deposition of atoms from the atomic beam source which would lower the optical transmission of the viewport. In vertical direction two CF150 reentrant viewports with a small separation of 39 mm allow for high numerical aperture (NA) imaging and dipole trapping.

2.2 Magnetic fields

Magnetic fields are essential for trapping and manipulating Li and Cs atoms. Here we give an overview of the different magnetic fields in our experimental setup and shortly describe their functionality.

- **Double-species Zeeman slower.** The Li and Cs atoms coming from the oven are decelerated by the force of a resonant laser beam in counter-propagating direction through absorption of photons. As the atoms decelerate the change in Doppler shift can be compensated by a spatially varying magnetic field produced by the Zeeman slower [Phillips and Metcalf, 1982]. Since the deceleration is mass dependent the required magnetic field profile along the atomic beam scales as $B(z) \propto \sqrt{1/m}$. For the highly mass-imbalanced Li-Cs system an efficient deceleration is therefore provided by two sets of helical coils (see Fig. 2.2) where the outer set is used for Cs and both sets are used for Li which are loaded subsequently. The detailed characterization of our Zeeman magnetic field profiles can be found in [Repp, 2013]. At the end of the Zeeman slower an adaption coil is implemented to match the field profiles of the Zeeman slower coils to the MOT coils in the experimental chamber.
- **MOT coils.** A quadrupole field is required in a MOT to create a spatially varying Zeeman shift that gives rise to an indirect confinement of an optical molasses through scattering of photons [Raab et al., 1987]. The MOT coils create such gradient fields of $\partial B_{\text{Li}}/\partial z = 31$ G/cm and $\partial B_{\text{Cs}}/\partial z = 9.5$ G/cm

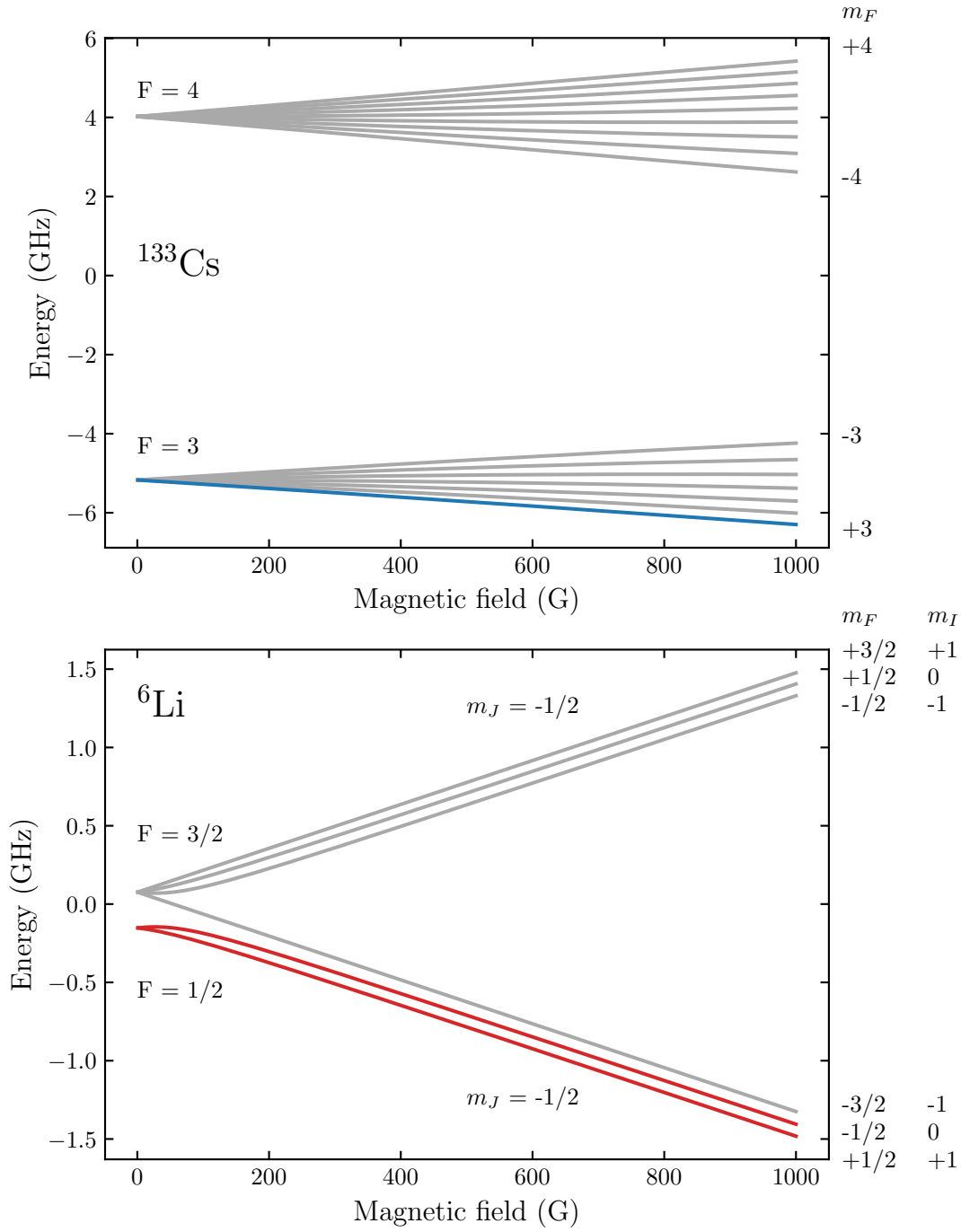


Figure 2.3: Magnetic field dependence of atomic energy levels of ^{133}Cs and ^6Li in their electronic ground state. The quantum number F denotes the total angular momentum with the magnetic quantum number m_F . The magnetic quantum numbers m_I and m_J are associated with the nuclear spin angular momentum and the total electronic angular momentum, respectively. The employed ^{133}Cs (^6Li) states in our experiment are highlighted in blue (red).

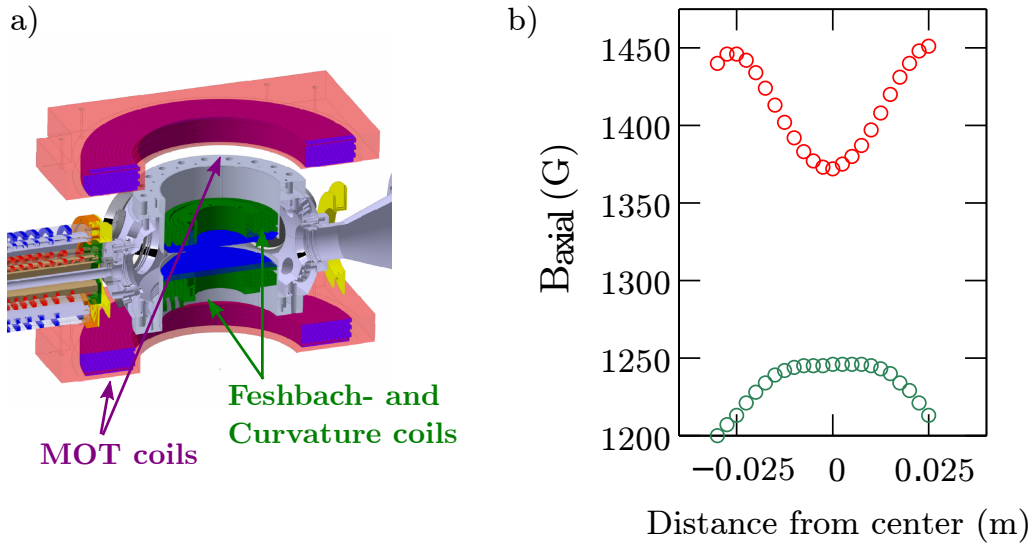


Figure 2.4: Magnetic field coils around the vacuum chamber. a) The Feshbach and curvature coils (green) are placed on top of the reentrant viewports (blue) while the larger MOT coils (violet) are situated around the steel chamber. b) The magnetic field produced by the Feshbach coils has an axial curvature (red) which can be compensated by the curvature coils (green). Figure adapted from [Repp, 2013].

consisting of 6 layers with 12 winding and a minimal radius of 100 mm per coil. The large design, however, causes a large inductance which limits the turn off time together with Eddy currents to > 10 ms. This limitation is problematic for subsequent optical cooling techniques such as degenerate Raman sideband cooling for Cs or gray molasses cooling for Li.

- **Compensation cage.** A large, rectangular cage ($800 \text{ mm} \times 1380 \text{ mm} \times 660 \text{ mm}$) around the vacuum chamber consisting of three pairs of coils provides magnetic fields of up to 2 G in each spatial direction. They are used to compensate the earth magnetic field or other stray magnetic fields e.g. from permanent magnets of the ion pumps.
- **Feshbach coils.** Offset magnetic fields of up to 1400 G are provided by the Feshbach coils to tune the intraspecies (Li-Li, Cs-Cs) and interspecies (Li-Cs) scattering lengths (the scattering length is introduced in Ch. 3) and the hyperfine energy levels according to the Zeeman effect (Fig. 2.3). The 24 windings per coil (four in axial and six in radial direction) are directly placed on the reentrant viewport (Fig. 2.4). Since this geometry deviates from an ideal Helmholtz configuration, the effective magnetic field along the axial direction is given by $B_z = B_0(1 + \alpha z^2)$ with a curvature of $\alpha = 0.0274 \text{ G/cm}$ [Gerken, 2022]. The exact geometry as well as the manufacturing process are described

in [Pires, 2014]. The Feshbach coils are additionally stabilized using a current transducer¹ which is fed into a home-built PID controller. A high stability of the Feshbach coils requires a thermal equilibrium in the experiment and is analyzed in detail in [Ulmanis, 2015]. The resolution is limited to about 20 mG by a 16 bit DAC of the experimental control system.

- **Curvature coils.** The curvature coils are placed inside the Feshbach coils and were originally designed to compensate for the curvature of the Feshbach coils (Fig. 2.4b)). However, the trapped atomic gas is usually not strongly affected by the curvature if placed in the center of the Feshbach coils. For this reason we connect the curvature coils in anti-Helmholtz configuration to produce quadrupole fields. Due to their small size with two layers and two windings per coil, we can make use of faster switching times of 1-2 ms compared to the MOT coils. We therefore typically transfer the atoms from the quadrupole field provided by the MOT coils after loading to the one provided by the curvature coils.
- **Raman coils/Offset coils.** Additional, small offset fields of up to 2 G can be produced in all three spatial directions by these coils. This is useful e.g. for having a small magnetic field with high resolution (< 1 mG) on top of the Feshbach field for mapping out splittings in p-wave Feshbach resonances [Gerken et al., 2019] or for degenerate Raman sideband cooling. The offset fields in the horizontal plane can be used to e.g. spatially shift the center of the quadrupole field.

2.3 Laser cooling

In this section we present some of the basic concepts of our Li and Cs laser cooling setup. The full laser cooling scheme consists of a complex setup of different diode lasers which are frequency-stabilized by spectroscopic methods and frequency shifted by acusto-optic modulators before they are guided to the vacuum chamber via optical fibers across different laser tables. Here we give an overview of the employed Li and Cs frequencies and discuss the cooling technique of degenerate Raman sideband cooling which is necessary in our system to reach Bose-Einstein condensation of Cs.

The level schemes for the D_2 transition for ${}^6\text{Li}$ and ${}^{133}\text{Cs}$ including the employed light frequencies are shown in Fig. 2.5. For Li, the D_2 line is at a wavelength of 670.977 nm and has a natural linewidth of 5.87 MHz [Gehm, 2003]. Since the hyperfine structure in the excited state is unresolved, atoms in the excited state can decay

¹Danfysik Ultrastab 866

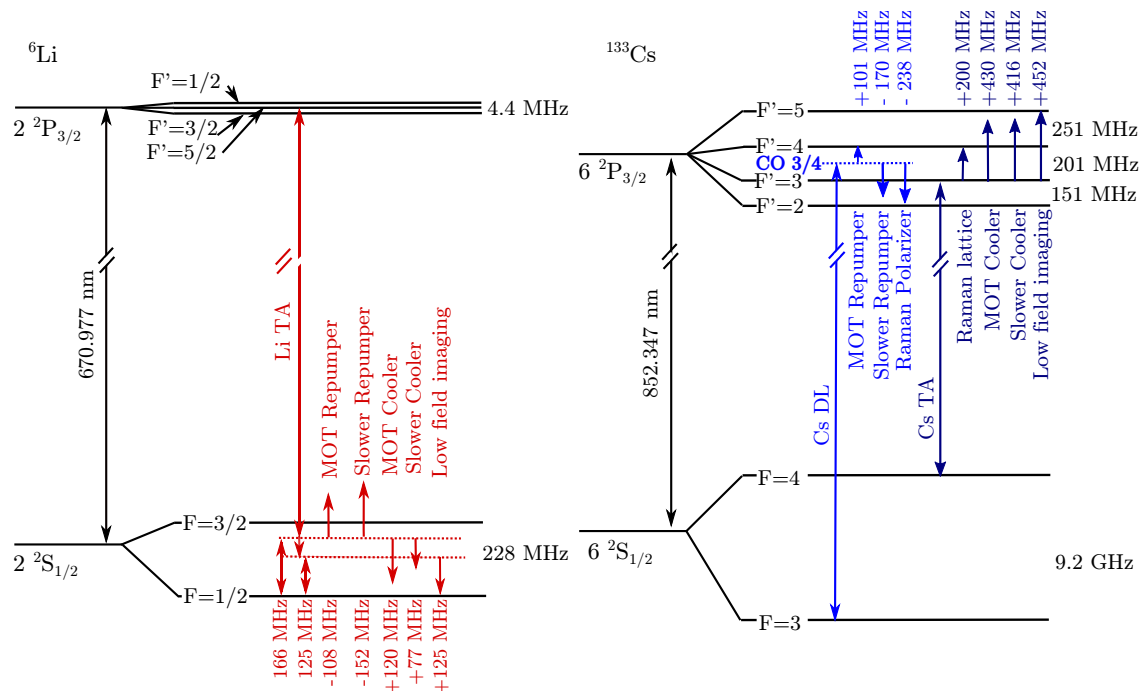


Figure 2.5: Hyperfine structure of the D_2 cooling line for ${}^6\text{Li}$ and ${}^{133}\text{Cs}$. The arrows and the red (blue) numbers mark the laser light frequencies and frequency shifts by the AOMs, respectively. Li TA, Cs DL and Cs TA stand for the diode lasers which are frequency-stabilized. Figure adapted from [Repp, 2013].

into both the $F = 3/2$ and $F = 1/2$ state, requiring repumping light in addition to the cooling light. Also sub-Doppler cooling techniques are less effective due to the unresolved excited state and we use a gray molasses cooling scheme on the D_1 transition instead [Gerken, 2016]. Both the laser light for cooling and trapping Li atoms in the MOT as well as for gray molasses cooling are provided by Toptica TA pro 670 laser systems with a recently upgraded home-built tapered amplifier system (design of S. Whitlock group). With gray-molasses cooling we typically reach temperatures of $T = 42 \mu\text{K}$.

The D_2 line of Cs is at 852.347 nm with a natural linewidth of 5.22 MHz [Steck, 2008]. The 9.2 GHz hyperfine splitting of the ground state is the famous clock transition serving as a time standard for defining the second. Unlike Li, Cs has a resolved excited hyperfine state which allows for efficient sub-Doppler cooling [Drewsen et al., 1994]. Although the $F = 4 \rightarrow F' = 5$ cooling transition is a closed cycling transition, off-resonant coupling can still lead to population in the dark $F = 3$ state, requiring an additional repumping beam. Cooling and repumping light are provided by a Toptica TA pro 850 and a Toptica DL pro 850 laser system, respectively. With sub-Doppler cooling we typically reach temperatures of $T = 8 \mu\text{K}$.

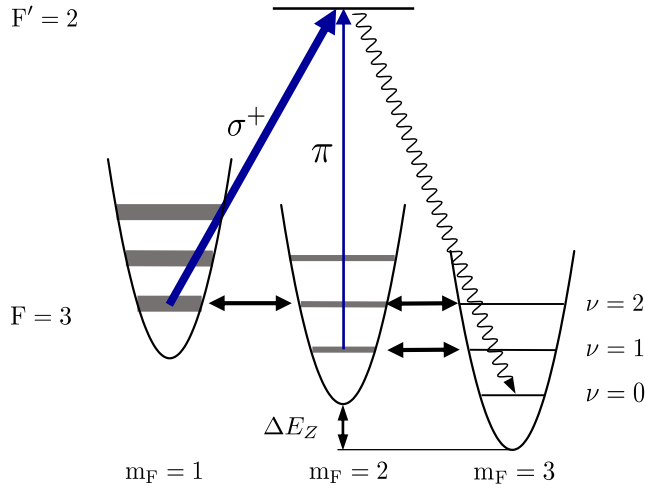


Figure 2.6: Schematics of degenerate Raman sideband cooling. Degenerate vibrational levels are coupled via Raman transitions (double-sided arrows). Optical pumping via the excited $F' = 2$ level transfers atoms into the $|3, 3\rangle$ ground state.

2.3.1 Degenerate Raman sideband cooling of ^{133}Cs

The Cs atoms can be further cooled by the technique of degenerate Raman sideband cooling (dRSC) [Vuletic et al., 1998; Kerman et al., 2000] where our setup follows the one in [Treutlein et al., 2001]. Our full setup is described in [Repp, 2013]. In dRSC the atoms are loaded from the MOT into a 3D optical lattice (Fig. 2.6). The cooling takes place by pumping atoms which are initially in high-lying vibrational states into the vibrational ground state of the $|F = 3, m_F = 3\rangle$ hyperfine sublevel. A small offset magnetic field B_0 leads to a Zeeman splitting $\Delta E_Z = g_F \mu_B B_0$ bringing the states $|F = 3, m_F = 3, \nu\rangle$, $|F = 3, m_F = 2, \nu - 1\rangle$, and $|F = 3, m_F = 1, \nu - 2\rangle$ into degeneracy. These states are coupled to each other by a two-photon Raman transition driven by the lattice light. An additional polarizer beam which is composed of a strong σ^+ - and a weak π -component pumps the atoms from the $6^2S_{1/2}, F = 3$ into the $6^2P_{3/2}, F' = 2$ manifold. The Raman coupling is much faster than the optical pumping by the weak π beam such that atoms are pumped preferably starting from the $m_F = 1$ state. The atoms decay back into the $F = 3$ manifold and maintain their vibrational state since the vibrational energy $\hbar\omega$ is much larger than the photon recoil energy ('Lamb-Dicke regime'). At the end of the cooling, a large part of the atoms are in the $|F = 3, m_F = 3, \nu = 0\rangle$ which is a dark state hindering Raman transitions and optical pumping.

In our setup the Raman lattice light is set on the $|F = 4\rangle \rightarrow |F' = 4\rangle$ transition (see Fig. 2.5) with a red detuning of 9.2 GHz to the $|F = 3\rangle$ manifold. The

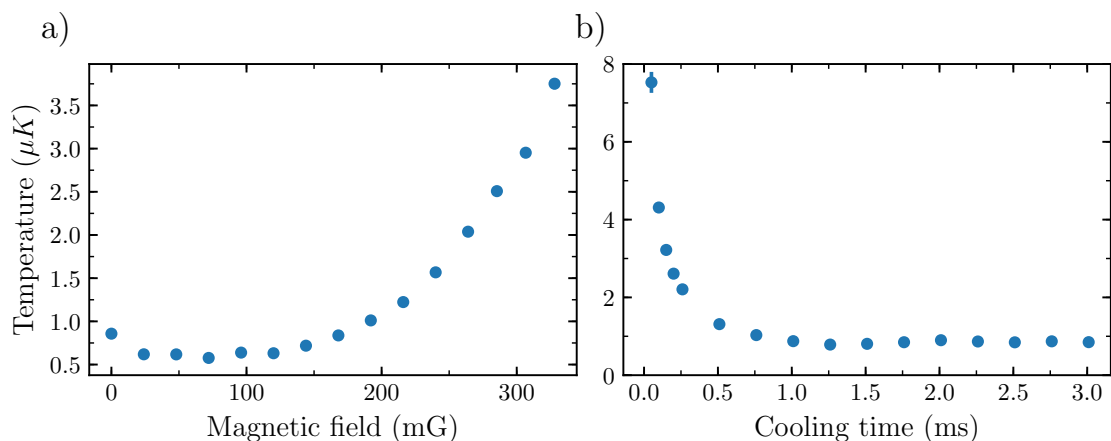


Figure 2.7: Characterization of degenerate Raman sideband cooling. a) The achieved temperature depends on the offset magnetic field determining Zeeman shift and the degeneracy of the vibrational states. b) The cooling time, during which the polarizer beam is turned on, needs to be long enough to account for the Raman transition rate and the optical pumping rate.

light therefore also serves as a repumper for off-resonantly pumped atoms into the $|F = 4\rangle$ manifold. The Raman polarizer beam drives the $|F = 3\rangle \rightarrow |F' = 2\rangle$ transition with a blue detuning of about 10 MHz. The strong σ^+ - and weak π -component are achieved by a small angle of the polarizer beam with respect to the magnetic field axis and can be optimized with a small horizontal magnetic field on top of the vertical offset field B_0 which slightly rotates the quantization axis of the system.

In the following a characterization of our dRSC scheme is presented. In Fig. 2.7a) we investigate the magnetic field dependence on the temperature. We therefore transfer Cs atoms from the MOT with a density of $n = 2 \times 10^{10} \text{cm}^{-3}$ into the Raman lattice and apply a pulse of the polarizer of 1.5 ms. The temperature is extracted by measuring the cloud size after release from the lattice in a time-of-flight expansion (see Sec. 2.6). We read off a minimum of the temperature of $T \approx 0.6 \mu\text{K}$ in a magnetic field range of about $25 \text{mG} \lesssim B \lesssim 125 \text{mG}$. This is in agreement with our estimated value of $B_0 = \hbar\bar{\omega}/g_F\mu_B = 80 \text{mG}$ where we assumed a harmonic lattice with a mean trap frequency of $\bar{\omega} = 2\pi \times 28 \text{kHz}$ based on a peak intensity of $I = 329 \text{mW/cm}^{-2}$ per beam. Power broadening of the vibrational states contribute to the large magnetic field range over which the temperature stays constant. On the other hand the Gaussian intensity distribution of the lattice prevents that the degeneracy condition between the vibrational states is fulfilled at every lattice site. We compensate for this effect by ramping the lattice intensity to a lower value during the cooling process, thereby dynamically changing the trap frequencies. Finally, we note that the required magnetic field is much smaller than the earth magnetic field

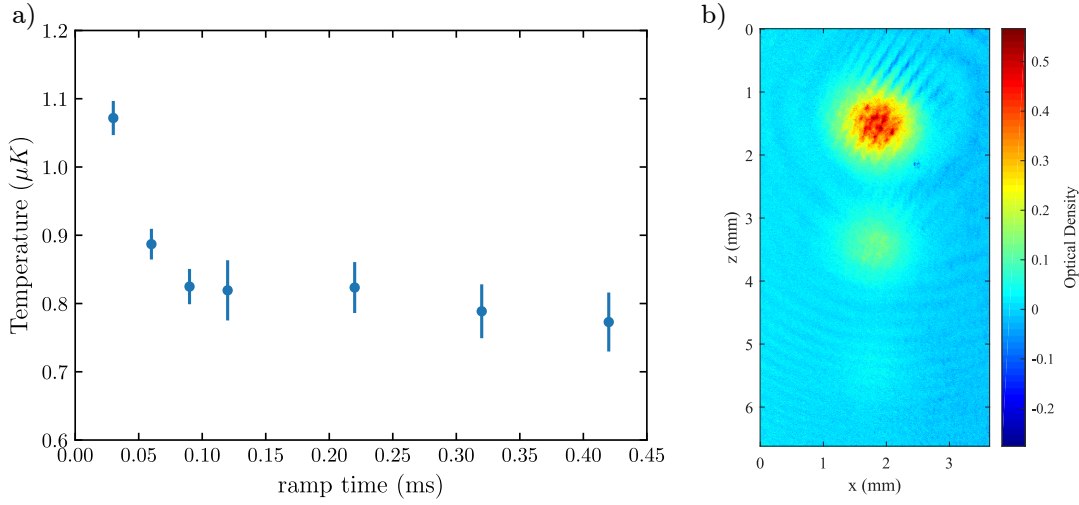


Figure 2.8: Raman sideband cooling lattice release. a) Measured temperature after an adiabatic release of the atoms from the Raman lattice with a linear intensity ramp. b) After release we use a Stern Gerlach separation to find 85 % of the atoms in the $|3, 3\rangle$ state. The two clouds below show atoms in the $|3, 2\rangle$ and $|3, 1\rangle$ state.

of ~ 0.5 G which makes a compensation necessary. A method for calibrating our compensation cage via microwave transitions is presented in Sec. 2.5. Fig. 2.7b) shows the temperature dependence on the total cooling time which denotes the time during which the polarizer beam is turned on. After transfer of the Cs atoms from the MOT we wait for 2 ms for decaying magnetic fields before we turn on the polarizer ($t = 0$). For very short times we recover the temperature that we reach after sub-Doppler cooling of $T < 8 \mu\text{K}$. The minimal temperature is already achieved for cooling times above 1 ms. Since we omit the additional intensity ramp in this measurement for simplicity, the temperature is slightly higher than in Fig. 2.7a). After optical pumping of the Cs atoms low temperatures can be achieved by adiabatically releasing them from the lattice [Kastberg et al., 1995; DePue et al., 1999]. We do this by a linear intensity ramp and find that compared to a sudden release the temperature can be decreased by another $\sim 0.3 \mu\text{K}$ after a ramp time above 0.3 ms (Fig. 2.8). For much longer ramp times the atoms get heated up again due to photon scattering of the lattice light (see (2.3)). Once the atoms are released from the lattice we can quantify the quality of the optical pumping by performing a Stern-Gerlach separation, i.e. spatially separating the m_F states by application of a magnetic field gradient. In this way we find a typical population of 85% in the $m_F = 3$ state, 13% in the $m_F = 2$ state and 2% in the $m_F = 1$ state. In general the performance of dRSC is mainly limited by the density of the sample. While at low densities $n \leq 1 \times 10^{10} \text{ cm}^{-3}$ temperatures close to the recoil limit $T_R = 198 \text{ nK}$

have been achieved in our experiment and in the literature [Kerman et al., 2000], at higher densities reabsorption of photons leads to higher temperatures. At very high densities, $n = (852 \text{ nm}/2)^{-3} \approx 1 \times 10^{13} \text{ cm}^{-3}$ when lattice sites are occupied with more than one atom [DePue et al., 1999; Vuletic et al., 1998], also light-assisted collisions play a role.

2.4 Optical dipole traps

Optical dipole traps work based on dipole forces which create a conservative trapping potential for neutral atoms [Chu et al., 1986]. The form of the potential can be derived from an oscillator model. Following [Grimm et al., 2000] we consider an atom placed into an oscillating electric light field \mathbf{E} which induces an atomic dipole moment \mathbf{p} . This induced dipole moment can again interact with the electric field giving rise to the interaction potential

$$U_{\text{dip}} = -\frac{1}{2} \langle \mathbf{p} \mathbf{E} \rangle = -\frac{1}{2\epsilon_0 c} \Re(\alpha) I. \quad (2.1)$$

where we have used the linear relation between the dipole moment amplitude and the field amplitude $p_0 = \alpha E_0$. Here α denotes the complex polarizability and I is the light intensity which follows a Gaussian function for a focused laser beam. The imaginary part of the polarizability is linked to the absorbed power of the atom P_{abs} and leads to the photon scattering rate

$$\Gamma_{sc}(\mathbf{r}) = \frac{P_{\text{abs}}}{\hbar\omega} = \frac{1}{\hbar\epsilon_0 c} \Im(\alpha) I(\mathbf{r}). \quad (2.2)$$

From the photon scattering rate one can calculate the corresponding heating rate in a three-dimensional harmonic potential via

$$\dot{T} = \frac{1}{3} T_{\text{rec}} \Gamma_{sc} \quad (2.3)$$

where $T_{\text{rec}} = \hbar^2 k^2 / 2m$ is the recoil energy. In Fig. 2.9 we show the real part of the polarizability for Li and Cs and the corresponding heating rate. Our dipole traps operate at a wavelength of 1064 nm which is far detuned from the atomic resonance frequencies where photon scattering is negligible and at the so-called tune-out wavelength for Cs of 880 nm. At this wavelength the polarizability of Cs is zero which enables species-selective trapping of Li [LeBlanc and Thywissen, 2007]. Since this wavelength lies between the D1 and D2 line of Cs it leads to a considerable heating rate which we need to take into account in our Li-Cs mixing scheme.

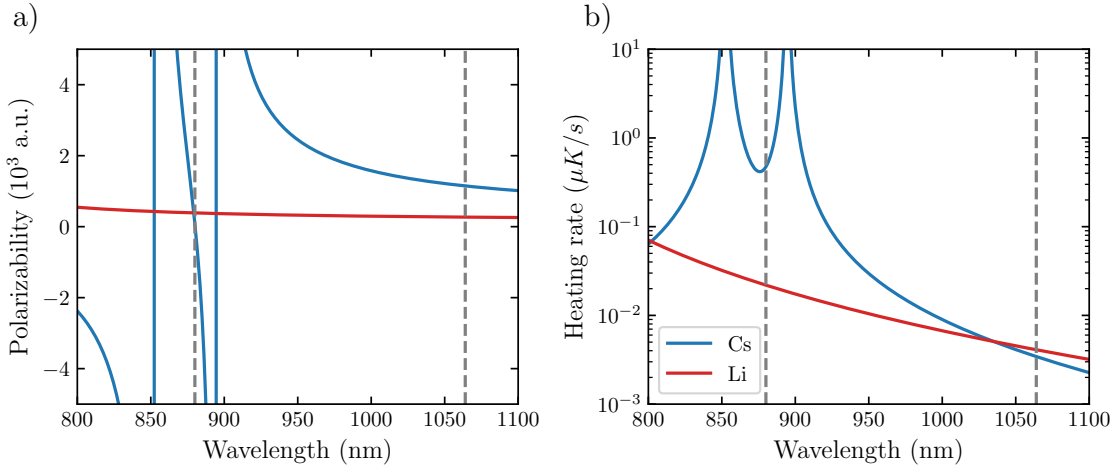


Figure 2.9: a) Real part of the polarizability for Li (red) and Cs (blue). b) Calculated heating rate for a typical microtrap intensity of 10^8 W/m². The vertical dashed lines mark the wavelengths of our dipole traps.

The dipole traps implemented in our setup are schematically shown in Fig. 2.10.

- Reservoir trap.** The reservoir trap is a large volume trap designed to capture a large number of Cs atoms from the Raman lattice at temperatures below $1 \mu\text{K}$ and low densities on the order of 10^{11}cm^{-3} . A Mephisto MOPA laser with 55 W output power is used to focus down a laser beam to a waist of $300 \mu\text{m}$. The beam is deflected behind the chamber and backreflected under a 90° angle which requires a rotation of the linear polarization in order to avoid interference. A piezo mirror allows to translate the trapped atoms in the horizontal plane by about < 1 mm. The full optical setup and its characterization can be found in [Arias, 2014]. A system for intensity stabilization has recently been implemented to suppress heating caused by laser noise.
- Dimple trap.** The dimple trap has two purposes: as the name suggests, it serves as a small volume trap for Cs in the context of the dimple trick (Ch. 3.2.3). Secondly, it was designed to capture Li atoms from a MOT for subsequent evaporative cooling. A 200 W fiber laser (IPG YLR-200-LP-WC) with a wavelength of 1070 nm is focused down to $62 \mu\text{m}$. The beam is reflected under an angle of 8° and forms a cigar-shaped trap. The high power allows to create trap depths of up to 1.2 mK for Li. The complete optical setup can be found in [Heck, 2012]. In the course of this thesis a setup was implemented to dynamically change the trapping volume via frequency modulation of an acousto-optic modulator (AOM) [Neiczer, 2018]. This allows for effective loading of Li atoms after gray molasses cooling. The high power of the laser makes it difficult to stabilize the intensity over the whole range.

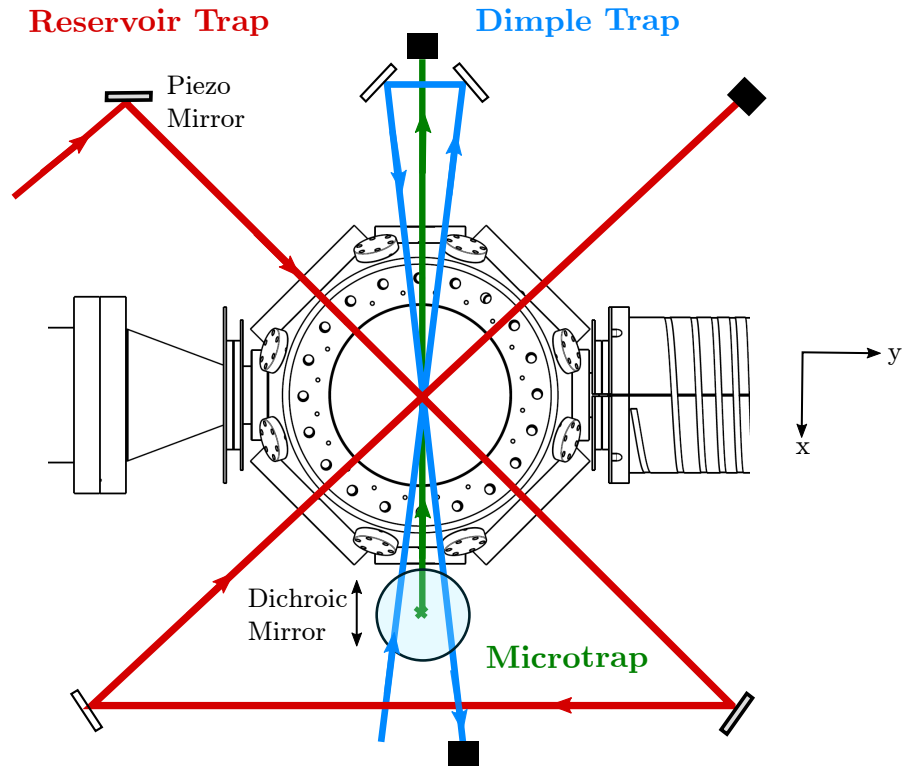


Figure 2.10: Schematic overview of the optical dipole traps.

A new intensity stabilization based on a digital PID controller (Red Pitaya) is implemented to stabilize at low intensities and low gas temperatures where intensity fluctuations become more critical.

- **Microtrap.** For spatially tight confinement of Li atoms within a Cs Bose-Einstein condensate a single-beam trap has been implemented with a beam waist of $10\ \mu\text{m}$ operated at the Cs tune-out wavelength of 880 nm. It is oriented along the symmetry axis of the dimple trap. The laser source is a Ti:sapphire laser (Coherent MBR-110) with a maximum output power of 3 W in the wavelength tunable range of 700 nm to 1030 nm and is intensity stabilized. The microtrap can be translated in z-direction via displacement of a dichroic mirror in a large range of over 13 mm. The full setup of the microtrap is discussed below.

Optical Setup of Microtrap

The microtrap setup is divided onto two tables (Fig. 2.11) which are connected via an optical fiber. The fiber allows for a pure TEM_{00} Gaussian mode and is less

susceptible to beam pointing fluctuations. Finally, the large Ti:sapphire laser system and thermal effects related to dissipation of high intensities are kept far away from the experimental chamber. On the laser table, the output of the laser passes an AOM² which is used for switching and intensity stabilization. The strong, first order of the AOM is directed through a polarizing beam splitter (PBS) to ensure a linear polarization before it reaches the fiber coupler and the polarizing maintaining single-mode³ fiber to the experimental chamber table. The weaker, zeroth order is used as an input for a wavelength meter⁴ which we employ as a reference to tune our laser to the tune-out wavelength.

On the experimental chamber table (Fig. 2.11b)), a fiber coupler⁵ with a focal length of 12 mm outputs a beam with a diameter of $d = 2.1$ mm. A Galilean telescope magnifies the beam with a magnification of $M = |400 \text{ mm}/(-50 \text{ mm})| = 8$ which is focused by a two-inch achromatic lens⁶ with a focal length of 250 mm. Although a high numerical aperture (NA) aspheric lens with small focal length would be the natural choice for a microtrap setup, spatial constraints mainly due to the large MOT coils (see Sec. 2.2) prevent us from their usage. With an off-the-shelf achromatic lens from the Thorlabs AC series we reach a beam waist of $10 \mu\text{m}$ which is small enough for the Li atoms to be trapped within our Cs BEC. We will discuss this aspect further in Ch. 3. Behind the first mirror a photodiode picks up a small fraction of light for intensity stabilization. In front of the chamber a dichroic mirror⁷ mounted on a compact, high-resolution translation stage⁸ reflects the microtrap light while transmitting the dimple trap light. In this way the horizontal move of the translation stage converts into a vertical displacement of the beam over a maximum travel range of 13 mm. Additional fine-tuning of the microtrap focus position can be done via one piezo mirror and the fiber coupler which is mounted into a second piezo mirror holder allowing for adjustment of both the angle and the position of the beam. Moreover, the achromatic lens is placed on a manual translation stage to shift the focal position along the axial direction of the beam.

2.5 Radio-frequency and microwave setup

Radio-frequency (RF) spectroscopy has a wide range of applications in ultracold atom experiments. While early experiments employed RF spectroscopy to map

²Crystal Technology 3100-125

³Thorlabs P3-780PM-FC-10

⁴HighFinesse WS7

⁵Schäfter+Kirchhoff 60FC-4-M12-10

⁶Thorlabs AC508-250-B

⁷Thorlabs DMLP950L

⁸Physik Instrumente Q-545.140

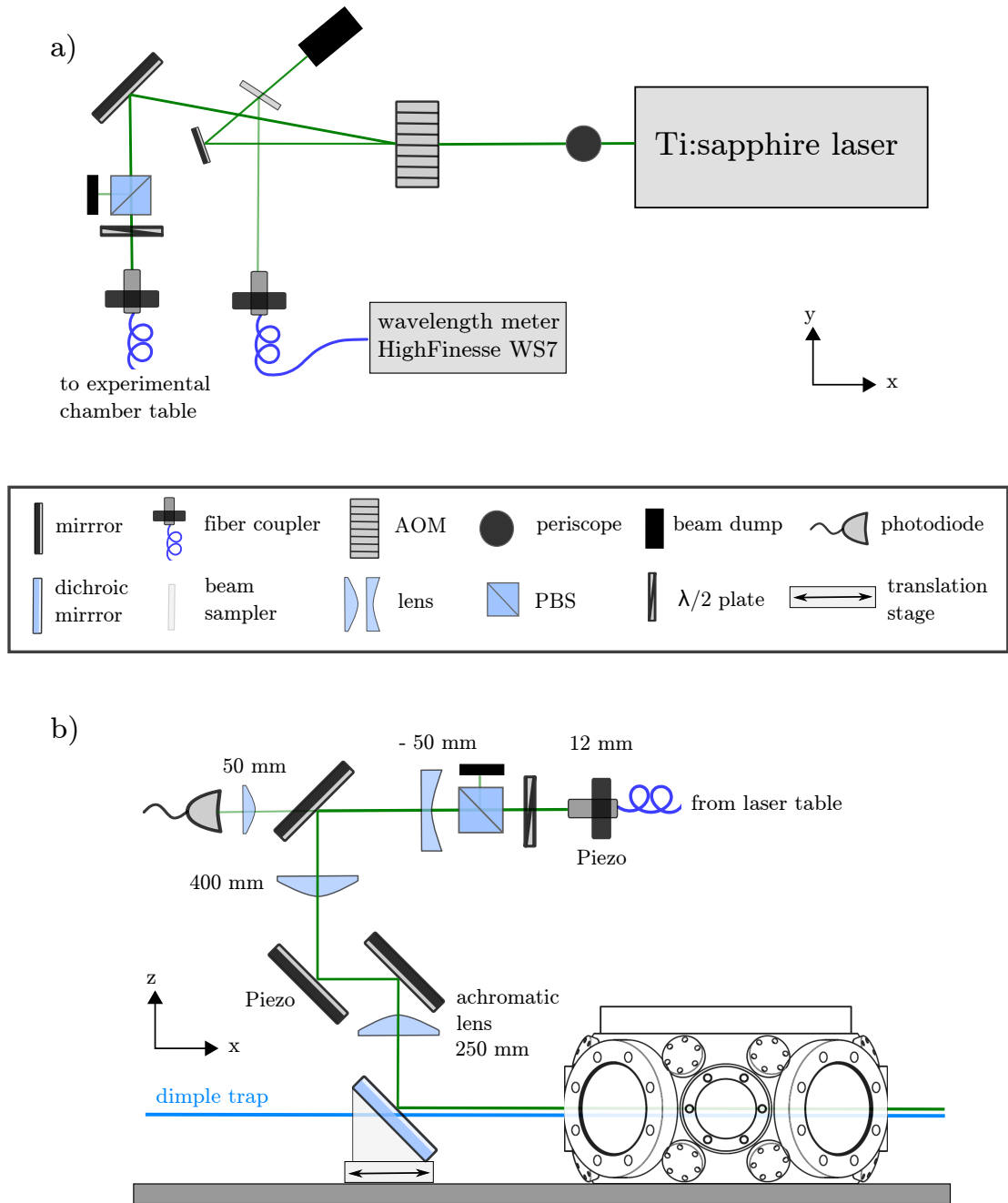


Figure 2.11: Optical setup of the microtrap. a) On the laser table the light is switched and tuned in wavelength before it is coupled through a fiber to the b) experimental chamber table. Here the light is focused by an achromatic lens and the beam can be moved by a motorized translation stage and by piezo mirror holders.

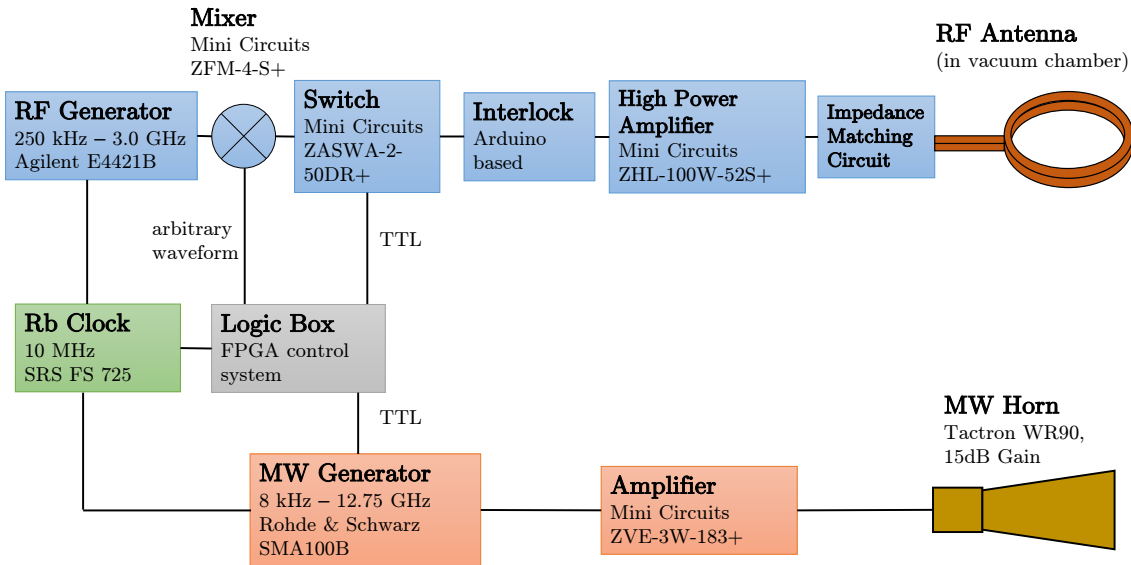


Figure 2.12: Radio-frequency (RF) and microwave (MW) setup for spin manipulation of Li and Cs atoms. The upgraded RF setup includes the possibility to apply arbitrary waveforms and has a 100 W amplifier to drive high frequency Rabi oscillations. An Arduino based interlock prevents the antenna from overheating. In the new MW setup the signal output from the generator is amplified before it is emitted by a horn antenna.

out energy distributions of trapped atoms [Martin et al., 1988], later experiments have measured molecular binding energies [Regal et al., 2003], mean-field interaction energies [Regal and Jin, 2003], or the fermionic pairing gap [Chin et al., 2004a]. Finally, the ground state hyperfine transition in Cs provides the standard of time in atomic clock experiments. In the course of this thesis our radio-frequency (RF) setup for Li has been upgraded and a new setup for driving microwave (MW) transitions for Cs has been implemented. The main motivation for our setups is to probe the properties of polarons via RF spectroscopy and for magnetic field calibration. In the case of the Bose polaron, Li impurities in a Cs bath are driven from the non-interacting $\text{Li}|1\rangle + \text{Cs}|3, 3\rangle$ to the interacting state $\text{Li}|2\rangle + \text{Cs}|3, 3\rangle$ (injection spectroscopy) or vice versa (ejection spectroscopy). The spectral shift $\Delta = \omega_0 - \omega_{\text{RF}}$ between the bare Li transition frequency ω_0 and the altered frequency in the presence of the bath ω_{RF} provides information about the energy of the polaron.

In Fig. 2.12 our setup is presented. For Li (Cs) an RF (MW) generator produces a typical output frequency of 76 MHz (9.2 GHz) which is amplified before it is emitted by a double looped antenna (horn). The pulse duration is controlled by an FPGA control system ('Logic Box') and a Rb clock serves as a 10 MHz reference oscillator to the frequency generator. In the RF setup the Logic Box also provide the

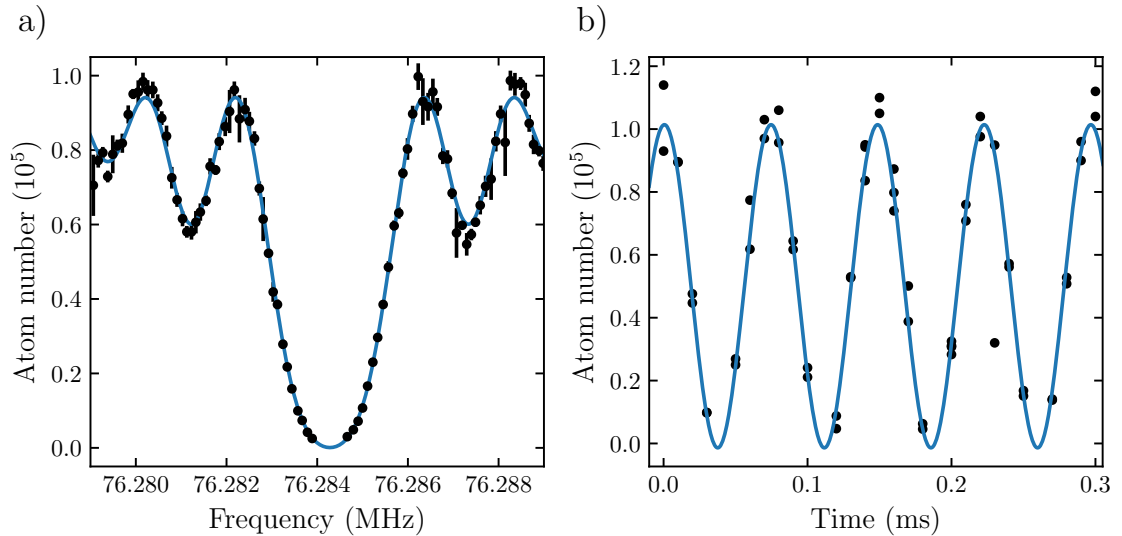


Figure 2.13: Radio-frequency spectroscopy on Li atoms. a) Li atom number in the $|2\rangle$ state after application of a 3π pulse of 0.64 ms duration driving the $\text{Li}|1\rangle \rightarrow \text{Li}|2\rangle$ transition. Data points are averages with standard errors. The solid line is a fit to the data. b) Rabi oscillations with a determined frequency of 13.5(1) kHz from the fit (blue line).

possibility to generate arbitrary waveforms such as Gaussian or Blackman functions in order to suppress sidelobes. For a rectangular pulse these sidelobes are inevitably present since the Fourier-transformed signal follows a *sinc* function. However, the rectangular pulse has the advantage of a smaller width in the frequency domain compared to the other two pulses. A high power $P = 100$ W amplifier is implemented to drive high Rabi frequencies $\Omega \propto \sqrt{P}$ up to 13.5 kHz, similar to frequencies in existing polaron experiments [Kohstall et al., 2012]. An interlock system based on an Arduino microcontroller (for details see [Filzinger, 2018]) protects the antenna from overheating if pulse durations are set too long. The antenna is placed within the vacuum chamber and is connected to an impedance matching circuit to maximize the output power. In Fig. 2.13a) we show a typical $\text{Li}|1\rangle \rightarrow \text{Li}|2\rangle$ spin flip with a pulse duration of 0.64 ms corresponding to a 3π pulse. A Rabi oscillation with maximum Rabi frequency is displayed in Fig. 2.13b).

The Cs MW setup is implemented to drive the transition $F = 3 \rightarrow F = 4$ between the hyperfine ground states. Analogously to the Li setup it could be used in a Fermi polaron experiment to flip Cs impurities in a Li Fermi sea. Another important application of MW spectroscopy is the determination of absolute magnetic fields, e.g. for high resolution Feshbach spectroscopy experiments or for compensation of the earth magnetic field. In the previous section (Sec. 2.3.1) we have seen

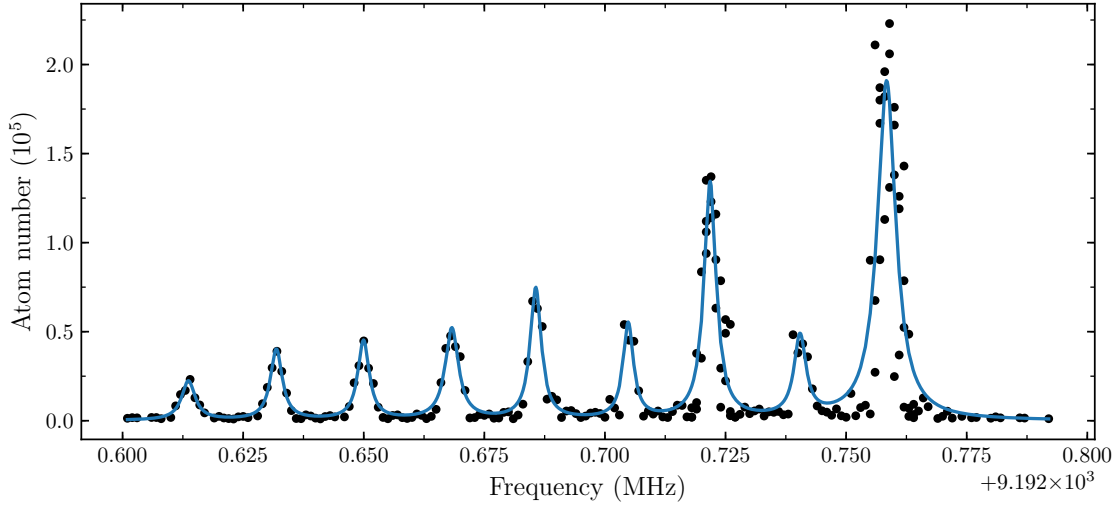


Figure 2.14: Cs microwave spectroscopy. Cs atom number after microwave transfer in the ground state hyperfine transition $F = 3 \rightarrow F = 4$. The blue solid line shows a multi-Lorentzian fit to the data. The outermost right peaks correspond to the transitions $|3, 3\rangle \rightarrow |4, 4\rangle$, $|3, 3\rangle \rightarrow |4, 3\rangle$, etc. From the peak positions we calculate an offset magnetic field of $B = 51(1)$ mG via the Breit-Rabi formula (2.4).

how important a proper compensation of stray magnetic fields is for application of degenerate Raman sideband cooling. Similarly, gray molasses cooling for Li already suffers from small magnetic fields below 1 G [Gerken, 2016]. Fig. 2.14 shows an example of a bad compensation of stray magnetic fields. The data show the transferred atom numbers in the $F = 4$ manifold and the peaks indicate transitions of $|F = 3, m_F\rangle \rightarrow |F = 4, m_F \pm \{0, 1\}\rangle$ due to the Zeeman splitting (see Fig. 2.3). The data is fitted by Lorentzian functions and from the peak positions we infer the absolute magnetic field via the Breit-Rabi formula which can be used across small (Zeeman regime) and high magnetic fields (Paschen Back regime) for the hyperfine ground state manifold [Breit and Rabi, 1931; Steck, 2008]

$$E(B) = -\frac{A_{\text{hfs}}}{4} + g_I \mu_B m B \pm \frac{A_{\text{hfs}}(I + 1/2)}{2} \left(1 + \frac{4mx}{2I + 1} + x^2\right)^{1/2}. \quad (2.4)$$

Here A_{hfs} denotes the hyperfine structure constants and $x = (I+1/2)(g_J - g_I)\mu_B B / A_{\text{hfs}}$ where I and J refer to the nuclear spin and total electron angular momentum, respectively. For the presented data in Fig. 2.14 the magnetic field is determined to be $B = 51(1)$ mG. We compensate this by applying different magnetic fields with our compensation cage in all three spatial directions to find a minimum in the Zeeman splitting, such that the different transitions merge to one peak in the observed atom number.

2.6 Diagnostics

A common technique to extract information on our trapped atoms such as density distributions or temperatures is absorption imaging (see e.g. [Ketterle et al., 1999]). In this destructive technique, atoms are illuminated with resonant laser light and the shadow of the atomic cloud is recorded by a CCD camera. The transmission of the light $T(x, y)$ with incoming (outgoing) intensity I_{in} (I_{out}) through the atomic cloud with a density distribution of $n(x, y, z)$ follows the Beer-Lambert law

$$T(x, y) = \frac{I_{\text{out}}(x, y)}{I_{\text{in}}(x, y)} = e^{-\sigma \int n(x, y, z) dz} \quad (2.5)$$

where σ denotes the absorption cross section. The column density $n(x, y) = \int n(x, y, z) dz$ along the beam direction (which is the line of sight) can then be extracted via

$$n(x, y) = -\frac{1}{\sigma} \log[T(x, y)] =: \frac{1}{\sigma} \text{OD}(x, y) \quad (2.6)$$

with the optical density $\text{OD} := -\log[T(x, y)]$. The atom number and the sizes of the cloud in x- and y-direction can be extracted by fitting a two-dimensional Gaussian function to the column density. Alternatively, since the column density is discretized via the pixels of the CCD chip of size s_x and s_y , we extract the number of atoms simply by summing up over the pixels

$$N = \int n(x, y) dx dy = \frac{s_x s_y}{\sigma} \sum_{\text{pix}} \text{OD}(x, y). \quad (2.7)$$

The temperature of the atomic cloud is determined in a so-called time-of-flight (TOF) expansion. After switching off the trapping potential we study the ballistic expansion and the cloud size $\sigma_{x,y,z}$ after TOF t which follows

$$\sigma_{x,y,z}(t) = \sqrt{\sigma_{x,y,z}^2(t=0) + \frac{k_B T}{m} t^2} \quad (2.8)$$

where we assume that the velocity distribution of the thermal cloud follows a Maxwell-Boltzmann distribution. The temperature T and the initial size $\sigma_{x,y,z}(t=0)$ are thus determined as fit parameters in the above equation. Alternatively, the initial size can be obtained via $\sigma_{x,y,z}(t=0) = \sqrt{2k_B T / m} / \omega_{x,y,z}$ where $\omega_{x,y,z}$ is the trap frequency of a harmonic trap.

In our setup, we use a Ximea MD028MU-SY CCD camera to image in horizontal direction and a AVT Guppy F-038 NIR or an Andor iKon camera in vertical direction. The latter features a fast kinetics mode which allows us to image both Li and

Cs in one experimental run. This is achieved by imaging on a subset of pixels on the CCD chip followed by a quick shift of the charges to an unused subset of pixels. A second picture can then be taken on the first subset before reading out the chip. A high resolution of our imaging setup well below $< 2 \mu\text{m}$ [Filzinger, 2018] allows us to resolve small Bose-Einstein condensates of Cs atoms or small Li impurity density distributions. The full imaging setup can be found in [Renner, 2014; Häfner et al., 2017] with detailed information on noise analysis [Filzinger, 2018] and estimates on resolvable atom numbers [Klaus, 2019; Rautenberg, 2021].

Absorption imaging can be performed at low magnetic fields or high magnetic fields of up to ~ 1000 G. Since the imaging frequencies are shifted due to the Zeeman effect at high magnetic fields, independent Li and Cs diode lasers which are stabilized by an offset lock [Schünemann et al., 1999] to the low field laser are employed (for the setups see [Heck, 2012] for Li and [Schönhals, 2013]). Li at zero magnetic field is imaged on the $F = 1/2$ ground state manifold to the $F' = 1/2, 3/2, 5/2$ excited state manifold which is not resolved. Since the atoms can decay back to the $F = 3/2$ hyperfine state, an additional repumper is used. After the imaging pulse is turned off, the repumper beam is kept on for another few hundred μs in order to optically pump the atoms into the $F = 1/2$ manifold which is the desired state for our Feshbach resonances. At high magnetic fields the two hyperfine sublevels are not degenerate anymore and we can image the different states selectively by directly varying the frequency of the high field imaging laser. If we want to prepare Li atoms in one single spin state we can use the high field light to remove the other state by application of a resonant light pulse.

Cs at low magnetic fields is imaged on the $F = 4 \rightarrow F' = 5$ transition. Since the atoms are prepared in the $F = 3$ state we need to pump them into the $F = 4$ state by what we also refer to as 'repumper' beam. At high magnetic fields two additional lasers provide the imaging and repumper beams for the same transition. The repumper transition can also be driven by the recently implemented microwave setup (Sec. 2.5) which does not suffer from typical problems of optical setups such as power or beam pointing instabilities.

Chapter 3

Towards the creation of Bose polarons in a ${}^6\text{Li} - {}^{133}\text{Cs}$ mixture

In this chapter we present an experimental scheme designed for the realization of Bose polarons, i.e. a system of ${}^6\text{Li}$ impurities immersed in a ${}^{133}\text{Cs}$ Bose-Einstein condensate (BEC). The chapter is structured as follows: a basic theoretical background of two-body scattering at ultracold temperatures is given in Sec. 3.1. We then continue by presenting the realization of the ${}^{133}\text{Cs}$ BEC in Sec. 3.2, the trapping of ${}^6\text{Li}$ impurities in Sec. 3.3, and the mixing scheme of ${}^6\text{Li}$ and ${}^{133}\text{Cs}$ in Sec. 3.4. Each of these sections begins with a summary of the relevant scattering properties of ${}^{133}\text{Cs}$, ${}^6\text{Li}$ and ${}^6\text{Li} - {}^{133}\text{Cs}$ followed by the presentation of the experimental realization and the characterization of the gas.

3.1 Low-energy two-body scattering

One of the major successes of ultracold gas experiments lies in the exquisite control of interactions. At ultralow temperatures scattering properties and two-body interactions are solely governed by the so-called s-wave scattering length a independent of the underlying two-body interaction potentials. The tunability of the scattering length via Feshbach resonances allows for precise control of the strength and sign of the interactions via magnetic fields [Chin et al., 2010]. In the following we introduce the basic concepts of two-body scattering physics which are used throughout the whole thesis including the derivation of the scattering length and the concept of Feshbach resonances.

Two-body scattering

Two-body scattering physics is the subject of many textbooks (e.g. [Merzbacher, 1998; Sakurai, 1993]). In deriving some of the main concepts we closely follow [Dal-

ibard, 1999]. The scattering process of two particles in the center-of-mass reference interacting via the potential $V(\mathbf{r})$ can be described by the Schrödinger equation

$$\left(-\frac{\hbar^2 \nabla^2}{2\mu} + V(\mathbf{r})\right) \psi_{\mathbf{k}}(\mathbf{r}) = E_k \psi_{\mathbf{k}}(\mathbf{r}) \quad (3.1)$$

with the effective mass μ , a positive collisional energy $E_k = \hbar^2 k^2 / 2\mu$ and the relative coordinate \mathbf{r} between the particles. If the interparticle distance $|\mathbf{r}|$ is much larger than the range of interaction r_0 of $V(r)$, i.e. $|\mathbf{r}| \gg r_0$, the solution of the Schrödinger equation reads

$$\psi_{\mathbf{k}}(\mathbf{r}) \sim e^{i\mathbf{k}\mathbf{r}} + f(k, \theta) \frac{e^{ikr}}{r}. \quad (3.2)$$

The solution is a superposition of an incoming plane wave with wavevector k and a scattered spherical wave with scattering amplitude $f(k, \theta)$. The scattering amplitude contains the physics of the collisional process and depends on the angle θ between incident and observation direction. It is related to the scattering cross section σ_k via an integration over the solid angle Ω

$$\sigma_k = \int_{\Omega} |f(k, \theta)|^2 d\Omega. \quad (3.3)$$

For a spherically symmetric potential $V(\mathbf{r}) = V(r)$ the situation can be further simplified to a one-dimensional Schrödinger equation by expanding the wavefunction in spherical harmonics. In this case the scattering amplitude reads

$$f(k, \theta) = \frac{1}{2ik} \sum_{\ell=0}^{\infty} (2\ell + 1) (e^{2i\delta_{\ell}(k)} - 1) P_{\ell}(\cos \theta) \quad (3.4)$$

where $P_{\ell}(x)$ and $\delta_{\ell}(k)$ are the Legendre polynomials and the scattering phase shift between incoming and outgoing wave of partial wave $\ell = 0, 1, 2, \dots (s, p, d, \dots)$, respectively. The scattering cross section is then given as a sum of the partial wave cross sections,

$$\sigma(k) = \sum_{\ell} \sigma_{\ell}(k) \quad \text{with} \quad \sigma_{\ell}(k) = \frac{4\pi}{k^2} (2\ell + 1) \sin^2 \delta_{\ell}(k). \quad (3.5)$$

At ultralow temperatures only s-wave scattering ($\ell = 0$) needs to be considered since collision energies are well below the centrifugal barrier. In this regime the scattering phase shift can be expressed by the equation [Sakurai, 1993]

$$k \cot \delta_{\ell=0}(k) = -\frac{1}{a} + \frac{1}{2} r_0 k^2 + \dots \quad (3.6)$$

which is known as the effective range expansion. To first order, the scattering length is therefore given in the limit of low energies ($k \rightarrow 0$) by

$$a = -\lim_{k \rightarrow 0} \frac{\tan \delta_{\ell=0}(k)}{k}. \quad (3.7)$$

Equivalently, using the effective range expansion, the s-wave cross section can be written as

$$\sigma(k) = \frac{4\pi a^2}{1 + k^2 a^2} \quad (3.8)$$

which in the low-energy limit is simply given by $\sigma_k = 4\pi a^2$. In the unitarity limit ($k^2 a^2 \gg 1$), when the scattering length exceeds the deBroglie wavelength $\lambda \sim k^{-1}$, the cross-section becomes independent of the scattering length $\sigma(k) = 4\pi/k^2$. We note that this cross-section is valid for distinguishable particles. For bosons (identical fermions), it can be shown that, due to the symmetry (antisymmetry) of the wavefunction, the cross-section is enhanced (reduced) to $\sigma(k) = 8\pi a^2/(1 + k^2 a^2)$ ($\sigma(k) = 0$).

Feshbach resonances

The scattering length can be varied via magnetically tunable Feshbach resonances. The topic of magnetically tunable Feshbach resonances is treated in detail in [Mordijk et al., 1995; Timmermans et al., 1999; Köhler et al., 2006; Chin et al., 2010]. Here, we give a basic introduction of the physical picture of Feshbach resonances, closely following [Chin et al., 2010]. Fig. 3.1a) depicts the origin of a Feshbach resonance considering two molecular potentials. The potential denoted by the *open channel* is associated with two free atoms in the limit of large internuclear distances R and is open to scattering events with small collision energies E_{col} close to threshold. The *closed channel* supports bound states close to the open channel threshold. If a molecular bound state in the closed channel and the open channel threshold have different magnetic moments $\delta\mu$, the application of a magnetic field B can lead to a resonant energy of the two states which gives rise to a Feshbach resonance. A weak coupling between the channels, e.g. via hyperfine interactions, can lead to an avoided crossing of the states with two branches and a divergence of the scattering length a . In the vicinity of a Feshbach resonance a can be parametrized and written as a function of the magnetic field (Fig. 3.1b))

$$a(B) = a_{\text{bg}} \left(1 - \frac{\Delta}{B - B_0} \right) \quad (3.9)$$

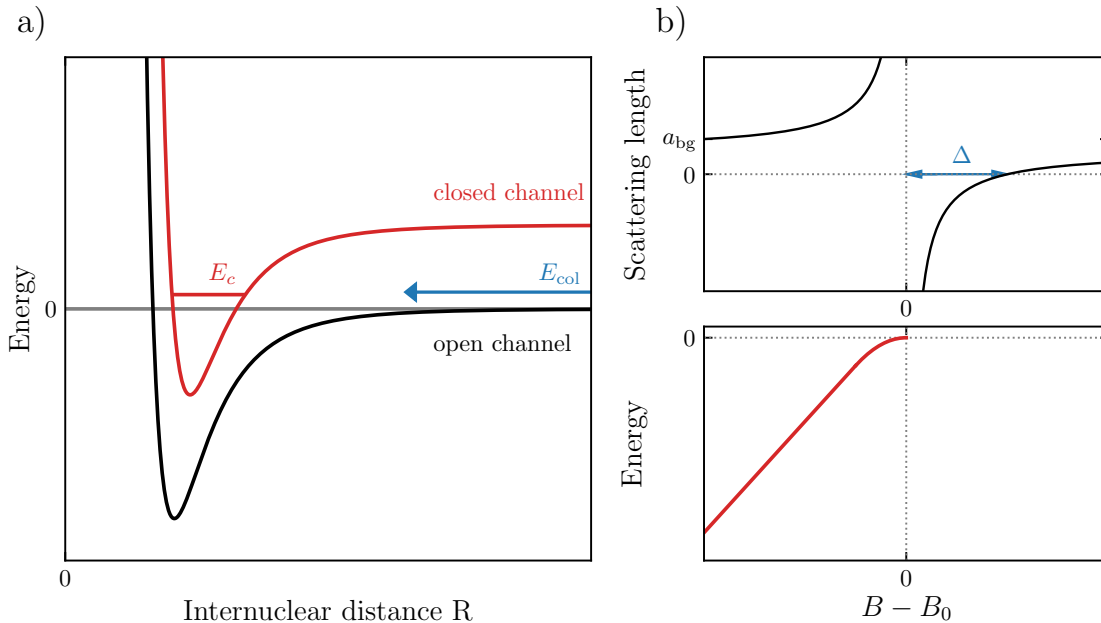


Figure 3.1: Feshbach resonance working principle. a) A Feshbach resonance occurs as the result of the open channel threshold coupling to a weakly bound molecular state with energy E_c in the closed channel. b) Top: The scattering length diverges around the Feshbach resonance position B_0 . Bottom: Close to resonance the molecular binding energy has a quadratic form. Redrawn from [Chin et al., 2010].

where Δ is the resonance width. At the resonance position B_0 the scattering length diverges and displays an attractive ($a < 0$) and repulsive branch ($a > 0$) next to it. The parameter a_{bg} describes the background (off-resonant) scattering length associated with atoms scattering in the open channel. For $B - B_0 < 0$, if the scattering length is very large, i.e. $a \gg r_0$, the energy of the weakly bound molecule takes the form

$$E_b = -\frac{\hbar^2}{2\mu a^2}. \quad (3.10)$$

For smaller a , the binding energy is linear with a slope proportional to the difference in magnetic moment $\delta\mu$. The regime where the binding energy has a quadratic dependence on the scattering length is said to be *universal* since a is the only relevant length scale independent of microscopic details of the potential. The molecules in the universal regime are very weakly bound and represent a special case of halo systems [Köhler et al., 2006]. One of the intriguing properties of halo states is that its wavefunction extends to sizes on the order of the scattering length, far beyond the classical turning point of the potential. Later we will see how the universal

properties of halo dimers become important in the preparation of molecular Bose-Einstein condensates of $^6\text{Li}_2$ (Ch. 3.3) or the understanding of Efimov spectra (Ch. 4).

3.2 A Bose-Einstein condensate of ^{133}Cs

3.2.1 Concepts of Bose-Einstein condensation

We start this section with an introduction on some of the most important concepts of Bose-Einstein condensation with focus on the experimental aspects in harmonic traps which are used throughout this chapter. Beyond the here presented concepts, the theoretical background of Bose-Einstein condensates in dilute atomic gases is subject in textbooks of [Pethick and Smith, 2002] and [Pitaevskii et al., 2003]. A larger experimental perspective is given in lecture notes of [Ketterle et al., 1999].

The nature of Bose-Einstein condensation is based on the quantum statistics of bosons and their wave properties. When the atoms in a gas are cooled down, the thermal deBroglie wavelength, which is the length scale associated with their wave packet extent, increases via

$$\lambda_{\text{dB}} = \frac{h}{\sqrt{2\pi m k_B T}}. \quad (3.11)$$

When λ_{dB} is on the order of the interparticle spacing $n^{-1/3}$ the wave packets start to overlap and a phase transition to a Bose-Einstein condensate can occur. In this case the phase-space density (PSD)

$$\Gamma = n\lambda_{\text{dB}}^3 \quad (3.12)$$

reaches unity (1.02 for a harmonic trap) and is used to characterize the transition. To calculate the critical temperature where the transition occurs we start by considering non-interacting bosons. The mean occupation number of particles in the single-particle state i is given by

$$n_i = \frac{1}{e^{(\epsilon_i - \mu)/k_B T} - 1} \xrightarrow{\text{high T}} e^{(\mu - \epsilon_i)/k_B T} \quad (3.13)$$

where the chemical potential μ is fixed by the conservation of the total atom number $N = \sum_i n_i$. At high temperatures, the mean occupation number follows a Boltzmann distribution and is much smaller than unity which implies that the chemical potential μ must be smaller than the ground state energy ϵ_0 . For decreasing temperatures the chemical potential rises with the mean occupation number, but can never exceed ϵ_0

since this would lead to an unphysical occupation number. As this condition limits the maximum value of the occupation number, conservation of atom number dictates that the atoms which are not in the excited states must occupy one ground state giving rise to Bose-Einstein condensation. In a three-dimensional harmonic trap of the form $U(\mathbf{r}) = \sum_{i=1}^3 1/2m\omega_{x_i}^2 x_i^2$ the number of atoms in the excited, thermal states can be summed up via

$$N_T = \sum_{n_x n_y n_z \neq 0} = \frac{1}{e^{(\epsilon_i - \mu)/k_B T} - 1} \quad (3.14)$$

where n_x, n_y, n_z are the quantum numbers associated with the harmonic oscillator eigenenergies. With the conditions $\mu = \epsilon_0$ and $N_T = N$ the critical temperature can be calculated as [Pitaevskii et al., 2003]

$$k_B T_c = \hbar \bar{\omega} \left(\frac{N}{\zeta(3)} \right)^{1/3} \approx 0.94 \hbar \bar{\omega} N^{1/3} \quad (3.15)$$

where $\zeta(x)$ is the Riemann function and $\bar{\omega} = (\omega_x \omega_y \omega_z)^{1/3}$ denotes the mean trap frequency. With the conservation of atom number $N = N_0 + N_T$ we also find the condensed fraction given by

$$f_c = \frac{N_0}{N} = 1 - \left(\frac{T}{T_c} \right)^3. \quad (3.16)$$

Bose-Einstein condensates can be characterized by analysis of their density distributions. For introducing density distributions, we consider BECs in harmonic traps at zero temperature. We start with the Gross-Pitaevskii equation (GPE) for the order parameter $\psi(\mathbf{r})$ describing the many-body ground state. The stationary GPE reads

$$\left(-\frac{\hbar^2 \nabla^2}{2m} + U(\mathbf{r}) + g |\psi(\mathbf{r})|^2 \right) \psi(\mathbf{r}) = \mu \psi(\mathbf{r}) \quad (3.17)$$

where the coupling constant $g = 4\pi \hbar^2 a/m$ accounts for weak two-body interactions and the density can be related to $n_c(\mathbf{r}) = |\psi(\mathbf{r})|^2$. In the Thomas-Fermi limit, when $gn \gg \hbar \omega_{x,y,z}$, we neglect the kinetic energy term in the GPE and the density becomes

$$n_c(\mathbf{r}) = \max \left(\frac{\mu - U(\mathbf{r})}{g}, 0 \right). \quad (3.18)$$

mimicking the shape of the trapping potential. For a harmonic trap this leads to the

well-known inverted parabola density profile. In an experiment it is often necessary to characterize only partly condensed clouds superimposed with a thermal part, giving rise to a bimodal distribution. The bimodal density distribution can in this case be expressed by [Ketterle et al., 1999]

$$n_{\text{tot}}(\mathbf{r}) = n_{\text{th}} g_{3/2} \left(\prod_{i=1}^3 e^{-x_i/x_{i,th,0}^2} \right) + n_c \max \left(1 - \sum_{i=1}^3 \frac{x_i^2}{x_{i,c,0}^2}, 0 \right) \quad (3.19)$$

where $g_p(x)$ is the polylogarithmic function and the initial sizes of the thermal and condensed cloud are given by $x_{i,th,0} = \sqrt{\hbar/m\omega_i}$ and $x_{i,c,0} = \sqrt{2\mu/m\omega_i^2}$, respectively. The first term follows a Gaussian distribution for thermal gases and the second term follows the functional form of (3.18). From fitting the amplitudes n_{th} and n_c we can extract the condensed fraction. A slightly modified version of (3.19) to fit our absorption images accounts for two-dimensional column densities (see Ch. 2.6).

3.2.2 Scattering properties of ^{133}Cs

Before the realization of the first BECs in the 90s with Rb [Anderson et al., 1995], Na [Davis et al., 1995] and ^7Li [Bradley et al., 1995, 1997], employing evaporative cooling in magnetic traps, Cs was considered a promising candidate to make it first [Tiesinga et al., 1992]. The heavy Cs atom with its large hyperfine splitting possessed ideal requirements for laser cooling, and measurements of its scattering properties revealed feasible elastic cross sections [Monroe et al., 1993]. However, first attempts in realizing Cs BECs in magnetic traps in the $|F = 4, m_F = 4\rangle$ state [Söding et al., 1998; Arlt et al., 1998] suffered from unexpectedly high two-body inelastic collisions due to spin-dipole relaxation ruling out condensation for this particular spin state. In the publication [Guery-Odelin et al., 1998] with the title "Is Bose-Einstein condensation of atomic cesium possible?" the authors eventually shifted their experimental focus to the lower hyperfine level, i.e. the $|3, -3\rangle$ state in which dipolar relaxation rates were, however, still too high (also investigated by the Oxford group [Hopkins et al., 2000]).

The solution around the inelastic two-body collisions lied in the employment of the lowest hyperfine sub-level state $|3, 3\rangle$ which is, however, not magnetically trappable and requires an optical approach. In the $|3, 3\rangle$ state, the Cs atoms can not decay into lower-lying states anymore in a two-body collision and the limitation in the lifetime is given by three-body recombination processes. In a three-body loss process two atoms form a dimer and 2/3 of the released binding energy is distributed on the atom and 1/3 on the molecule. Since the binding energy usually exceeds the trap depth, this will lead to a loss process. After performing Feshbach spectroscopy [Chin et al., 2000] and mapping out three-body losses [Weber et al., 2003a], the Innsbruck group realized the first BEC of Cs in 2003 [Weber et al., 2003b] at a

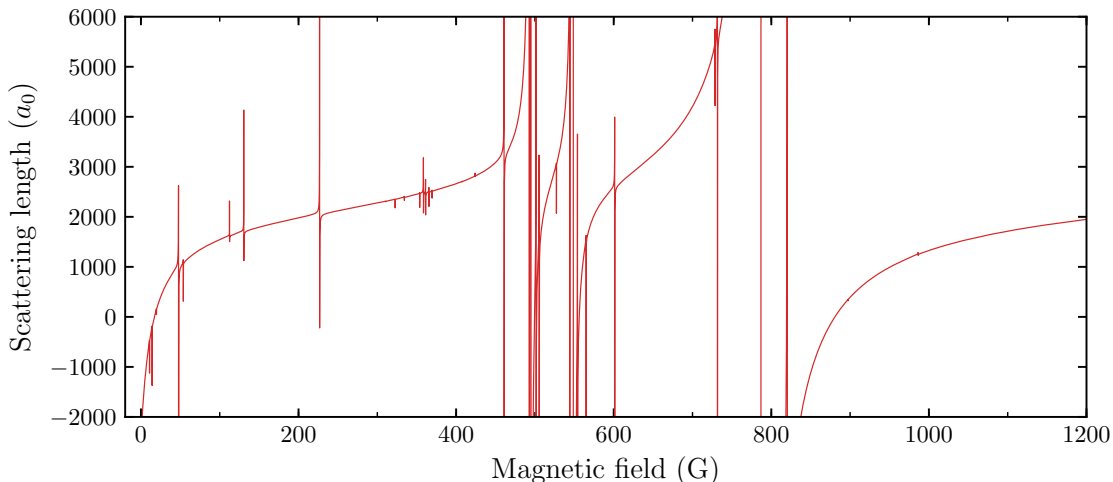


Figure 3.2: Cs-Cs scattering length as a function of the applied magnetic field including s-, d-, and g-wave resonances. The three broad s-wave resonances are centered around -12 G, 549 G, and 787 G. Data taken from [Berninger et al., 2013].

magnetic field around 21 G. Later Cs BECs at this magnetic field have also been realized in our group [Pires, 2014]. The creation of stable Cs BECs requires small repulsive interactions for which the three broad s-wave Feshbach resonances centered around -12 G, 549 G and 787 G (see Fig. 3.2) are generally suitable [Berninger et al., 2013]. In the following we want to discuss the role of losses, in particular of three-body losses, and our strategy to create BECs at high magnetic fields around 900 G where we can simultaneously tune the Cs-Cs and the Li-Cs interactions. The atomic density of trapped Cs atoms in the $|3, 3\rangle$ state follows the differential equation

$$\frac{dn}{dt} = -\tau^{-1}n(t) - L_3n^3(t) \quad (3.20)$$

where τ and L_3 are the one-body $1/e$ lifetime and the three-body recombination rate, respectively. One-body losses can for example happen by collisions of atoms with the background gas and are governed by e.g. the quality of the vacuum or by the photon scattering rate. Also technical noise from the laser or the magnetic fields can contribute to a shorter lifetime [Savard et al., 1997; He et al., 2011]. In our system (Fig. 3.3) we map out the one-body lifetime by holding a thermalized Cs gas in the reservoir trap at a zero-crossing of the scattering length around $B = 880$ G. Thermalization has been achieved by holding the gas at $B = 900$ G for 500 ms before jumping to the target magnetic field of $B = 880$ G. At this magnetic field the three-body recombination rate L_3 is negligible and densities in (3.20) can be integrated to obtain atom numbers. By fitting an exponential function to the data we extract a

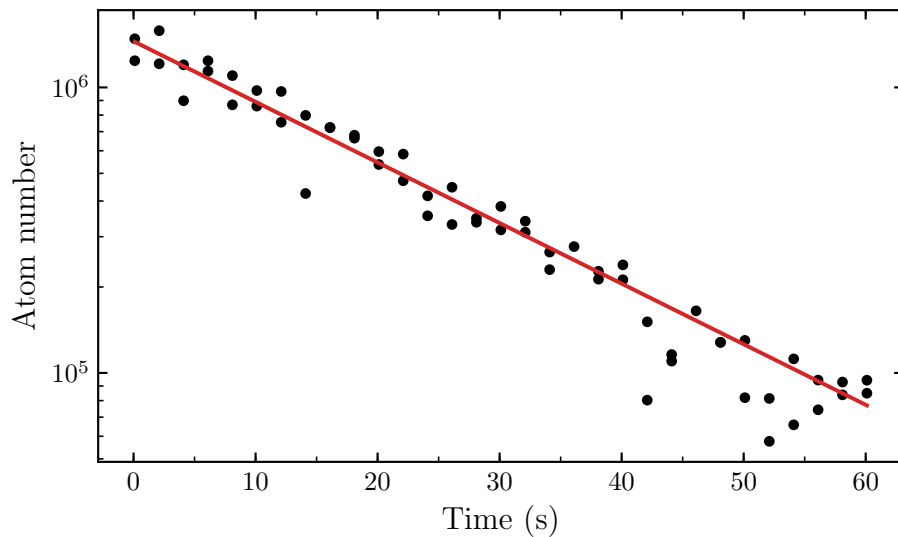


Figure 3.3: Atom number of a thermalized Cs gas held at $B = 880$ G at the zero-crossing of the scattering length. From an exponential fit (red line) to the data a $1/e$ lifetime of $\tau = 20.4(8)$ s is extracted.

one-body lifetime of $\tau = 20.4(8)$ s. On the other hand, the three-body recombination rate was studied theoretically [Esry et al., 1999; Bedaque et al., 2000; Braaten and Hammer, 2001, 2006] and experimentally [Weber et al., 2003a; Kraemer et al., 2006] and can be written as

$$L_3 = 3 C(a) \frac{\hbar}{m} a^4 \quad (3.21)$$

for large positive or negative scattering lengths ($|a| \gg r_0$). Besides the simple a^4 dependence the log-periodic function $C(a)$ leads to loss minima (maxima) for $a > 0$ ($a < 0$) caused by quantum interference and shape resonance effects based on Efimov physics [Esry et al., 1999; Esry and Greene, 2006]. In effective field theory it can be written as [Braaten and Hammer, 2006]

$$C(a) = \begin{cases} 4590 \frac{\sinh(2\eta_-)}{\sin^2[s_0 \log(a/a_-) + \sinh^2 \eta_-]}, & a < 0 \\ 67.1 e^{-2\eta_+} \sin^2[s_0 \log(a/a_+) + \sinh^2 \eta_+] + 16.8(1 - e^{-4\eta_+}), & a > 0 \end{cases} \quad (3.22)$$

where $s_0 \approx 1.00624$ is connected to the Efimov scaling factor $\lambda = e^{\pi/s_0} = 22.7$. The parameters a_+/a_- and η_+/η_- are related to the Efimov resonance positions and lifetimes, respectively. They have been extracted for the different Cs s-wave Feshbach resonances in [Kraemer et al., 2006; Berninger et al., 2011] by fits to the experimental data. A three-body loss minimum at $B = 21$ G, corresponding to a scattering length of $a_+ = 210 a_0$ (see Fig. 3.4), opened up the possibility of effective

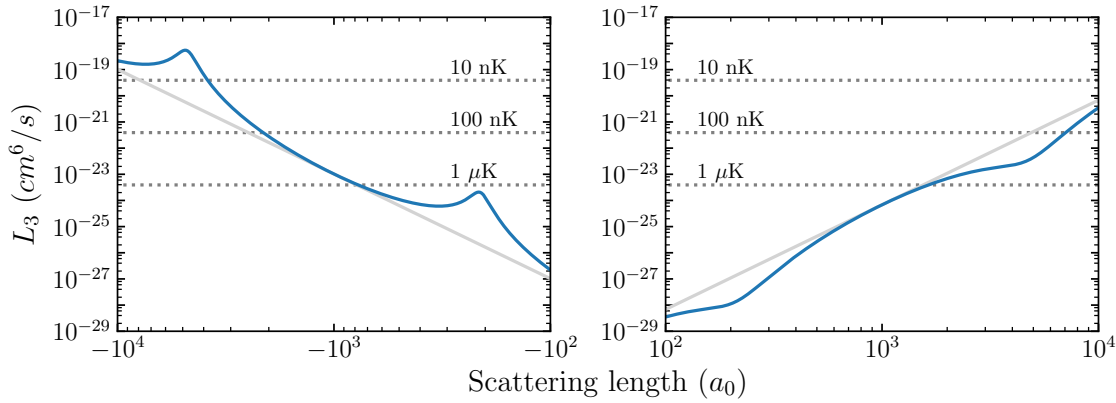


Figure 3.4: Calculated Cs three-body recombination rate (blue line) from effective field theory according to (3.21) with parameters $\eta_- = \eta_+ = 0.10$ and $a_- = a_+ = 210 a_0$ taken from [Berninger et al., 2011]. The lower and upper bounds (grey lines) show the a^4 scaling and are obtained by setting the \sin^2 terms to 1. Dashed lines mark the temperature dependent unitarity limit.

evaporative cooling and was key in achieving the first Cs BEC. Analogously, a three-body loss minimum was also found at a high magnetic field of $B = 893$ G or $a_+ = 270 a_0$.

When working at finite temperatures, the three-body loss rate saturates in the unitarity limit when the scattering length is on the order of the thermal deBroglie wavelength $a \sim \lambda_{\text{dB}}$. In this limit the three-body loss rate follows a T^{-2} scaling which can be expressed via [Rem et al., 2013]

$$L_3 \approx \frac{\hbar^5}{m} 36\sqrt{3}\pi^2 \frac{1 - e^{-4\eta_*}}{(k_B T^2)} \quad (3.23)$$

where η_* is the so-called Efimov inelasticity parameter. The value of this parameter differs for different Cs Feshbach resonances [Eismann et al., 2016] and in Fig. 3.4 we set $\eta_* = \infty$ to omit the details of Efimov physics and calculate an upper bound. We see that for our experimentally relevant temperature regimes the unitarity limit will not play any role below scattering lengths of about $a \sim 1500 a_0$.

For effective evaporative cooling we need to go a scattering length where the elastic collision rate ('good collisions') is high while keeping inelastic collisions ('bad collisions') low. The ratio of good to bad collisions is defined as

$$R = \frac{\Gamma_{\text{el}}}{\Gamma_{3\text{B}} + \Gamma_{1\text{B}}} \quad (3.24)$$

where $\Gamma_{3\text{B}} = n^2 L_3$ and $\Gamma_{1\text{B}} = 1/\tau$ are the three-body and the one-body loss rates, respectively. The elastic collision rate is given by $\Gamma_{\text{el}} = n\sigma\bar{v}$ with the elastic cross

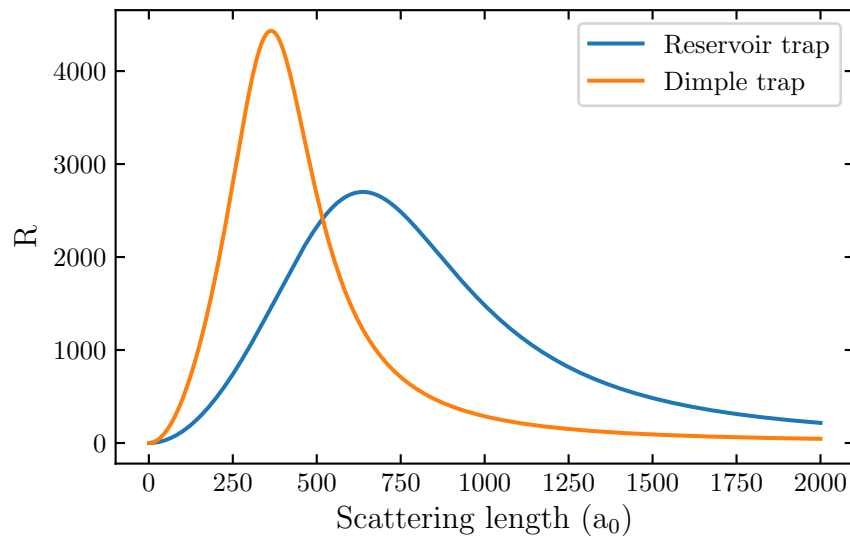


Figure 3.5: Ratio of good to bad collisions. The ratio shows maxima well below scattering lengths of $1000 a_0$ for typical reservoir trap (blue, $n = 5 \times 10^{11} \text{ cm}^{-3}$, $T = 1 \mu\text{K}$) and dimple trap parameters (orange, $n = 3 \times 10^{12} \text{ cm}^{-3}$ and $T = 400 \text{ nK}$).

section σ for bosons (3.8) and the mean relative velocity $\bar{v} = 4\sqrt{k_B T / \pi m}$. For typical densities and temperatures in the reservoir and in the dimple trap the ratio of good to bad collisions is plotted in Fig. 3.5. While in both traps scattering lengths well below $1000 a_0$ lead to a maximum in R , the higher densities in the dimple trap require smaller scattering lengths around $\sim 350 a_0$.

3.2.3 Experimental Realization

With the understanding of the scattering properties of ^{133}Cs we now turn to the experimental realization of the BEC at high magnetic fields. We give a detailed description of its preparation starting from the loading process of Cs atoms into the reservoir trap after laser cooling. Afterwards, we characterize the performance of the dimple trick, a technique to enhance the local phase-space density, in our system and describe the evaporative cooling process to reach condensation.

Loading of Cs atoms into Reservoir Trap

In order to avoid high densities leading to three-body losses we start by loading Cs atoms into a large volume, magnetically levitated reservoir trap after they have been laser-cooled via dRSC (see Sec. 2.3.1). Magnetic levitation means that we apply a magnetic field gradient with the curvature coils to counteract gravity which has a large influence on the trapping potential of the heavy Cs atoms. Additionally,

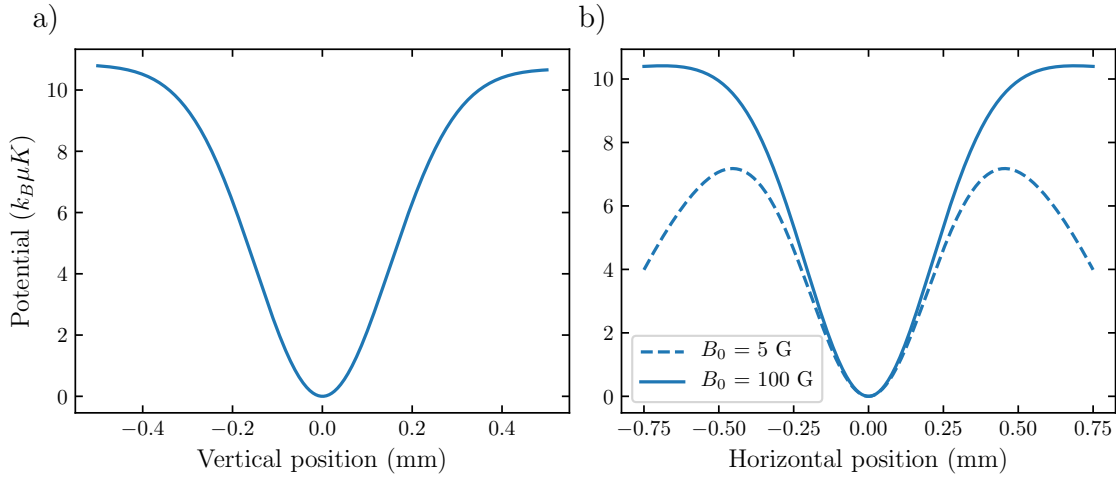


Figure 3.6: Trapping potential of Cs atoms with magnetically levitated reservoir trap. a) In vertical direction the magnetic levitation compensates for gravity entirely, while in horizontal direction b) anti-trapping occurs requiring an offset magnetic field B_0 .

magnetic levitation serves as a filter to obtain a pure sample of Cs atoms in the $|3, 3\rangle$ ground state since the magnetic potential of the unwanted fraction of atoms in the $|3, 2\rangle$ and $|3, 1\rangle$ is too weak to be held. This filtering process is important to exclude inelastic two-body losses. Finally, magnetic levitation allows to create larger trapping volumes compared to an all-optical approach.

We shall have a look how the magnetic levitation determines the trapping potential. The total potential reads

$$U_{\text{tot}}(\mathbf{r}) = U_{\text{dip}}(\mathbf{r}) + U_{\text{grav}}(\mathbf{r}) + U_{\text{mag}}(\mathbf{r}) \quad (3.25)$$

where $U_{\text{dip}}(\mathbf{r})$ is the potential created by the dipole force (2.1) and $U_{\text{grav}}(\mathbf{r}) = m_{\text{Cs}}gz$ is the gravitational potential with the Cs mass m_{Cs} and the gravitational constant g . The magnetic potential can be expressed as

$$U_{\text{mag}}(\mathbf{r}) = -\boldsymbol{\mu} \cdot \mathbf{B}(\mathbf{r}) = -m_F g_F \mu_B B \quad (3.26)$$

where $\mu = m_F g_F \mu_B$ is the absolute value of the magnetic moment with the Bohr magneton μ_B and $g_F = -1/4$ for the $|3, 3\rangle$ state. The last step in the equation holds under the assumption that the atoms follow the magnetic field axis adiabatically, i.e. if the Larmor frequency of the atoms is large compared to the rotation axis of the magnetic field which is fulfilled in our system. The total magnetic field is composed of an offset field in z -direction $B_0(1 + \alpha z^2)$ with a small curvature α (see

Sec. 2.2) and a gradient field $\partial B/\partial z =: \partial_z B$. Using Maxwell's equations $\nabla \cdot \mathbf{B} = 0$ and $\nabla \times \mathbf{B} = 0$ one finds

$$\begin{aligned} \mathbf{B}(\mathbf{r}) = & - \left(\frac{\partial_z B}{2} + \alpha B_0 z \right) x \mathbf{e}_x - \left(\frac{\partial_z B}{2} + \alpha B_0 z \right) y \mathbf{e}_y \\ & + \left[B_0 + \partial_z B + \alpha B_0 \left(z^2 - \frac{x^2 + y^2}{2} \right) \right] \mathbf{e}_z. \end{aligned} \quad (3.27)$$

We see that the atoms experience a magnetic field gradient with opposite sign in x- and y-direction which leads to so-called anti-trapping (Fig. 3.6) while gravity is compensated in z-direction. In the harmonic approximation we Taylor expand (3.26) to obtain the radial and axial magnetic trap frequencies

$$\omega_\rho = \sqrt{\frac{\mu}{4mB_0} (\partial_z B^2 - 4\alpha B_0^2)} \quad \text{and} \quad \omega_z = \sqrt{\frac{2\mu\alpha B_0}{m}}, \quad (3.28)$$

respectively. With a curvature of $\alpha = 0.0274 \text{ G/cm}$ [Gerken, 2022] and a levitation gradient for Cs of $\partial_z B = 31 \text{ G/cm}$ we find that an offset magnetic field of $B_0 = 94 \text{ G}$ is necessary to turn the anti-trapping into a trapping potential.

For an efficient transfer of the Cs atoms into the reservoir trap after degenerate Raman sideband cooling we need to switch on the magnetic fields fast (offset and gradient fields) in order to avoid a long free fall under gravity of the atoms and to compensate for anti-trapping. We determine turn-on times of the magnetic fields by implementing current transducers¹ to dynamically measure the currents flowing through the coils. The currents are provided by commercial power supplies² and can be switched by MOSFETS. In an ideal RL circuit with effective resistance R and inductance L the current follows a simple exponential rise

$$I(t) = \frac{V_0}{R} (1 - e^{-t/\tau}) \quad (3.29)$$

where V_0 and $\tau = L/R$ are the applied voltage and the $1/e$ time constant, respectively. For our curvature coils the time constant is determined to be $\tau = 0.8 \text{ ms}$ [Freund, 2019] and cannot be tuned easily without a redesign of the coils. Instead, we initially apply the maximum voltage provided by the power supply to profit from a large amplitude of the exponential rise followed by a limitation of the voltage in order to reach the desired set value of the magnetic fields. In Fig. 3.7a) we demonstrate the turn-on process for a magnetic field of $B_0 \approx 200 \text{ G}$ and a corresponding levitation gradient of $\partial_z B = 30 \text{ G/cm}$. By limiting the voltage after around 1 ms

¹Danfysik Ultrastab 666

²Delta SM15-400 and TDK Lambda Gen8-400

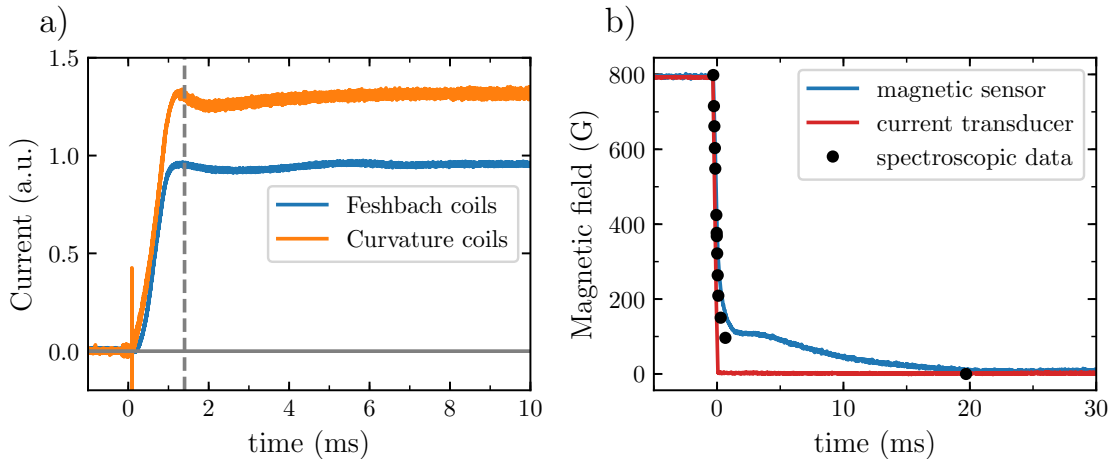


Figure 3.7: Magnetic field switching times. a) Turn-on time of offset magnetic field (Feshbach coils) and magnetic field gradient (Curvature coils). The applied voltage is first maximized and then limited (dashed line) in order to achieve fast turn-on times (see text). b) Turn-off times of the offset magnetic field measured by a current transducer (red), a magnetic sensor (blue) and by performing optical spectroscopy (black points). Turn-off times are limited by Eddy currents.

(dashed line) we achieve rise times of $t_{10\%-90\%} \approx 0.7$ ms. The small overshoot of the current depends on the time of voltage limitation and results in a short overlevitation which might even be beneficial to compensate for the free fall of the atoms. On the other hand, turn-off times of our magnetic fields are considerably longer due to Eddy currents induced in e.g. the steel chamber (Fig. 3.7b)). The long decay of the magnetic field prevents us from applying additional, fast cycles of degenerate Raman sideband cooling (see Ch. 2.3.1) which helps in recapturing and recooling highly energetic atoms in the reservoir trap.

With the presented scheme we load up to $N = 8 \times 10^6$ atoms at a temperature of $T = 1.8 \mu\text{K}$ considering 2s of loading time into the MOT yielding a transfer efficiency of about 20%. We note that longer MOT loading times barely increase the atom number in the reservoir trap due to limited densities in the MOT. Higher transfer efficiencies can therefore only be achieved by larger trap volumes, e.g. by increasing the beam waist of the reservoir trap.

Dimple trick

After having loaded Cs atoms into the reservoir trap, we need to find a way to increase the phase-space density to unity in order to reach condensation. In standard evaporative cooling techniques [Ketterle and Druten, 1996] the phase-space density is

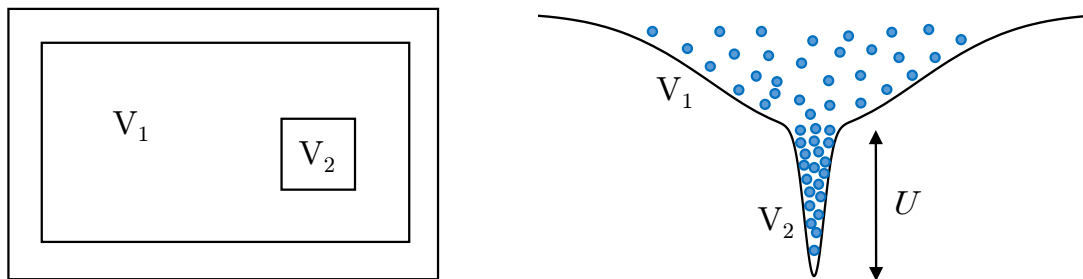


Figure 3.8: Illustration of the dimple trick. In analogy with a two-box model of volumes V_1 and V_2 in an isolated environment (left) in the canonical ensemble, the dimple trick can be modeled in a system with two dipole traps consisting of a large reservoir trap and a small dimple trap with trap depth U .

increased by sacrificing hot atoms which leave the trap. This principle can, however, result in inefficient evaporation for atomic species with a low ratio of good-to-bad collisions such as Cs (see Sec. 3.2.2). In [Pinkse et al., 1997] it was shown that for a collisional gas an adiabatic change of the trap shape can lead to a gain in phase-space density without any loss of atoms and is therefore even reversible. Yet, this technique is limited to phase-space density gains of about 20 and has led to the development of the dimple trick [Stamper-Kurn et al., 1998] where factors of up to 50 in a local subspace of atoms have been reached. As pointed out by the authors, the dimple trick can be seen as an equivalent to a simple box model in a canonical ensemble (Fig. 3.8). An isolated box with volume $V_0 = V_1 + V_2$ and phase-space density Γ_0 where the small volume V_2 (dimple) is adiabatically lowered to a well depth U . Through thermal contact with the reservoir V_1 the atoms equilibrate to the temperature T_f and the density in V_2 increases by the Boltzmann factor $e^{U/k_B T_f}$. The local phase-space density gain in V_2 can be calculated as

$$\log \Gamma_2 / \Gamma_0 = \frac{U/k_B T_f}{1 + (V_2/V_1)e^{U/k_B T_f}} \quad (3.30)$$

and is thus largely determined by the relative ratio of the two volumes V_2/V_1 . Although in theory one can reach arbitrarily large gains in phase-space densities by increasing the volume ratio, in practice one is limited by several factors. Small dimple volumes result in large three-body losses while large reservoir volumes (and ratios) are limited by thermalization times between reservoir and dimple as well as by available laser powers.

We will now experimentally characterize how well the dimple trick works in our system and compare it to a refined model taking into account harmonic potentials.

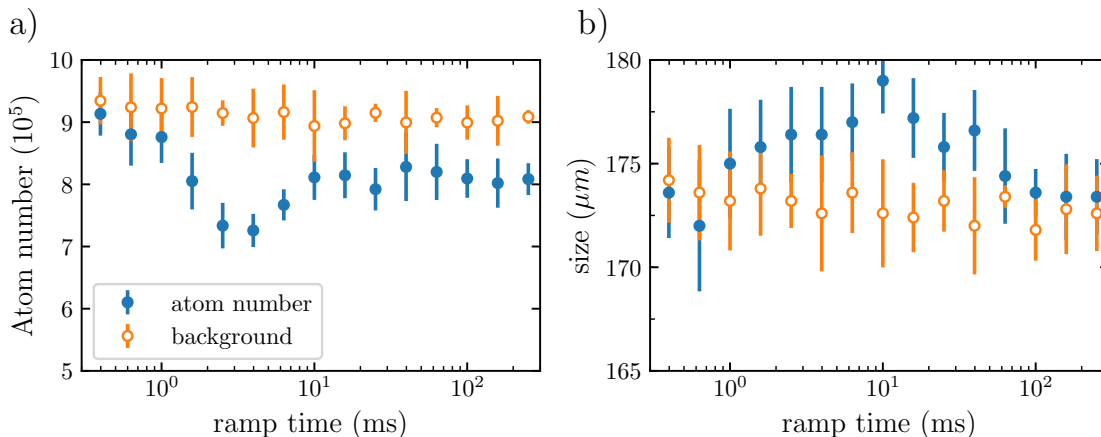


Figure 3.9: Role of adiabaticity in the dimple trick. a) Atom number and b) size of the atomic cloud (as a measure of the temperature after trap release at $t_{\text{TOF}} = 23$ ms) after the power of the dimple trap is ramped up and down again, compared to a background measurement without the dimple trap. For ramp times ≤ 10 ms parametric heating is visible while for larger times the process is nearly reversible.

Therefore we start by investigating if the condition of adiabaticity is fulfilled. After loading atoms into the reservoir we set the magnetic field to a high value of $B_0 = 940$ G ($\sim 900 a_0$) and wait for 4 s for sufficient initial thermalization. The dimple trap is turned on to a trap depth of $U = k_B \times 17 \mu\text{K}$ using a linear intensity ramp with a variable ramp time t_{ramp} and subsequently the intensity is ramped down again in the same way to turn off the trap. If conditions are the same before and after the ramps, the process is reversible and therefore adiabatic. We wait for another thermalization time of 5 s before we image the released atoms from the reservoir trap at a time of flight of $t_{\text{TOF}} = 23$ ms and extract the atom number as well as the cloud size (see Fig. 3.9). The cloud size after expansion can be seen as a measure of the temperature (see Ch. 2.6). As a comparison we show a background measurement where the atoms are simply held in the reservoir trap for the same time. We see that while at very short times $t_{\text{ramp}} < 1$ ms the system has no time to react and is basically identical to the background, for $1 \text{ ms} < t_{\text{ramp}} < 10$ ms the atom number (size) shows a minimum (maximum). Since the frequencies of the intensity ramps are on the same order as the trap frequencies parametric heating can occur [Savard et al., 1997] through which the atoms can accumulate kinetic energy to leave the trap. For larger ramp times well-above $t_{\text{ramp}} > 10$ ms the size comes back to the background and the atom number stays slightly below. This small discrepancy might already be an indication of three-body losses for which the corresponding time scale is on the order of $\tau_3 = (n_{\text{DT}}^2 L_3)^{-1} \sim 100$ ms where n_{DT} refers to the density in the dimple trap. We choose a ramp time of $t_{\text{ramp}} = 150$ ms which is long enough to

allow for elastic collisions between atoms in the reservoir and in the dimple trap.

In the following we investigate the gain in phase-space density as a function of the dimple trap depth U with the experimentally confirmed adiabaticity. For calculating phase-space densities $\Gamma = n_0\lambda_{\text{dB}}^3$ we use peak atomic densities obtained via

$$n_0 = N\bar{\omega}^3 \left(\frac{m}{2\pi k_B T} \right)^{3/2} \quad (3.31)$$

where the temperature T is measured in a time-of-flight expansion (see Ch. 2.6) while the mean trap frequency $\bar{\omega} = (\omega_x\omega_y\omega_z)^{1/3}$ is measured via an excitation of center-of-mass oscillations (see e.g. [Gensemer and Jin, 2001]) and via parametric heating for the reservoir and the dimple trap, respectively. When turning on the dimple trap, the determination of the atom number in it is not easily extracted since the atomic distribution is on top of the one in the reservoir trap. We therefore extract the atom number in the following way: after linearly ramping up the dimple trap within t_{ramp} at $B_0 = 920 \text{ G}$ we suddenly turn off the reservoir trap. We need to wait about 100 ms for expansion before the cloud is dilute enough to assign the remaining atoms on our absorption image to atoms in the dimple trap. In order to mitigate effects of plain evaporation during this waiting time, the atoms are held at $B_0 = 880 \text{ G}$ where they are non-interacting. Our results are displayed in Fig. 3.10. The gain in phase-space density rises for increasing trap depths and shows a maximum of 3.5 at a trap depth of $U = k_B \times 14 \mu\text{K}$. For larger trap depths the gain decreases since more atoms are loaded into the dimple trap and the situation becomes eventually comparable to a simple compression. The maximum gain is far below the numbers in [Stamper-Kurn et al., 1998] and shall be compared to our theoretical expectations. We therefore employ the simple model from above and refine it by replacing the two boxes by harmonic potentials $V_0(r) = V_i(r) + V(r)$ (see also [Rautenberg, 2021]) of the form

$$V_i(r) = \frac{1}{2}m\bar{\omega}_i^2 r^2 - U_i \quad \text{and} \quad r \leq r_{\text{max},i} = \frac{\sqrt{2k_B U_i/m}}{\bar{\omega}_i} \quad (3.32)$$

where the index i refers to initial quantities in the reservoir trap and we drop the index for the same quantities in the dimple trap. The calculated gain lies even below the experimental data and the maximum is shifted towards lower trap depths. Comparing the theoretical and experimental temperatures we see that the theory overestimates the temperature in the dimple trap. This may be explained by ongoing plain evaporation during the ramp time $t_{\text{ramp}} = 150 \text{ ms}$ of the dimple trap leading to lower temperatures. The time scale for evaporation in the reservoir trap

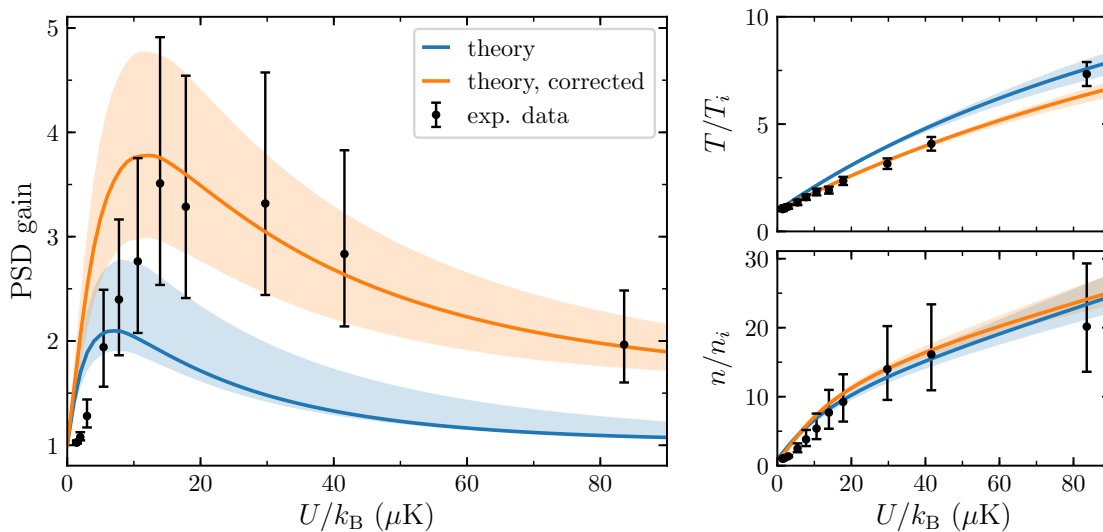


Figure 3.10: Performance of the dimple trick. The theoretical prediction (blue) underestimates the experimental data in the phase-space density gain unless the temperature is corrected (orange) accounting for plain evaporation (see text). Temperatures T and densities n are normalized by the initial values in the reservoir trap, which are $T_i = 1.1 \mu\text{K}$ and $n_i = 2.3 \times 10^{11} \text{cm}^{-3}$. Data points are averages and error bars include the standard error and uncertainties from trap frequency determinations.

is estimated via $\Gamma_{\text{ev}}^{-1} \approx [(\eta - 4)e^{-\eta}\Gamma_{\text{el}}]^{-1} = 110 \text{ ms}$ [Olson et al., 2013] with the truncation parameter $\eta = U/k_B T = 10$ and lies on the same order as t_{ramp} . We account for this effect by stretching the theoretical temperature by a somewhat arbitrary value of $T(3/4U)$ to match the experimental data. This also leads to a reasonable agreement between theory and experiment in the phase-space density gain and confirms the necessity of tuning the volume ratio of the traps for an efficient dimple trick.

In future experiments a larger reservoir trap with a beam waist of up to $650 \mu\text{m}$, limited by the available laser power, may be used to increase the volume ratio. With a similar beam waist and a smaller dimple phase-space density gains of 40 have been reached in the Innsbruck experiment for Cs [Weber, 2003]. Since the dimple trap in our setup also serves the purpose of loading Li from a MOT, we would have to compromise between Li and Cs. In Appendix A the setup of an independent dimple trap is described which can be used to find the optimal volume ratio. Monte Carlo simulations can help to obtain better theoretical predictions [Ma et al., 2004].

Evaporative Cooling

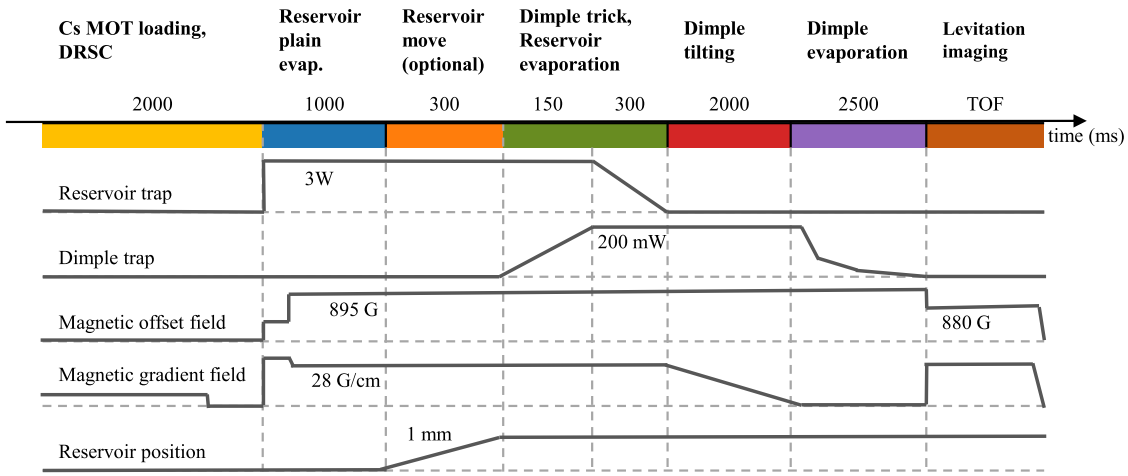
After the application of the dimple trick we now start to evaporatively cool our atomic sample. In the previous Sec. 3.2.2 we have already discussed a way of choosing the right scattering length via an optimal ratio of good to bad collisions. To quantify the process of evaporative cooling, we define the evaporation efficiency as [Ketterle and Druten, 1996]

$$\gamma = \frac{\log(\Gamma_{\text{final}}/\Gamma_{\text{initial}})}{\log(N_{\text{initial}}/N_{\text{final}})} \quad (3.33)$$

which is large if the gain in phase-space density is large compared to the loss of atoms before and after an evaporation sequence. Besides the evaporation efficiency it is also important to consider the total time of evaporation. In kinetic theory of evaporation [Luiten et al., 1996] it is assumed that the energy distribution of an evaporating gas is approximated well by a Boltzmann distribution which is truncated at the trap depth. Choosing a constant truncation parameter $\eta = U/k_B T$ with the right value would lead to a rescaling of the Boltzmann distribution during the cooling while its shape remains the same. In other words, this would ensure the right balance between the time of lowering the trap depth and a sufficient rethermalization time of the atoms. Usually, the optimal truncation parameter lies in the range of 6-10 for which the truncation has a small effect on the energy distribution. In [Olson et al., 2013] a model for 3D harmonic traps and constant $\eta > 6$ allows to find an optimal evaporation trajectory taking into account elastic and inelastic collisions as well as changes in the trap shape. This model is used to obtain starting points for efficient evaporation. Finally, the presented evaporation scheme is empirically optimized.

In Fig. 3.11a) our experimental sequence to Bose-Einstein condensation is summarized leading to the evaporation dynamics shown in Fig. 3.11b). We also include the loading of the reservoir trap (open data points) which marks the time $t = 0$. We load the magnetically levitated reservoir trap with a trap depth of $U = k_B \times 10 \mu\text{K}$ at a magnetic field large enough to compensate for anti-trapping (here $B_0 = 600 \text{ G}$) with 8×10^6 Cs atoms and an initial phase-space density of 1×10^{-3} . Afterwards, we go to the target magnetic field of $B_0 = 895 \text{ G}$ corresponding to a scattering length of $a \sim 300 a_0$. Although we go to this magnetic field as soon as possible in our sequence to profit from low densities and low three-body losses when crossing a series of Feshbach resonances (see Fig. 3.2) we observe an atom loss by over 60 % during this step. The third data point is an optional spatial displacement of the reservoir trap for a mixing scheme with Li (see e.g. [Pires et al., 2014b]) which shall not be discussed further here. The dimple trap is ramped up in 150 ms followed by ramping down the reservoir trap in 300 ms. This leaves us with starting conditions

a)



b)

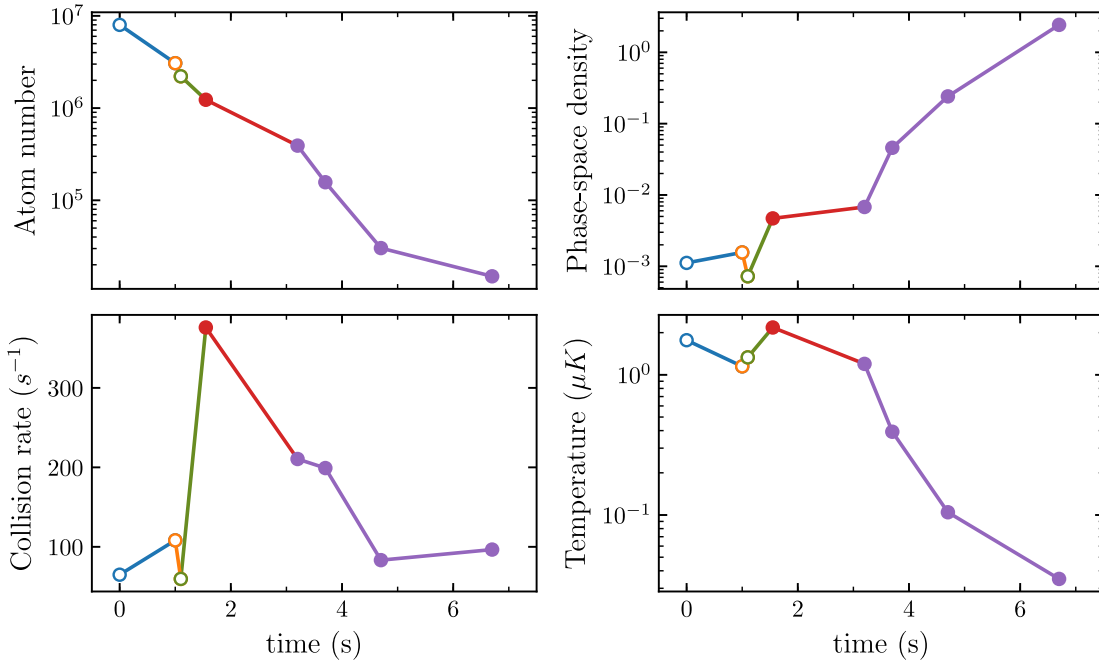


Figure 3.11: a) Schematics of the experimental sequence for creation of a Cs BEC at high magnetic fields. The most important parameters for the trapping potential and magnetic fields are displayed with time durations given in ms. b) Characteristic quantities during evaporation in the reservoir (open circles) and in the dimple trap (filled circles). The colors mark the different evaporation steps analogous to a). The time $t = 0$ is defined by the initial conditions in the reservoir trap.

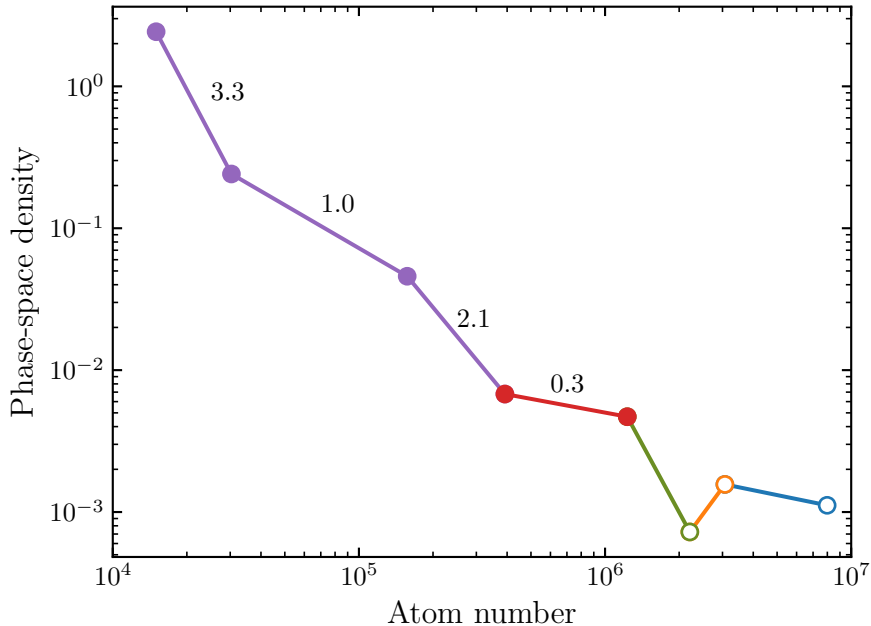


Figure 3.12: Evaporation to Cs BEC. Phase-space density and atom number measured after different stages of evaporation (see text) in the dimple trap (filled circles). Evaporation efficiencies γ between the stages are denoted above the lines (guide to the eye). The open circles mark atoms in the reservoir trap and colors are chosen analogous to Fig. 3.11.

of $N = 1 \times 10^6$ atoms in the dimple trap (filled data points) at a phase-space density of 5×10^{-3} . The collision rate is drastically enhanced from 60 s^{-1} to 376 s^{-1} . We evaporate further by ramping down the magnetic field gradient from 28 G/cm to 0 G/cm in 2 s which corresponds to a tilt of the trap in z -direction. This only yields a small increase in phase-space density to 7×10^{-3} . Afterwards the intensity of the laser decreased in a total time of 3.5 s followed by 0.5 s of plain evaporation during which Bose-Einstein condensation is reached. The three linear intensity ramps are performed with decreasing slope between each other to account for a decrease of collision rate trying to reach a constant truncation parameter η . Calculating the resulting evaporation efficiencies (Fig. 3.12) we note that the intensity ramps (purple lines) with an average of $\bar{\gamma} = 2.1$ are much more efficient than the previous tilt via the magnetic field gradient with $\gamma = 0.3$. We speculate that the inefficient evaporation might be due to the atoms leaving the trap only in z -direction making the evaporation one-dimensional. In this case an increase in the scattering length would help to create high energy atoms through collisions enabling them to find escape trajectories in all three dimensions through stochastic motion [Hung et al., 2008]. With the intensity ramps we can enhance the phase-space density by three

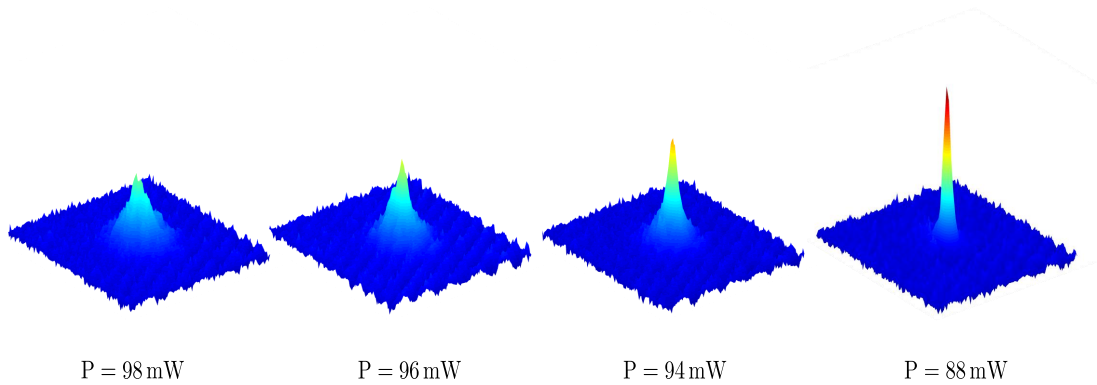


Figure 3.13: Onset of Cs Bose-Einstein condensate. In the two-dimensional column density the transition from a thermal gas (left) to an almost pure BEC can be observed by stopping the evaporation at different powers. The images are taken in a time-of-flight expansion.

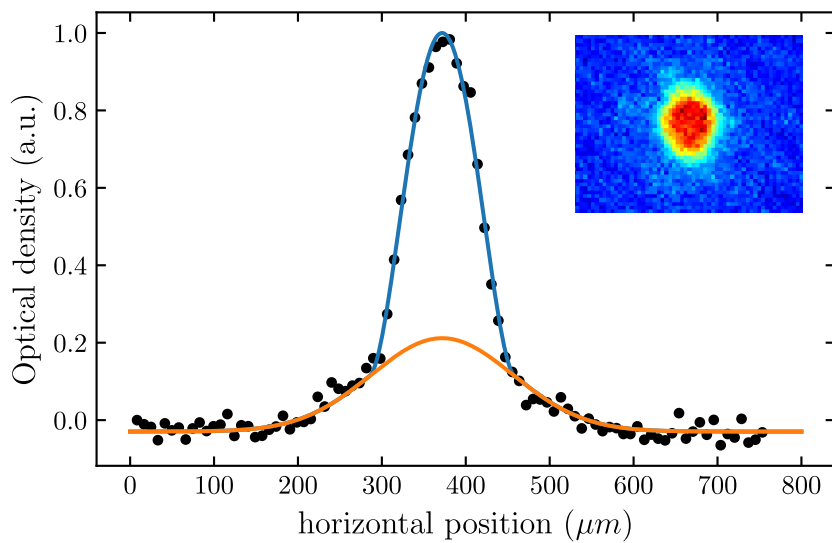


Figure 3.14: Bimodal distribution of Cs Bose-Einstein condensate shown in the one-dimensional column density. The image (inset) is taken after a time-of-flight expansion of $t = 55$ ms. From a bimodal fit we extract a condensed fraction of $f_c = 45\%$ and an atom number of $N = 1.3 \times 10^4$ in the condensed part. A Gaussian fit to the thermal wings (orange) yields a temperature of $T = 28$ nK.

orders of magnitude and obtain a temperature in the thermal fraction of the atomic distribution of around $T = 28\text{ nK}$. With this scheme we create pure BECs with $N = 1 - 2 \times 10^4$ atoms in an evaporation time below 7 s.

The onset of condensation can be observed in the density profiles (Fig. 3.13) which are taken after a time-of-flight expansion of 45 ms in the presence of magnetic field levitation. With final dimple trap powers in the typical range of $P = 98\text{ mW}$ to $P = 88\text{ mW}$ for which we stop the evaporation, we can control the condensed fraction arbitrarily and observe the build-up of the bimodal distribution giving evidence for Bose-Einstein condensation. Already small changes in laser power on the mW scale strongly influence the trapping potential due to the large effect of gravity for the heavy ${}^{133}\text{Cs}$ atoms. By fitting a two-dimensional bimodal function to the data (Fig. 3.14) we can extract the atom number and the condensed fraction. The temperature is extracted from the thermal wings of the distribution according to (2.8).

3.3 A quantum degenerate gas of ${}^6\text{Li}$

3.3.1 Scattering properties of ${}^6\text{Li}$

The scattering properties of ${}^6\text{Li}$ are fundamentally different compared to ${}^{133}\text{Cs}$ due to its fermionic nature. The Pauli exclusion principle suppresses collisions between two identical fermions and hence a spin mixture is required for thermalization and evaporative cooling. s-wave Feshbach resonances of different spin mixtures (Fig. 3.15) have been precisely mapped out via RF spectroscopy on weakly bound molecules [Zürn et al., 2013; Bartenstein et al., 2005]. In this work the Feshbach resonance of the $|1\rangle$ - $|2\rangle$ spin mixture around 834 G is employed which is a particularly broad resonance with a width of $\Delta = 300\text{ G}$ and a background scattering length of $a_{\text{bg}} = 1405\text{ a}_0$ yielding its universal character. Pioneering work such as the realization of a Bose-Einstein condensate of ${}^6\text{Li}_2$ dimers [Jochim et al., 2003; Zwierlein et al., 2003] and first studies on the BEC-BCS crossover [Bourdel et al., 2004] have been performed across this Feshbach resonance. Evaporation at unitarity is very effective due to the high two-body cross-section while three-body recombination is strongly suppressed in Li, even in a two-component mixture [Petrov, 2003]. Atom-dimer collisions, where a weakly bound dimer decays into a lower bound state, are hindered by the Pauli principle as this process would require two identical fermions to come close to each other on the order of the molecular state's size. [Petrov et al., 2004].

In our experiment evaporative cooling usually starts in a $|1\rangle$ - $|2\rangle$ spin mixture on resonance or close to resonance e.g. at 790 G where interactions are unitarity limited followed by a change of the magnetic field depending on the goal of the experiment.

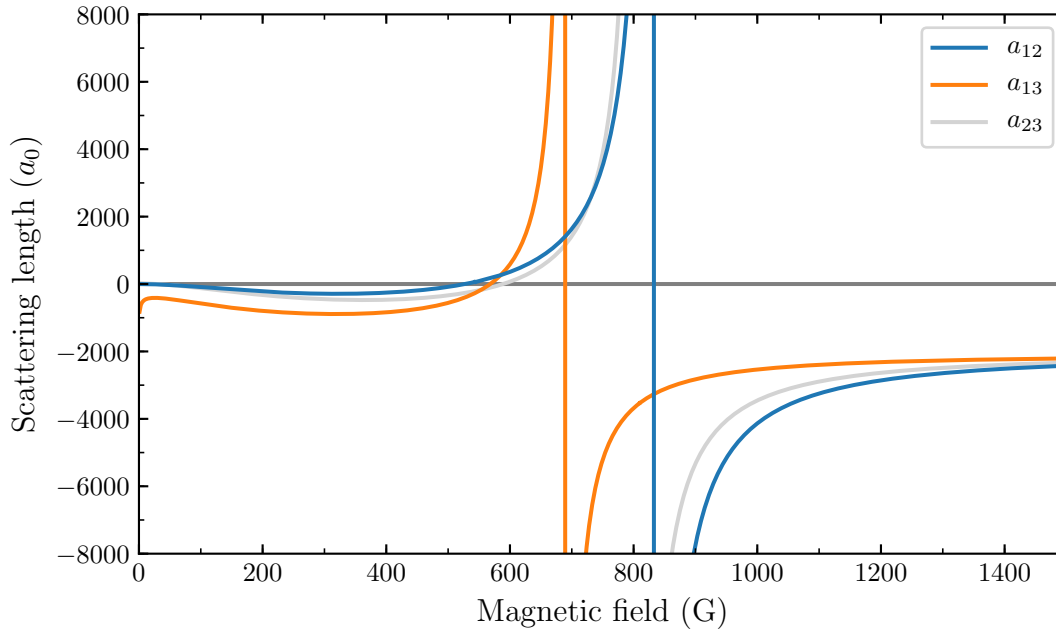


Figure 3.15: Feshbach resonances of ${}^6\text{Li}$ for different spin mixtures. The FRs for the $|1\rangle\text{-}|2\rangle$, $|1\rangle\text{-}|3\rangle$, and $|2\rangle\text{-}|3\rangle$ mixtures are centered around 834 G, 690 G, and 810 G, respectively. Data taken from [Zürn et al., 2013].

A molecular BEC (mBEC) can be created by evaporating further while the creation of a degenerate Fermi sea requires negative scattering lengths. Therefore, the mBEC can be dissociated by a magnetic field ramp across the Feshbach resonance. Above resonance, interactions are however strong due to the large background scattering length. In order to create a weakly, interacting Fermi gas one can jump with the magnetic field to ~ 300 G where the spin mixture has a small negative scattering length of $a_{12} \sim 300 a_0$. In our Bose polaron scenario we aim to be in the vicinity of the Li-Cs Feshbach resonance around 889 G (Sec. 3.4.1) in the final stage.

3.3.2 Experimental Realization

Based on the very different properties of ${}^6\text{Li}$ compared to ${}^{133}\text{Cs}$ as described in the previous section, we will discuss in the following how this determines our experimental procedure in preparing ${}^6\text{Li}$ impurities at ultracold temperatures. We begin the description with an improved scheme of loading Li atoms into the dimple trap after laser cooling. We then characterize the performance of evaporative cooling in the dimple trap and show how we can either create large molecular BECs or transfer ${}^6\text{Li}$ atoms into the tightly confined microtrap where they serve as impurities in the Bose polaron scenario.

Loading of Li atoms into Dimple Trap

The required trapping potential for Li is rather simple compared to the combined magnetic and optical potential for Cs (Sec. 3.2). It consists of a deep optical potential which is only slightly affected by gravity due to the small mass of Li. Other than in previous experiments in our group [Ulmanis et al., 2016b; Häfner et al., 2017; Gerken et al., 2019], we load a MOT with Li atoms for 1.5s with additional performance of gray molasses cooling yielding $N = 3 \times 10^7$ atoms at a temperature of $T = 42 \mu\text{K}$. The lower temperature after gray molasses cooling requires a shallower dipole trap on the order of $U \sim 6 - 10 k_B T$ for efficient transfer. We therefore employ a fast frequency modulation of the AOM ($\omega_{\text{mod}} \gg \omega_{x,y,z}$) which dynamically changes the diffraction angle of the laser beam, effectively enhancing the trap volume while reducing the trap depth.

The loading procedure is discussed in detail in [Gerken, 2022] and shall not be repeated here. After loading, we jump to a high magnetic field close to resonance to ensure fast thermalization. The high laser powers of the dimple trap up to 120 W per beam cause the two beams to spatially separate within tens of milliseconds due thermal lensing effects of the AOM [Heck, 2012]. We therefore do a first evaporation intensity ramp down to 37 W before the beams separate. In this way we end up with $N = 2.5 \times 10^6$ atoms in each spin state of the $|1\rangle$ - $|2\rangle$ mixture with a temperature of $T = 30 \mu\text{K}$ and a PSD of $\Gamma = 3 \times 10^{-5}$. We consider these parameters to be our starting conditions for further evaporative cooling.

Evaporative Cooling in the Dimple Trap

The evaporation of Li atoms in the dimple trap is done by lowering the laser intensity of the dimple trap (Fig. 3.16). We perform the evaporation at $B = 880 \text{ G}$ where the scattering length is $a = -8500 a_0$. However, the exact magnetic field around the Feshbach resonance is irrelevant due to the unitarity limit ($k^2 a^2 \gg 1$) where the two-body cross-section $\sigma(k) = 4\pi/k^2$ is independent of the scattering length. Analogously to Sec. 3.2, linear intensity ramps are used which are experimentally optimized by maximizing the evaporation efficiency (3.33). The large cross-section in combination with low three-body losses makes the evaporation highly efficient with efficiencies up to $\gamma = 8.8$. However, a drop in phase-space density after the third evaporation ramp occurs when we turn off the AOM frequency modulation. In this process we adiabatically ramp down the modulation amplitude of a triangular signal. An adiabatic change of the trap shape leads to a change in the phase-space density [Pinkse et al., 1997] and might explain this drop. Adiabaticity is confirmed in this measurement since we can revert the process. Although the starting conditions for evaporative cooling are worse than for Cs, the phase-space density can be enhanced by almost five orders of magnitude while the atom number only drops by

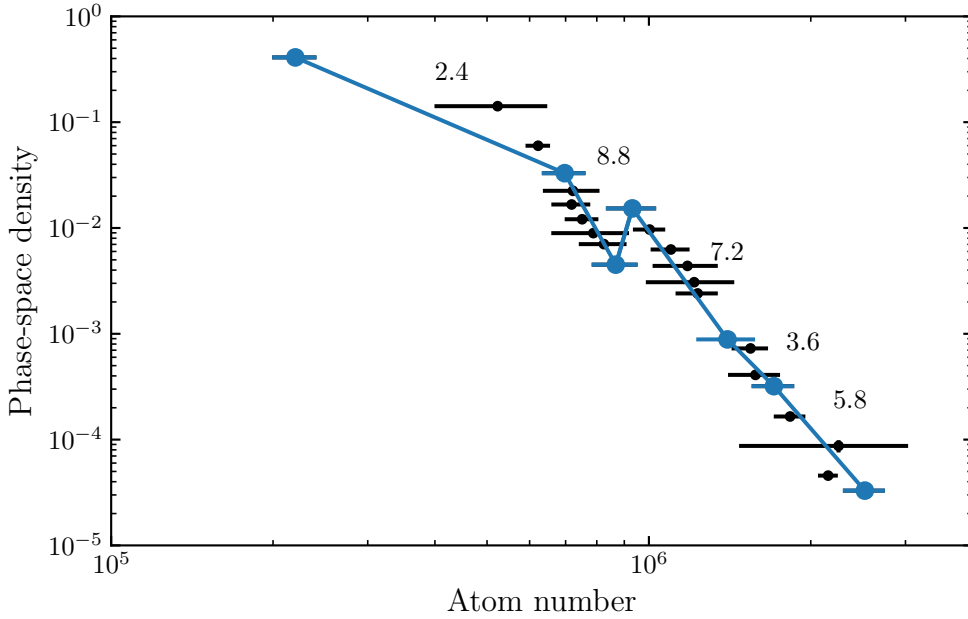


Figure 3.16: Li evaporation in the dimple trap. The numbers above the lines denote the evaporation efficiency between start and end points of linear evaporation ramps (blue points). The drop in evaporation efficiency after the third ramp is related to a turn off of the AOM frequency modulation. Data points are averages with standard errors. Adapted from [Gerken, 2022].

one order of magnitude.

Bose-Einstein condensation of ${}^6\text{Li}_2$ dimers can be reached by employing an analogous evaporation sequence at large positive scattering lengths, e.g. at $B = 790$ G (Fig. 3.17). In this way we typically achieve molecular BECs with $N \sim 1 \times 10^5$ dimers. We note that the dimers can be imaged with the same laser light as the atoms due to their small binding energy. Since the ground state energy shift is much smaller than the natural linewidth $\Gamma = 5.9$ MHz only the shift of the excited state plays a role [Jochim, 2004]. In the long-range excited state potential $V(R) \sim \hbar\Gamma(\lambda/2\pi R)^3$ [Zwierlein et al., 2003] where the internuclear distance R can be approximated by the scattering length a , one finds that the excited state shift is smaller than the linewidth for $a \sim 2000 a_0$ or a magnetic field of $B = 714$ G. Our images are therefore taken around this magnetic field in the weakly interacting regime.

Loading of Li atoms into Microtrap

For obtaining tightly confined Li impurities we perform evaporative cooling in the dimple trap at unitarity on the positive scattering length side as described above.

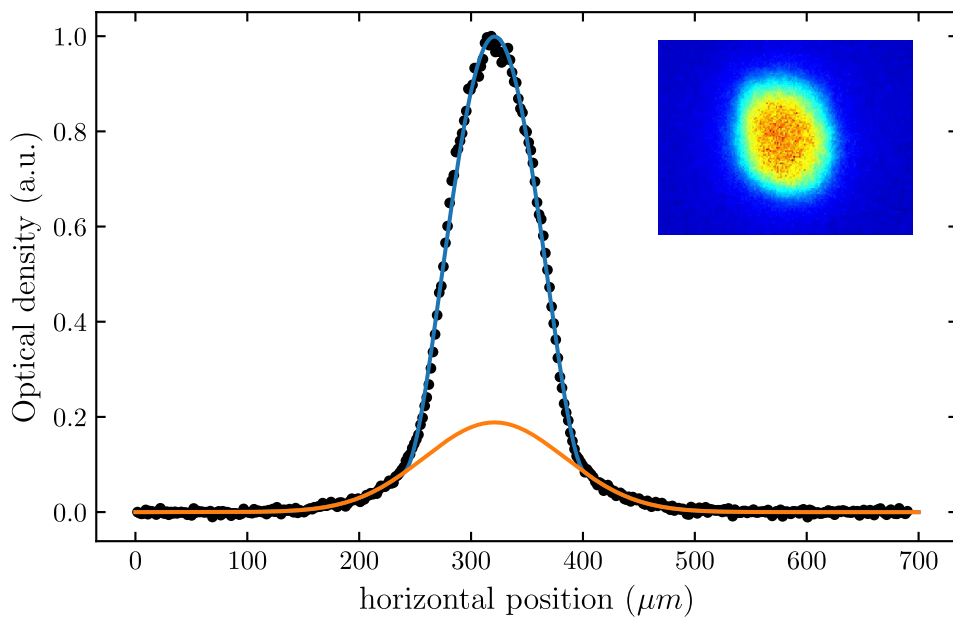


Figure 3.17: Bimodal distribution of molecular Bose-Einstein condensate of ${}^6\text{Li}_2$, taken after a time-of-flight expansion of $t = 10$ ms. The optical density is obtained through integration of the 2D column density which is depicted in the inset. From a bimodal fit (blue) we find a total dimer number of $N = 1.6 \times 10^5$ with a condensed fraction of $f_c = 71\%$. The orange curve shows the thermal wings of the distribution.

We stop the forced evaporative cooling when the dimple trap depth is smaller than the maximum microtrap depth $U_{\text{DT}} \leq U_{\text{MT}}^{\text{max}}$ to facilitate high transfer efficiencies. On the other hand, we leave the trap depth well above the dimer binding energy $U_{\text{DT}} > E_b$ (3.10) in order to avoid the formation of weakly bound dimers. The Li atoms are loaded into the microtrap (Fig. 3.18) by increasing its laser intensity and decreasing the dimple trap intensity. First attempts to load the microtrap yield $N \sim 1 \times 10^5$ atoms at a temperature of $T = 4 \mu\text{K}$ well above $E_b = 0.4 \mu\text{K}$ at $B = 790$ G. From here on, the further evaporation process for preparing single-component Li impurities in the Bose polaron scenario strongly depends on the mixing procedure of Li and Cs. Evaporative cooling could for example be continued at $B = 300$ G where $a \sim -300 a_0$ (see Fig. 3.15) before going to zero-field in order to load a MOT of Cs atoms. In the next section we discuss in more detail how such a mixing procedure could look like.

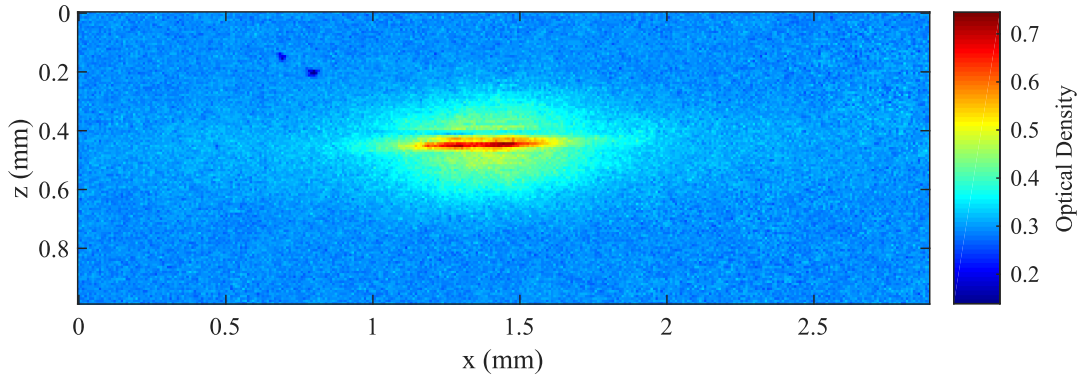


Figure 3.18: Loading of Li atoms into microtrap. The optical alignment of the microtrap beam ($w = 10 \mu\text{m}$) onto the dimple trap ($w = 62 \mu\text{m}$) is simplified by overlapping it with an expanding atomic cloud of Li atoms ($t_{\text{TOF}} = 0.5 \text{ms}$) after release from the dimple trap.

3.4 A quantum degenerate ${}^6\text{Li} - {}^{133}\text{Cs}$ mixture

3.4.1 ${}^6\text{Li} - {}^{133}\text{Cs}$ s-wave Feshbach resonances

The ${}^6\text{Li} - {}^{133}\text{Cs}$ system offers a large variety of s-wave Feshbach resonances which have been mapped out by atom-loss spectroscopy [Repp et al., 2013; Tung et al., 2013; Häfner, 2017] and by RF spectroscopy on weakly bound LiCs dimers [Ulmanis et al., 2015]. A theoretical analysis of the ${}^6\text{Li} - {}^{133}\text{Cs}$ Feshbach resonances comparing different models has been performed in [Pires et al., 2014a]. Resonances of larger interest include two broad resonances centered around $B = 843 \text{G}$ and $B = 889 \text{G}$ of the Li $|1\rangle \oplus \text{Cs } |3, 3\rangle$ and Li $|2\rangle \oplus \text{Cs } |3, 3\rangle$ scattering channel, respectively (Fig. 3.19). The center position of the former coincides with a negative Cs-Cs scattering length while the latter is on small positive Cs-Cs scattering lengths. The 889 G Feshbach resonance therefore offers the possibility to form stable Cs BECs while tuning the interspecies interactions and is therefore well suitable for studying the Bose polaron. The small background length of the Li-Cs Feshbach resonances of $a_{\text{bg}} \approx 30 a_0$ allows for the preparation of both a non-interacting and a strongly interacting Li-Cs mixture at the same magnetic field. Via a transfer of Li impurities between the $|1\rangle$ and $|2\rangle$ spin states by means of radio-frequency spectroscopy (Ch. 2.5) the polaron's spectral response can be mapped out.

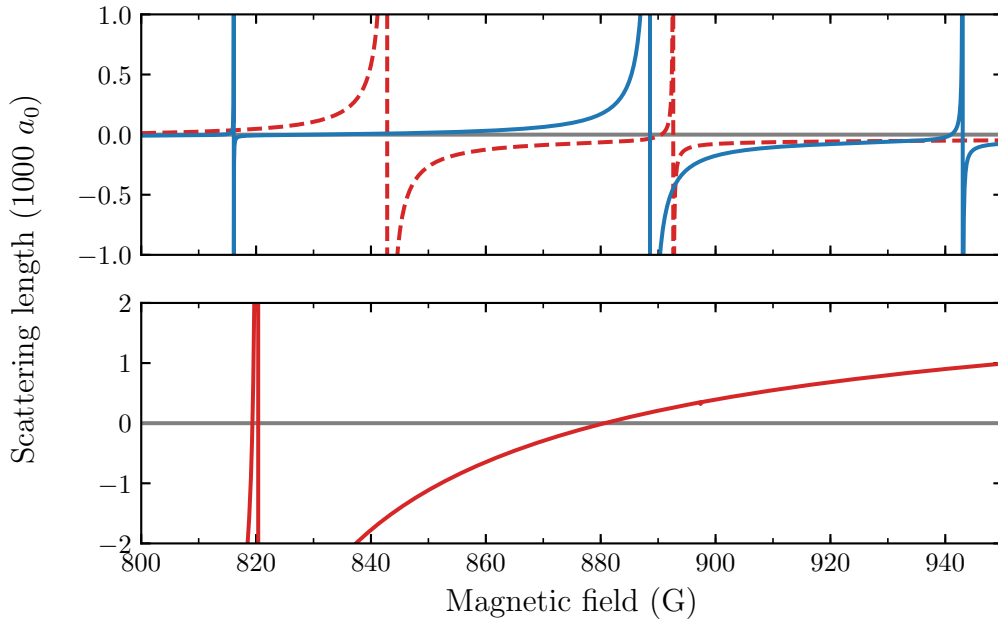


Figure 3.19: Li-Cs and Cs-Cs Feshbach resonances. Top panel: Magnetic field dependence of the interspecies scattering length of the Li $|2\rangle \oplus \text{Cs } |3,3\rangle$ (blue line) and Li $|1\rangle \oplus \text{Cs } |3,3\rangle$ (dashed red line) scattering channel. Calculated with parameters from [Häfner, 2017]. Bottom panel: Zero-crossing in the interspecies scattering length of the Cs $|3,3\rangle \oplus \text{Cs } |3,3\rangle$ channel. Data from [Berninger et al., 2013].

3.4.2 Preparation of degenerate ${}^6\text{Li} - {}^{133}\text{Cs}$ mixtures

In the previous sections we have discussed how to create Cs Bose-Einstein condensates and ultracold Li gases as well as the difficulties in their individual preparation. In this section we want to present a scheme allowing us to mix the two species in order to create Bose polarons. Therefore we will first discuss the individual steps from loading the MOT to combining the dipole traps highlighting the explicit challenges related to the Li-Cs mixture. Afterwards, we present our solutions and a proposed mixing scheme. We emphasize that the presented solutions are not the only possible ways of handling a Li-Cs mixture, but depicts a compromise between many factors.

Challenge 1: Dual-species MOT loading. During the initial phase of loading Li and Cs atoms into the MOT, we face two species-dependent issues. First, the large mass difference between Li and Cs requires magnetic fields of the Zeeman slower $B(z) \propto \sqrt{1/m}$ differing by a factor of five (see Ch. 2.2), making it hard to decelerate both species at the same time. Second, trapping Li and Cs in a double-species MOT suffers from light-assisted inelastic collisions which lead to atom loss

[Schlöder et al., 1999]. More precisely, collisions involving optically excited Cs can cause fine-structure changing collisions or radiative escape in the presence of a light field. For a review of inelastic collisions in a MOT we refer the reader to [Weiner et al., 1999].

Solution: The Li and Cs atoms are loaded into the MOT subsequently with different, optimized magnetic field profiles of the double-species Zeeman slower [Repp, 2013]. To overcome inelastic light-assisted collisions the two species are spatially separated. We do this by loading atoms from the Li MOT into the dimple trap with subsequent transfer into the microtrap (see Ch. 3.3.2). The microtrap is displaced in vertical direction away from the center enabling Cs atoms to be loaded into the MOT.

Challenge 2: Dipole trap loading. In many mixtures experiments, such as ${}^6\text{Li} - {}^{40}\text{K}$ [Spiegelhalter et al., 2010], ${}^6\text{Li} - {}^{23}\text{Na}$ [Hadzibabic et al., 2002], ${}^6\text{Li} - {}^{87}\text{Rb}$ [Silber et al., 2005] or ${}^{40}\text{K} - {}^{87}\text{Rb}$ [Ospelkaus et al., 2007], the two atomic species are loaded from the MOT into a common magnetic trap or optical dipole trap followed by evaporative cooling. In our case, besides the fact that $\text{Cs}|3,3\rangle$ is not magnetically trappable, we prepare Cs and Li atoms at temperatures of $T_{\text{Cs}} = 1 \mu\text{K}$ and $T_{\text{Li}} = 42 \mu\text{K}$ after degenerate Raman sideband cooling and gray molasses cooling, respectively. For effective dipole trap loading, trap depths of typically $U \sim 6 - 10 k_B T$ are required which cannot be fulfilled for both species at the same. At the wavelength of 1064 nm, where dipole trap lasers are commonly available, the polarizabilities of Cs and Li differ by $\alpha_{\text{Cs}}/\alpha_{\text{Li}} \approx 4$ (see Fig. 2.9) which makes the trap depth for Cs even deeper than for Li, although Cs would require a shallower trap.

Solution: The different requirements in temperatures are solved by loading Li and Cs atoms into the dimple trap and the large volume reservoir trap, respectively, which are well mode-matched to the individual species in terms of trap depth and trap volume. Besides the different temperatures, small densities for Cs are necessary to avoid high three-body losses which are less present for the fermionic Li. We also note that in our subsequent loading scheme it is important to load Li atoms into the dipole trap prior to the Cs atoms. The reason is that the Cs atoms in the reservoir trap are in the $|3,3\rangle$ ground state which requires a small magnetic field of a few G to maintain the spin polarization. On the other hand, when loading Li atoms into the MOT and performing gray molasses cooling the latter is already significantly disturbed at small magnetic fields above 1 G. This problem can therefore be circumvented by loading Cs atoms into the reservoir trap only after gray molasses cooling is finished.

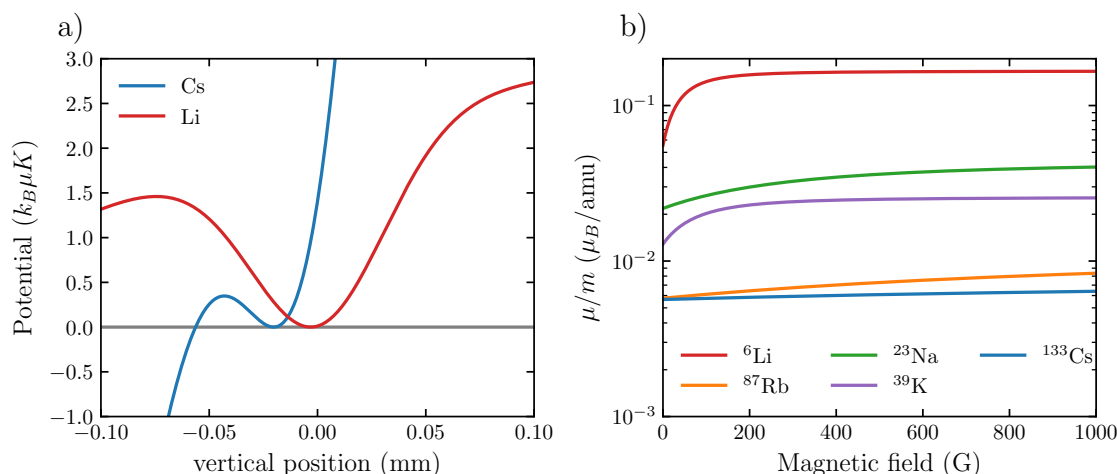


Figure 3.20: Dual-species overlap challenge of Li and Cs. a) Calculated trapping potentials of Li (red) and Cs (blue) at low temperatures. For shallow trapping potentials the potential minima for Li and Cs separate. b) Ratio of magnetic moment to mass for different alkali atoms. A vastly different ratio for Li and Cs implies different magnetic field gradients necessary to compensate for the gravitational sag.

Challenge 3: Dual-species overlap. When mixing the two species, a common approach is to trap both species in one final dipole trap, as we did in previous experiments where Li and Cs were in the dimple trap at 450 nK [Pires et al., 2014b]. However, at lower temperatures, the effect of gravity becomes more important (3.25) shifting the center of the trapping potential (‘gravitational sag’), see Fig. 3.20. For a harmonic trap the potential $U(z) = 1/2m\omega^2 z^2 + mgz$ has a minimum at $z = -g/\omega^2$ where the trap frequency scales as $\omega \propto \sqrt{U_0/m}$. In our case the highly mass-imbalanced Li-Cs mixture entirely separates at temperatures below 100 nK [Ulmanis et al., 2016b]. A simple magnetic levitation scheme to overcome this effect, as used e.g. in Rb-Cs mixtures, is not possible due to vastly different ratios of magnetic moment to mass (Fig. 3.20b)). Finally, even without gravitational sag, the widths of the thermal density distributions scale as $\sigma_{\text{Li}}/\sigma_{\text{Cs}} \propto \sqrt{\alpha_{\text{Cs}}/\alpha_{\text{Li}}} \approx 2$ (α_i refer to the real-part polarizabilities at a wavelength of 1064 nm) leading to a larger Li distribution which would be the opposite of what we aim for in the Bose polaron scenario.

Solution: The use of our tightly confined microtrap at the tune-out wavelength of 880 nm enables us to move the trapped Li atoms along the vertical direction without affecting the Cs trapping potential³. We expect that the tight confinement

³neglecting mean-field interactions between the two species which can alter the effective trap frequencies.

will enable us to confine Li atoms within the Cs BEC in radial direction to study Bose polarons. Our expectations are encouraged by recent experiments at MIT who make use of a similar dipole trap geometry [Yan et al., 2020].

Taking into account the different challenges for mixing Li and Cs we present a schematic experimental sequence in Fig. 3.21.

We start by loading Li atoms into the MOT and performing gray molasses cooling (1). Afterwards, the atoms are loaded into the dimple trap with a first evaporative cooling step (2). When the dimple trap depth is on the order of the microtrap depth $U_{\text{DT}} \leq U_{\text{MT}}^{\text{max}}$ the atoms are loaded into the microtrap by ramping up its intensity and ramping down the dimple trap intensity, following entirely the procedure of the Li preparation from Sec. 3.3. After evaporative cooling of the Li atoms around 300 G the microtrap is vertically displaced from the center of the experimental chamber by > 1 mm and stored allowing for an independent preparation of Cs (3). Since three-body losses in Li are largely suppressed (see Sec. 3.3.1), we expect lifetimes of > 20 s limited by one-body losses (see Fig. 3.3), in particular if we go away from the Li Feshbach resonance to prepare Cs. Once the Li atoms are stored, we can start to load Cs atoms into the MOT followed by the application of degenerate Raman sideband cooling (4). The Cs atoms are transferred into the reservoir trap (5) where a large number of atoms is trapped with low densities avoiding three-body losses. The dimple trick is applied to enhance the phase-space density with subsequent forced evaporative cooling (6). At this stage the sequence could follow the Cs BEC scheme presented in Sec. 3.2, allowing for a Cs BEC at high magnetic fields spatially separated from Li atoms in the microtrap (7). The ideal moment to move the Li atoms back onto the Cs atoms (8) is, however, subject of future experiments. A proper interspecies scattering length should be chosen to allow for thermalization between Li and Cs and the possibility of sympathetic cooling [Mudrich et al., 2002]. On the other hand, inelastic losses such as three-body losses between Li and Cs as well as one-body losses of Cs due to photon scattering of the microtrap light need to be taken into account when mixing the two species.

As an outlook we show calculations of the aimed trapping potentials and the corresponding density distributions for degenerate Li impurities in a Cs BEC (Fig. 3.22). For better visibility, density distributions of Li are multiplied by a factor of 10. For Cs we assume an improved condensate with $N_{\text{Cs}} = 1 \times 10^5$ atoms. In the microtrap an atomic cloud with $N_{\text{Li}} = 5 \times 10^3$ atoms is assumed, which is still easily resolvable with our absorption imaging system. By calculating the overlap integral this leads to a concentration of about $c \approx 2\%$. As expected from the geometry of our optical dipole traps, the Li impurities are well immersed in the Cs BEC in x- and z-direction due to the tight radial confinement of the microtrap and

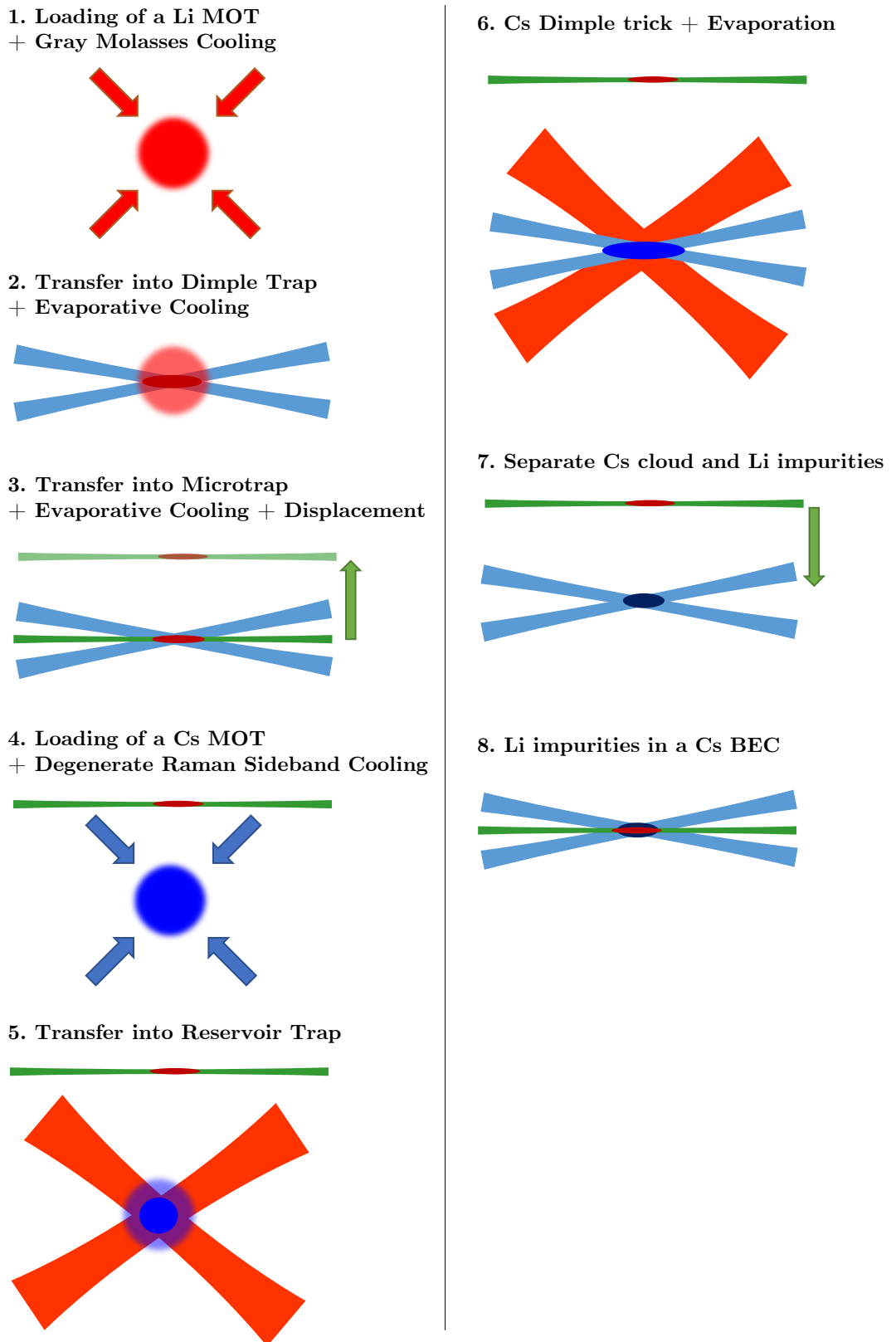


Figure 3.21: Schematic graph of the preparation of Li impurities in a Cs Bose-Einstein condensate.

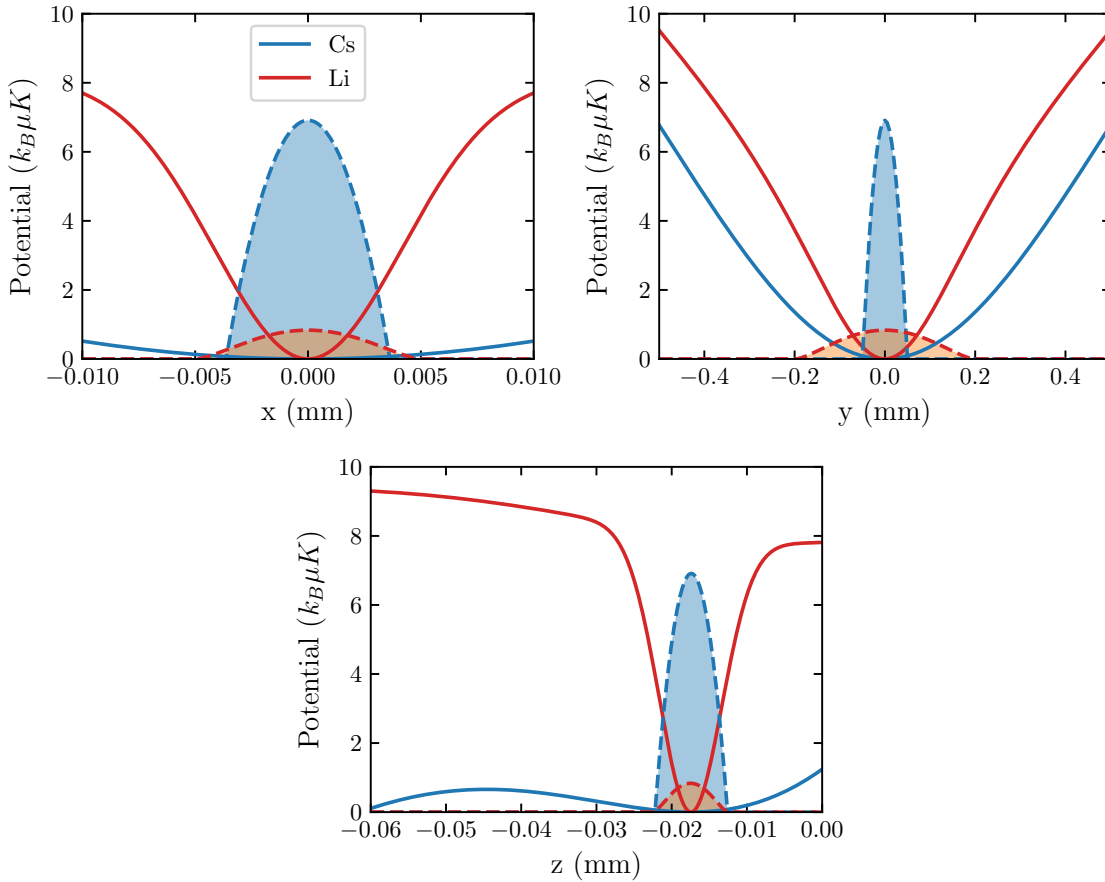


Figure 3.22: Calculated final trapping potentials (solid lines) and one-dimensional cut through density distributions (dashed lines) in arbitrary units for Li (zero-temperature profile) and Cs (Thomas-Fermi profile). The Li density distribution is multiplied by a factor of 10 for better visibility.

the cancellation of the relative gravitational sag. In y -direction the missing axial confinement of the single-beam microtrap results in a larger atomic distribution of Li. In RF spectroscopy measurements this can give rise to an additional signal at the bare Li transition frequency (see Ch. 2.5) next to the frequency related to the Bose polaron energy.

Conclusions

In conclusion, we presented the realization of a Cs Bose-Einstein condensate at high magnetic fields and the preparation of Li atoms in a tightly confined microtrap taking into consideration the challenges of combining Li and Cs for the realization of Bose polarons. In the first part, we presented our improved scheme of loading Cs into a magnetically levitated reservoir trap sample where we make use of fast magnetic field control. The experimental characterization of the dimple trick with

the existing trap geometry yields a small local phase-space density gain of ~ 3.5 in agreement with our theoretical model. This gain is far below state-of-the-art and can be further enhanced by an optimized volume ratio. With further evaporative cooling we achieve Cs BECs at $B = 895$ G with atom numbers of $N = 1 - 2 \times 10^4$. In the second part we presented our scheme to prepare Li samples with an improved dipole trap loading scheme and high evaporation efficiencies of up to $\gamma = 8.8$ in the dimple trap. Besides the realization of molecular BECs with dimer numbers of $N = 1 \times 10^5$, we transfer Li atoms into the translatable microtrap operating at the tune-out wavelength of Cs. Finally, we outline a scheme to combine a small number of Li atoms in a Cs BEC where we overcome the difficulties of the highly mass-imbalanced mixture such as the dipole trap loading or the large relative gravitational sag. While future experiments still need to answer open questions regarding three-body losses in the quantum degenerate regime or sympathetic cooling, a readily available and improved setup for performing radio-frequency spectroscopy on Li will allow to probe the spectral response of the Bose polaron.

Chapter 4

Fermions meet two bosons - the heteronuclear Efimov effect revisited

Parts of this chapter are based on the following publication:

Fermions Meet Two Bosons—the Heteronuclear Efimov Effect Revisited
B. Tran, M. Rautenberg, M. Gerken, E. Lippi, B. Zhu, Juris Ulmanis, M. Drescher, Manfred Salmhofer, T. Enss, and M. Weidemüller
Brazilian Journal of Physics (2021) 51:316-322

The Efimov effect was first predicted in 1970 by Vitaly Efimov [Efimov, 1970] describing the emergence of an infinite number of three-body bound states for particles with pairwise, resonant interaction. In the universal regime where the scattering length a exceeds the characteristic range of two-body interactions r_0 , an infinite number of three-body bound states can form which follow a discrete scaling law. Even if interactions are too weak to support two-body states, three particles can come together to form Efimov trimers. This unintuitive effect initially raised serious doubts about possible realizations and applicability, but theorists trying to prove Efimov wrong had to eventually admit that his predictions might be right. While Efimov suggested a possible observation in nuclear systems of three α -particles (^{12}C) or three nucleons (^3H), the existence of more than one three-body bound states requires the two-body interactions to be close to resonance. The tuning of two-body interactions via Feshbach resonances in ultracold quantum gases eventually enabled the first observation of the Efimov effect in a gas of ^{133}Cs atoms in 2006 [Kraemer et al., 2006]. Since then the Efimov effect has become a whole new area of research

and the initial investigations in homonuclear systems were followed by heteronuclear systems [Barontini et al., 2009, 2010; Bloom et al., 2013; Pires et al., 2014b; Tung et al., 2014]. In the ${}^6\text{Li} - {}^{133}\text{Cs}$ system with a large mass ratio the denser Efimov spectrum led to the observation of up to three consecutive Efimov states [Pires et al., 2014b; Tung et al., 2014]. Investigations on the Efimov effect are, however, not only relevant in the field of few-body physics. In particular, the influence of a many-body background medium on the Efimov trimers has been studied in different scenarios with a Fermi sea [MacNeill and Zhou, 2011; Nygaard and Zinner, 2014; Sun and Cui, 2019; Sanayei and Mathey, 2020] or a Bose-Einstein condensate [Zinner, 2013; Naidon, 2018]. On the other hand, theoretical studies have shown that many-body systems such as polaronic systems are influenced by the presence of three-body states [Levinsen et al., 2015; Sun et al., 2017; Sun and Cui, 2017]. Further studies on the Efimov effect are covered extensively in several reviews [Braaten and Hammer, 2006, 2007; Ferlaino et al., 2011; Blume, 2012; Wang et al., 2013, 2015; Naidon and Endo, 2017].

In this chapter we investigate the heteronuclear Efimov effect in a system consisting of two heavy bosons and one light fermion allowing us to work in the Born-Oppenheimer approximation. As a specific example, we consider fermionic ${}^6\text{Li}$ as a light particle and ${}^{133}\text{Cs}$ as heavy bosons. Two limiting cases of the Efimov effect are studied: first, we revisit the Efimov effect in vacuum, where we will show how the infinite series of three-body bound states arises as a consequence of an underlying attractive $-1/R^2$ potential [Fonseca et al., 1979; Bhaduri et al., 2011; Petrov, 2012] and investigate the influence of the intraspecies interactions on the Efimov spectrum [Häfner et al., 2017; Ulmanis, 2015; Wang et al., 2012]. In the second step, a Fermi sea is added as a background and we will study its influence on the Efimov trimers, again taking into account the intraspecies scattering length. The chapter is structured in the following way: after introducing the heteronuclear Efimov effect (Sec. 4.1) and the Born-Oppenheimer formalism (Sec. 4.2), we solve the Schrödinger equation in the vacuum limit in Sec. 4.3. Afterwards, the situation of two heavy bosons in a Fermi sea is considered where we introduce the effective interaction potential and solve the Schrödinger equation in Sec. 4.4.

4.1 The heteronuclear Efimov scenario

The heteronuclear Efimov scenario can be visualized in an energy diagram (Fig. 4.1) which is shown in dependence of the inverse interspecies scattering length $1/a$ between two identical bosons B and a distinguishable particle X. We first consider the case in which the two bosons interact resonantly ($a_{\text{BB}} \rightarrow \infty$). In the energy

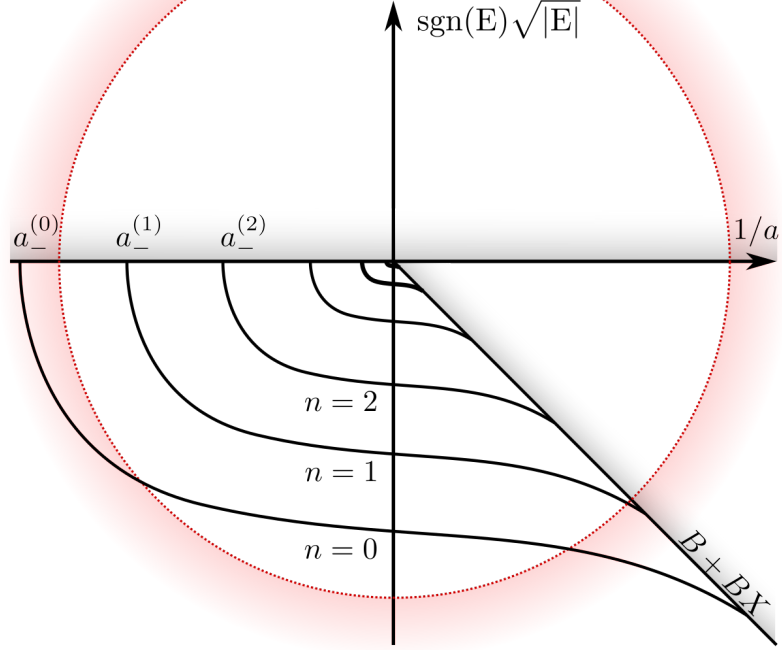


Figure 4.1: The heteronuclear Efimov scenario of two bosons B and one distinguishable atom X for resonant interactions between the bosons. The few deepest Efimov trimer states are drawn (solid lines) connecting the three-body scattering continuum with the atom-dimer threshold B+BX. The infinite series of Efimov states limited by short-range two-body interactions (red shaded circle).

diagram we can distinguish between three distinct areas, representing the three-body scattering states, the Efimov trimers, and the atom-dimer states. For $E > 0$, the three atoms are unbound and have a finite kinetic energy. For $E < 0$, a weakly bound dimer state BX exists on the positive scattering length side. Its binding energy (3.10) sets the atom-dimer threshold above which the dimer state BX coexists with a free atom B. The Efimov trimers are formed in the region below the three-body scattering continuum at $a < 0$ and the atom-dimer threshold at $a > 0$. In this region, an infinite number of Efimov states with energies E_n exist which cross the three-body scattering continuum at the scattering lengths $a_-^{(n)}$. Remarkably, these crossings follow the discrete scaling laws

$$\begin{aligned} a_-^{(n+1)} &= \lambda a_-^{(n)}, \\ E_{n+1} &= \lambda^{-2} E_n \end{aligned} \tag{4.1}$$

where $\lambda = e^{\pi/s_0}$ is the scaling factor characterized by the dimensionless parameter s_0 . The scaling factor gets smaller for increasing mass ratio and furthermore depends on the number of resonant interactions and the quantum statistics of the particles [Naidon and Endo, 2017].

Finally, in real systems, there is no infinite number of Efimov states due to finite range effects (red circle). That is, in the underlying interaction potential, only non-zero interparticle distances must be considered which leads to the definition of a ground state. It can be introduced by a three-body parameter (3BP) which is defined via the energy E_0 or the scattering length $a_-^{(0)}$ of the lowest Efimov state. As we will see in the next section, it is governed by short-range two-body interactions and thus the universal Efimov scaling only holds if the scattering length exceeds the characteristic van der Waals range $|a| \gg \max(r_{\text{vdW}}^{\text{BX}}, r_{\text{vdW}}^{\text{BB}})$.

4.2 Born-Oppenheimer approximation

In this section we introduce the concept of the Born-Oppenheimer (BO) approximation for the three-body problem. This concept is very similar to the textbook problem of the hydrogen molecular ion H_2^+ (see e.g. [Bransden and Joachain, 2003; Demtröder, 2016]) with a large proton to electron mass ratio of $m_p/m_e \approx 1836$ explaining the chemical binding from quantum mechanical principles. Here we present the BO approximation as discussed in the context of Efimov physics, following [Fonseca et al., 1979; Petrov, 2012]. We consider two heavy, identical bosons with mass M and displacement vector \mathbf{R} and a light atom with mass m . The two bosons and the light atom are located at $\pm\mathbf{R}/2$ and \mathbf{r} from the origin, respectively, as depicted in Fig. 4.2. The stationary Schrödinger equation for this system reads

$$H\Psi(\mathbf{r}, \mathbf{R}) = E\Psi(\mathbf{r}, \mathbf{R}) \quad (4.2)$$

with the three-body wavefunction $\Psi(\mathbf{r}, \mathbf{R})$ and the Hamiltonian ($\hbar = 1$)

$$H = -\frac{1}{M}\nabla_{\mathbf{R}}^2 - \frac{1}{2\mu_X}\nabla_{\mathbf{r}}^2 + V_{\text{BB}}(R) + \sum_{\pm} V_{\text{BX}}(|\mathbf{r} \pm \mathbf{R}/2|). \quad (4.3)$$

where $\mu_X = 2Mm/(2M + m)$ is the reduced mass of the light particle. Assuming a mass ratio of $M/m \gg 1$, the kinetic energy of the heavy atoms is much smaller than the one of the light atom. Therefore the wavefunction can be written in a product ansatz of the form

$$\Psi(\mathbf{r}, \mathbf{R}) = \psi_{\mathbf{R}}(\mathbf{r})\phi(\mathbf{R}) \quad (4.4)$$

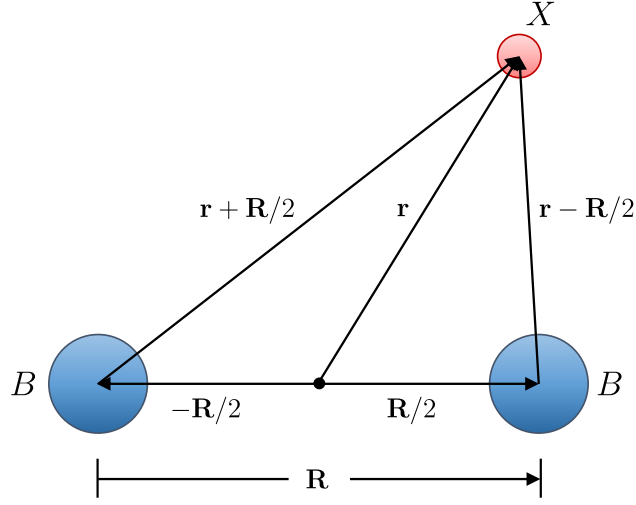


Figure 4.2: Coordinates of two heavy bosons B and a distinguishable atom X in the Born-Oppenheimer approximation.

where $\phi(\mathbf{R})$ is the wavefunction of the heavy atoms. The wavefunction $\psi_{\mathbf{R}}(\mathbf{r})$ describes the fast motion of the light atom which immediately follows the motion of the heavy atoms and only depends parametrically on \mathbf{R} , i.e. the interparticle separation can be chosen as a fixed parameter. In this approximation the Schrödinger equation splits into a set of two coupled equations. The equation of the light atom reads

$$\left[-\frac{1}{2m} \nabla_{\mathbf{r}}^2 + \sum_{\pm} V_{\text{BX}}(|\mathbf{r} \pm \mathbf{R}/2|) \right] \psi_{\mathbf{R}}(\mathbf{r}) = \epsilon(R) \psi_{\mathbf{R}}(\mathbf{r}) \quad (4.5)$$

with an energy $\epsilon(R) = \kappa^2(R)/2m$. This resulting energy serves as an interaction potential in the Schrödinger equation of the heavy bosons

$$\left[-\frac{1}{M} \nabla_{\mathbf{R}}^2 + V_{\text{BB}}(R) + \epsilon(R) \right] \phi(\mathbf{R}) = E \phi(\mathbf{R}). \quad (4.6)$$

In the first step we solve (4.5) where the interaction potentials $V_{\text{BX}}(|\mathbf{r} \pm \mathbf{R}/2|)$ are considered contact potentials [Huang and Yang, 1957] which are the simplest form of zero-range potentials. This problem is similar to the double-well problem and for bound states the light wavefunction can be expressed as

$$\psi_{\mathbf{R}}(\mathbf{r}) \propto C_1 \frac{e^{-\kappa(R)|\mathbf{r}-\mathbf{R}/2|}}{|\mathbf{r}-\mathbf{R}/2|} + C_2 \frac{e^{-\kappa(R)|\mathbf{r}+\mathbf{R}/2|}}{|\mathbf{r}+\mathbf{R}/2|} \quad (4.7)$$

where the coefficients C_1 , C_2 and $\kappa(R)$ can be obtained via the Bethe-Peierls boundary condition $\psi_{\mathbf{R}}(\mathbf{r}) \propto 1/|\mathbf{r} \pm \mathbf{R}/2| - 1/a$ for $\mathbf{r} \pm \mathbf{R}/2 \rightarrow 0$ and have the solutions

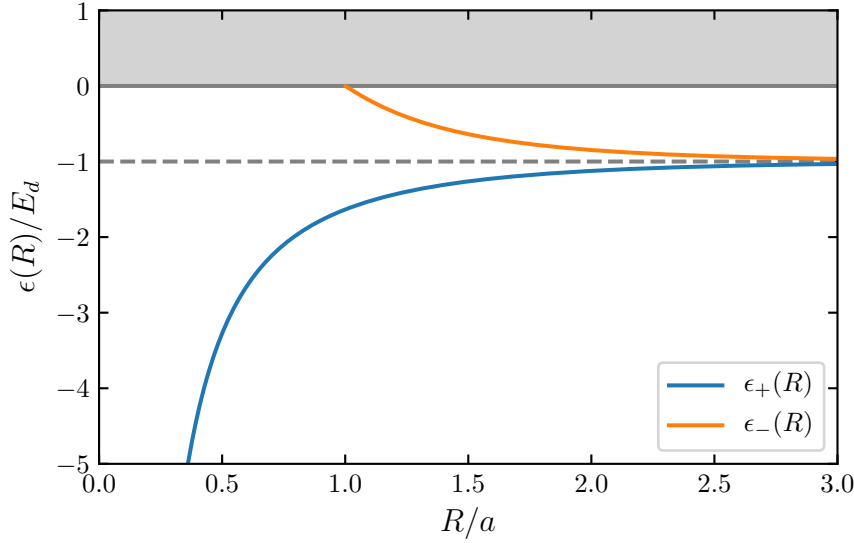


Figure 4.3: Symmetric (blue line) and antisymmetric (orange line) solution of the light atom Schrödinger equation. Both energies asymptotically approach the molecular dimer energy E_d (dashed grey line), while the antisymmetric solution hits the scattering continuum (grey area) at short-range.

$\{C_1, C_2\}_\pm = \{1, \pm 1\}$ [Petrov, 2012]. For the wavenumber we obtain the equation

$$\kappa_\pm(R) \mp \frac{e^{-\kappa_\pm(R)R}}{R} = \frac{1}{a} \quad (4.8)$$

which is solvable when $R/a > \mp 1$ and yields

$$\kappa_\pm(R) = \frac{1}{a} + \frac{1}{R} W(\pm e^{-R/a}). \quad (4.9)$$

Here, $W(z)$ denotes the Lambert W-function which has the property $z = W(z)e^{W(z)}$. With this result we can plot the symmetric and antisymmetric energies $\epsilon_\pm(R)$ of the light atom Schrödinger equation (4.5), as shown in Fig. 4.3. The symmetric (antisymmetric) solution ϵ_+ (ϵ_-) is attractive (repulsive) which means that through the presence of the light atom the heavy ones experience an attractive (repulsive) interaction. For small distances ($R/a < 1$), the symmetric state is the only bound state while the antisymmetric one hits the scattering continuum. If the interparticle distance between the two heavy atoms is very large ($R/a \gg 1$) the light atom can only localize on one heavy atom, thus the energies asymptotically approach the molecular dimer energy E_d . We can confirm this result by looking at the analytical solution obtained via a power series expansion of (4.9) for small $\exp(-R/a)$ in the

limit $R/a \gg 1$,

$$\kappa_{\pm}(R) \approx \frac{1}{a} \pm \frac{e^{-R/a}}{R} - \frac{e^{-2R/a}}{R}, \quad (4.10)$$

which yield the energies

$$\epsilon_{\pm}(R) \approx -\frac{1}{2ma^2} \mp \frac{e^{-R/a}}{maR} + \frac{e^{-2R/a}}{maR}(1 - a/2R). \quad (4.11)$$

The first term gives the above-mentioned molecular binding energy of the dimer state and the following terms show that for large R the light particle induces a Yukawa-type force between the heavy atoms. The Yukawa potential was originally introduced in nuclear physics to describe the nature of the interaction between protons and neutrons [Yukawa, 1955], but it is also known in solid-state physics as a screened Coulomb potential in the description of a collective electron gas [Hunklinger, 2017] or in the interaction between two Bose polarons [Naidon, 2018]. For $R/a \ll 1$, we find similarly via (4.8) the result

$$\epsilon_+(R) \approx -\frac{c^2}{2mR^2} \quad (4.12)$$

which becomes valid for all interparticle distances R at unitarity $a = \infty$. Here $c := W(1) \approx 0.567$ is connected to the scaling factor s_0 via $c = \sqrt{2m/M(s_0^2 + 1/4)}$. As we will demonstrate in the following section the attractive $-1/R^2$ potential lies at the heart of the Efimov effect and the infinite series of three-body bound states.

4.2.1 Boson-boson interaction in the heavy atom Schrödinger equation

After having solved the Schrödinger equation for the light atom, we now turn to the heavy atom equation (4.6) and use the energy $\epsilon_+(R)$, which we will refer to as the Efimov potential, serving as an induced interaction potential between the heavy atoms. Since we are interested in three-body bound states, we only consider the symmetric solution and, for simplicity, we will focus on the unitarity case (4.12).

For modelling the interaction between the two heavy bosons $V_{\text{BB}}(R)$, we would require knowledge of their molecular potentials. The collision between two ultracold, alkali atoms with electronic orbital angular momentum of $l = 0$ is described by their electronic Born-Oppenheimer interaction potential [Chin et al., 2010]. However, for qualitative understanding it often suffices to only consider the long-range van der Waals potential of the molecular potential, since the molecular potential and the Efimov potential are on vastly different energy scales. At distances $R < r_{\text{vdW}}$, where r_{vdW} is the so-called van der Waals length, the molecular potentials are typically on

the order of $\sim (10^3 - 10^4)\text{K}$ while the Efimov potential close to $R = r_{\text{vdW}}$ is typically on the order of $\sim (0.1 - 1\text{mK})$ [Chin, 2011]. Therefore, we model the interaction between the two heavy bosons by a van der Waals (vdW) potential with a hard core of the form [Gribakin and Flambaum, 1993; Flambaum et al., 1999]

$$V_{\text{BB}}(R) = \begin{cases} \infty, & R < R_0 \\ -C_6/R^6, & R > R_0. \end{cases} \quad (4.13)$$

where R_0 is a short-range cutoff radius. The C_6 coefficient can be naturally connected to the van der Waals radius r_{vdW} and energy E_{vdW} via [Chin et al., 2010]:

$$r_{\text{vdW}} = \frac{1}{2}(MC_6)^{1/4} \quad (4.14)$$

and

$$E_{\text{vdW}} = \frac{1}{Mr_{\text{vdW}}^2}. \quad (4.15)$$

For two ^{133}Cs atoms we calculate the vdW radius and energy to be $r_{\text{vdW}} = 101 a_0$ and $E_{\text{vdW}}/k_B = 0.13\text{mK}$ (or $E_{\text{vdW}}/h = 2.7\text{MHz}$) with the C_6 coefficient taken from [Chin et al., 2004b]. The cutoff radius R_0 in (4.13) is connected to the boson-boson scattering length a_{BB} via the analytical expression [Gribakin and Flambaum, 1993]

$$\frac{N_{1/4}(2r_{\text{vdW}}/R_0^2)}{J_{1/4}(2r_{\text{vdW}}/R_0^2)} = 1 - \sqrt{2} \frac{a_{\text{BB}}}{r_{\text{vdW}}} \frac{\Gamma(5/4)}{\Gamma(3/4)} \quad (4.16)$$

where $J_\nu(x)$ and $N_\nu(x)$ are Bessel functions of first and second kind, respectively. As (4.16) has multiple solutions, the cutoff R_0 does not only determine the boson-boson scattering length a_{BB} , but also the number of bound states within the vdW potential. However, the exact number of bound dimer states has no significant influence on the long-range Efimov wavefunctions [Wang et al., 2012]. From the vdW potential and the corresponding energy scale, we can already see that in the BO approximation the three-body parameter will be determined by the interaction of the two heavy bosons, as we will calculate in the next section.

4.3 Two bosons meet one fermion

We can now solve the Schrödinger equation of the heavy atoms (4.6) for a Cs-Cs-Li system with a large mass ratio of $M_{\text{Cs}}/m_{\text{Li}} = 22.1$. The calculation is performed with the matrix Numerov method [Pillai et al., 2012] on a logarithmic grid from the short-range cutoff R_0 up to of distances of $R/r_{\text{vdW}} \sim 10^{10}$. The short-range cutoff is

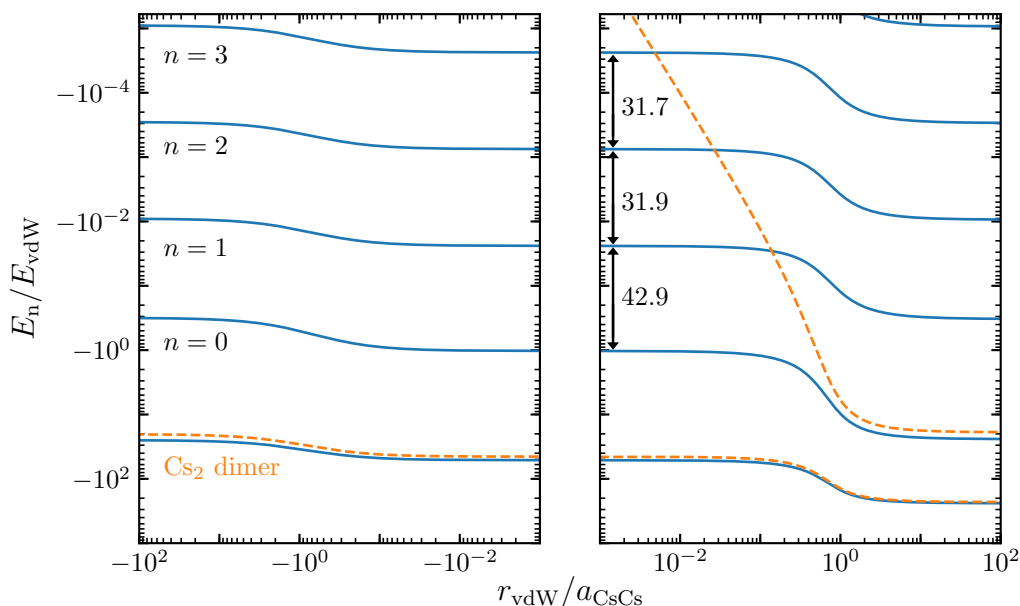


Figure 4.4: Efimov energy spectrum across a Cs-Cs resonance for resonant inter-species interaction. The spacing between the lowest Efimov trimer states (blue lines) is governed by the Cs₂ dimer states (orange dashed lines).

chosen such that the potentials support up to two Cs₂ dimer states. It is instructive to solve the two cases

- a) only boson-boson interaction $V_{\text{BB}}(R)$
- b) total potential $V_{\text{BB}}(R) + \epsilon_+(R)$.

which we show in Fig. 4.4 for positive and negative boson-boson scattering length. In case a) we can identify two weakly bound dimer states (orange dashed lines). For positive $a_{\text{CsCs}} \gg r_{\text{vdW}}$ the energy of the least bound state approaches the binding energy of the universal dimer $E_b = -1/Ma_{\text{CsCs}}^2$ (3.10) which is solely determined by the scattering length a_{CsCs} . The size of the wavefunction of this very weakly bound dimer state is typically on the order of the scattering length and is therefore also known as halo state [Chin et al., 2010]. The energy of the deeply bound state, however, persists across the resonance and shows gradual steps around $a_{\text{CsCs}} = r_{\text{vdW}}$ which mark a crossover between the vdW-dominated ($a_{\text{CsCs}} < r_{\text{vdW}}$) dimer and the halo state ($a_{\text{CsCs}} > r_{\text{vdW}}$). In case b), taking into account the total potential, we see that the energy of the most deeply bound state closely follows case a) and we can assign this state to the Cs₂ dimer. The following state $E_{n=0}$ does not coincide with the universal Cs₂ dimer anymore, but persists across the resonance. This clearly demonstrates the necessity of the mediated interaction via the Li atom to form Efimov states. Higher lying Efimov states $E_{n=1..3}$ are still affected by the presence

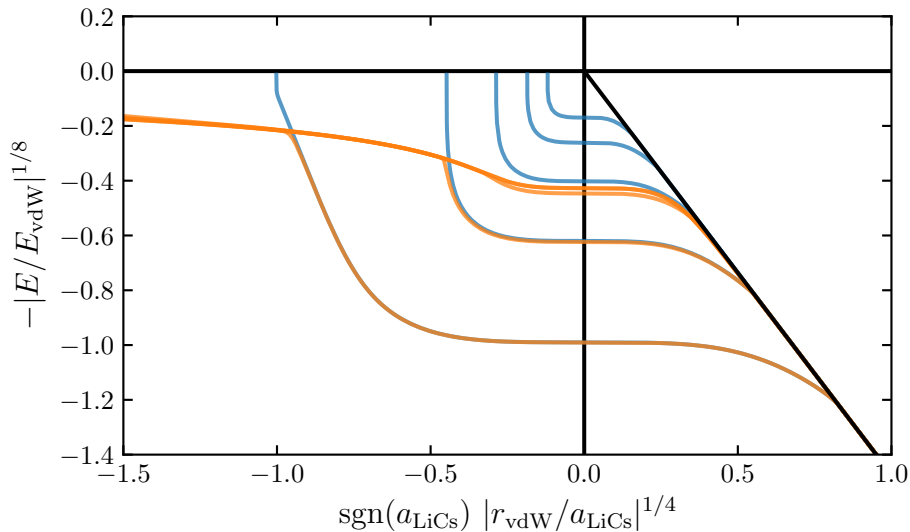


Figure 4.5: Efimov spectrum of two Cs atoms in a Li Fermi sea with $a_{BB} = \infty$ (blue line). A finite density of the Fermi sea of (orange line) modifies the binding energies of the Efimov states as well as the scattering continuum. Data shown for fermion wavevectors of $k_{Fr_{vdW}} = 0.00$ (blue) and $k_{Fr_{vdW}} = 0.01$ (orange).

of the large halo dimer, as indicated by the gradual steps around $a_{CsCs} = r_{vdW}$. From the energy spectrum we can additionally calculate the scaling factors $\lambda_n^2 := E_n/E_{n-1}$ between two adjacent energy levels for which we expect the universal value of $\lambda_{BO}^2 = (5.63)^2 = 31.7$ in case of a pure $-1/R^2$ potential in the BO approximation. However, the presence of the Cs_2 dimer state determines the three-body parameter E_0 and leads to a scaling factor of $\lambda_1^2 = 42.9$ well above the universal value at resonance. The scaling factor approaches the universal value for higher-lying states where already the second factor $\lambda_2^2 = 31.9$ only shows a small deviation.

4.4 Two bosons meet the Fermi sea

We now turn to the scenario where the two heavy Cs atoms are immersed in a Li Fermi sea (Fig. 4.5). In this scenario the binding energies are modified and the scattering continuum is lowered [Nygaard and Zinner, 2014; Sun and Cui, 2019]. Instead of three free atoms or a dimer plus one free atom, the scattering continuum is made of two impurities in a Fermi sea (Fermi polarons) or an impurity dimer state in a Fermi sea dependent on the scattering length. To understand the origin of this behaviour we will in the following first derive the mediated interaction potential of two heavy atoms in the presence of a whole Fermi sea, following [Nishida, 2009]. Afterwards, we solve the Schrödinger equation analogously to the previous section

and investigate the effect of the Fermi sea on the binding energies of the Efimov states, which we refer to as *in-medium Efimov states*, with focus on the intraspecies scattering length. Finally, we discuss our findings on how the Efimov scaling law is violated and is replaced instead by a modified version incorporating the length scale k_F of the Fermi sea.

We start by extending the Hamiltonian (4.3) to N fermions at positions \mathbf{r}_i which yields

$$H = -\frac{1}{M}\nabla_{\mathbf{R}}^2 - \sum_{i=1}^N \frac{1}{2m}\nabla_{\mathbf{r}_i}^2 + V_{\text{BB}}(R) + \sum_{i=1}^N [V_{\text{BX}}(|\mathbf{r}_i + \mathbf{R}/2|) + V_{\text{BX}}(|\mathbf{r}_i - \mathbf{R}/2|)] \quad (4.17)$$

In Sec. 4.2 we have already derived the bound state energies $\epsilon_{\pm}(\mathbf{R})$ for solving the light atom Schrödinger equation which we can use here analogously. In addition to the bound states, there exists a continuum of fermion scattering states at positive energies $\epsilon = k^2/2m > 0$. The fermion wavefunction is of the form

$$\psi_{\mathbf{R}}(\mathbf{r}) \propto C_1 \frac{\sin(k|\mathbf{r} - \mathbf{R}/2| + \delta_{\pm})}{|\mathbf{r} - \mathbf{R}/2|} + C_2 \frac{\sin(k|\mathbf{r} + \mathbf{R}/2| + \delta_{\pm})}{|\mathbf{r} + \mathbf{R}/2|}. \quad (4.18)$$

The coefficients C_1 , C_2 and the acquired scattering phase shift δ_{\pm} are found again via the Bethe-Peierls boundary condition, yielding $\{C_1, C_2\}_{\pm} = \{1, \pm 1\}$ and the equation

$$k \cos \delta_{\pm}(k) \pm \frac{\sin(kR + \delta_{\pm}(k))}{R} = -\frac{\sin \delta_{\pm}(k)}{a}. \quad (4.19)$$

Solving for the phase shift, one obtains

$$\tan \delta_{\pm}(k) = -\frac{kR \pm \sin(kR)}{R/a \pm \cos(kR)} \quad (4.20)$$

where $0 \leq \delta_{\pm}(k) < \pi$. Next, we assume that the atoms are confined in a large sphere with radius $L \gg R$ around the origin. At the boundary, the wavefunction vanishes $\psi(r \rightarrow L) \rightarrow 0$ such that we find discretized momenta

$$\begin{aligned} k_n^+ L + \delta_+ &= n\pi, \\ k_n^- L + \delta_- &= (n - 1/2)\pi. \end{aligned} \quad (4.21)$$

The total energy of the system is therefore

$$E = -\frac{\kappa_+^2 + \kappa_-^2}{2m} + \sum_{n=1}^N \frac{k_n^{+2} + k_n^{-2}}{2m}. \quad (4.22)$$

Taking the thermodynamic limit $N, L \rightarrow \infty$ and subtracting the free particle energies one can find the energy reduction

$$\Delta E(R) = -\frac{\kappa_+^2 + \kappa_-^2}{2m} - \int_0^{k_F} dk k \frac{\delta_+(k) + \delta_-(k)}{\pi m} \quad (4.23)$$

where for the Fermi momentum the definition $k_F := N\pi/L$ has been used. At large interparticle distances $R \rightarrow \infty$, the heavy bosons no longer interact and the energy reduction approaches the energy of two single polarons,

$$\Delta E(R \rightarrow \infty) \rightarrow 2\mu \quad (4.24)$$

where the single-polaron energy can be written down analytically as [Combescot et al., 2007]

$$\mu = -\frac{k_F^2}{2m} \frac{k_F a + [1 + (k_F a)^2][\pi/2 + \arctan(1/k_F a)]}{\pi(k_F a)^2}. \quad (4.25)$$

The effective, mediated interaction between the two heavy bosons is finally given by

$$V_{\text{eff}}(R) = \Delta E(R) - 2\mu. \quad (4.26)$$

It is instructive to write down the effective potential analytically in different limits. In the unitarity limit ($a \rightarrow \infty$), with a simple change of variables in (4.23), the effective potential can be expressed as

$$V_{\text{eff}}(R) = -\frac{c^2}{2mR^2} - \frac{k_F^2}{m} v(k_F R) \quad (4.27)$$

which has the exact same form as the Efimov potential (4.12) with the addition of a long-range term where $v(k_F R)$ is a dimensionless function representing the scattering contribution in (4.23). On the other hand, in the limit of $a \ll R, k_F^{-1}$, the potential is

$$V_{\text{eff}}(R) = -\frac{k_F^2}{2m} \frac{(ak_F)^2 \cos(2k_F R) - \sin(2k_F R)}{2\pi(k_F R)^4} \quad (4.28)$$

and of the same form as the RKKY interaction [Ruderman and Kittel, 1954] or of Friedel oscillations [Friedel, 1952] which are well-known in solid-state physics and

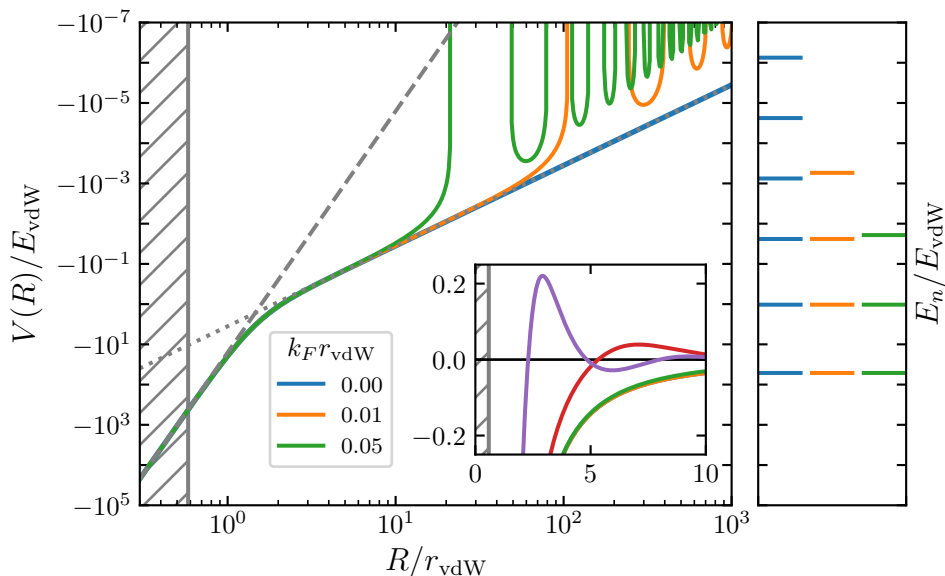


Figure 4.6: Left panel: Mediated interaction potential of two heavy Cs atoms in a Li Fermi sea with $a_{\text{CsCs}} = a_{\text{LiCs}} = \infty$. For comparison the pure $-1/R^2$ potential (grey dotted line) and the $-1/R^6$ potential (grey dashed line) with a short-range cutoff (hatched area) are plotted. On a lin-lin scale (inset) and higher values of $k_F r_{\text{vdW}} = 0.02$ (red) and $k_F r_{\text{vdW}} = 0.05$ (purple) the repulsive barrier with oscillating decay is clearly visible. Right panel: eigenenergies of the system for different k_F .

arise as a consequence of the sharp edge of the Fermi distribution.

The total potential $V(R) = V_{\text{eff}}(R) + V_{\text{BB}}(R)$ is shown in Fig. 4.6 for which we solve the heavy particle Schrödinger equation (4.6) with $a_{\text{CsCs}} = a_{\text{LiCs}} = \infty$. The gray hatched area marks the hard wall below the short-range cutoff R_0 . Setting $k_F r_{\text{vdW}} = 0$ we recover the Efimov potential $-1/R^2$ with short-range vdW interaction $-1/R^6$. For increasing k_F we observe the growth of a repulsive potential barrier which is located around $R = k_F^{-1}$. In addition, the potential barrier shows an oscillating decay at large distances which can be seen more clearly in the inset for larger values of k_F . The corresponding eigenenergies are shown in the right panel of Fig. 4.6 and we note that the values of the Fermi wavevector $0.01 \leq k_F r_{\text{vdW}} \leq 0.05$ are related to fermion density n via $k_F = (6\pi^2 n)^{1/3}$ and correspond to realistic experimental values on the order of $10^{11} \text{cm}^{-3} - 10^{13} \text{cm}^{-3}$. For $k_F r_{\text{vdW}} = 0.01$, the lowest Cs_2 dimer state and the two lowest in-medium Efimov states remain unaffected by the Fermi sea. However, the next higher bound state is shifted towards higher energies due to the rise of the potential around $R \sim 70 r_{\text{vdW}}$ forming the repulsive barrier. Any higher lying in-medium Efimov states are entirely suppressed upon increasing repulsion of the potential. In the same way, for a higher density of $k_F r_{\text{vdW}} = 0.05$, the potential starts to deviate from the pure $-1/R^2$ potential around $R \sim 10 r_{\text{vdW}}$

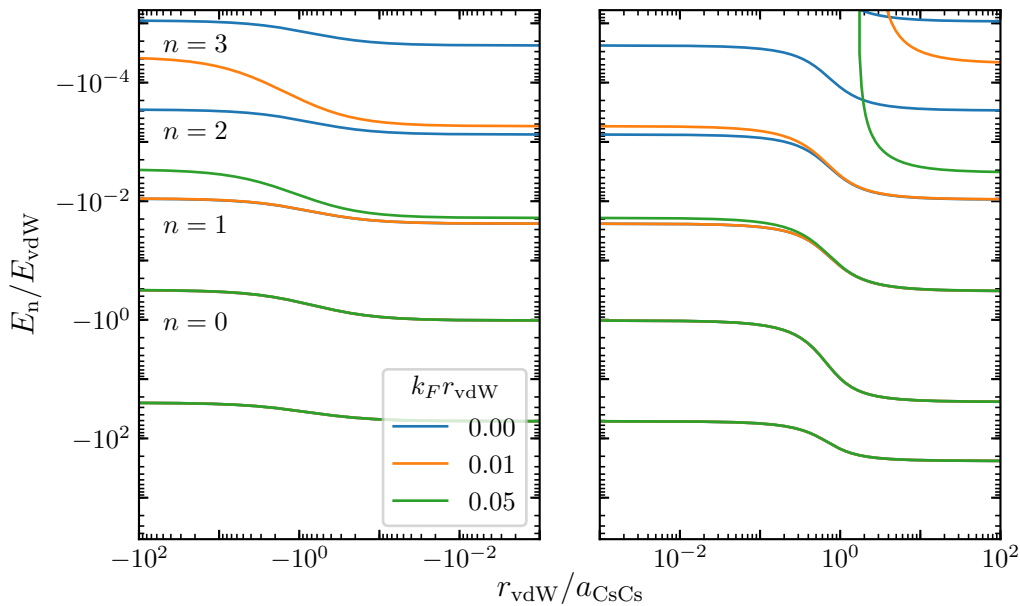


Figure 4.7: Energy spectrum of two Cs atoms in a Li Fermi sea across a Cs-Cs resonance (for $a_{\text{LiCs}} = \infty$). The presence of the Fermi sea leads to a suppression of bound states and break the discrete scaling behavior.

leading to a weakening of the binding already of the second Efimov state followed by suppression of the infinite series one state earlier than in the previous case.

As we did before for the Cs-Cs-Li system we would like to investigate the role of the intraspecies interaction in the presence of the Fermi sea (see Fig. 4.7). For $k_F r_{\text{vdW}} = 0$, we again recover the energies of the Efimov states without Fermi sea from Fig. 4.4. A finite density of the Fermi Sea ($k_F r_{\text{vdW}} = 0.05$) leads to first deviations in the energy E_1 for $a_{\text{CsCs}} > r_{\text{vdW}}$ when the system undergoes a change from the vdW-dominated to the long-range regime. After crossing the resonance towards negative scattering lengths, this deviation increases further around $-a_{\text{CsCs}} \sim r_{\text{vdW}}$. Before reaching the next step $a_{\text{CsCs}} \sim r_{\text{vdW}}$ on the positive scattering length side, the state rapidly rises to the dissociation threshold. Analogously, the states are more robust for $k_F r_{\text{vdW}} = 0.01$ and show a first deviation in the energy E_2 supporting one more bound state in total.

Finally, we calculate the density dependence of the binding energies (see Fig. 4.8). The energies remain nearly constant before they show a steep rise for increasing k_F disfavoring the formation of bound states. The symmetry of the curves suggests a scaling behavior similar to the three-body Efimov scenario. In the presence of the Fermi sea, a new discrete scaling law can be formulated incorporating the additional

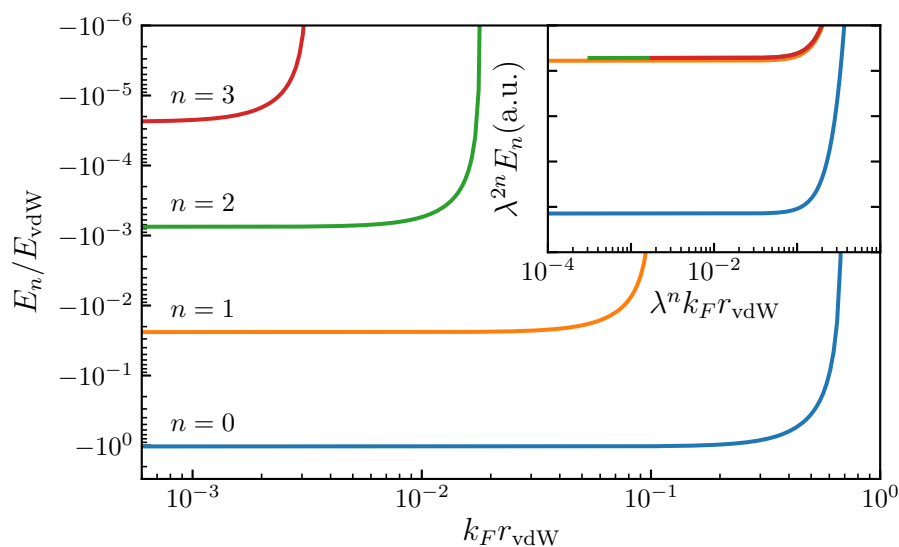


Figure 4.8: Density dependence of the bound state energies for intraspecies resonance. Inset: Clear deviations from the discrete scaling law are found for the ground state ($n = 0$) due to finite range effects while states with $n \geq 2$ fall on the same curve following the discrete scaling.

length scale k_F which reads [Nygaard and Zinner, 2014; Sun and Cui, 2019]

$$\begin{aligned} a_-^{(n+1)}(k_F) &= \lambda a_-^{(n)}(\lambda k_F), \\ E_{n+1}(k_F, a) &= \lambda^{-2} E_n(\lambda k_F, \lambda^{-1} a). \end{aligned} \quad (4.29)$$

In our calculation including boson-boson interactions, this scaling is fulfilled well for bound states $n \geq 2$ (see inset of Fig. 4.8). Analogous to the Cs-Cs-Li system the first excited bound state ($n = 1$) shows a slight deviation from (4.29) while the scaling is broken for the ground state due to the short-range vdW interaction.

Conclusions

In conclusion, we have calculated the Efimov energy spectrum in a system of two heavy Cs atoms in the limits of one additional Li atom as well as a whole Li Fermi sea taking into account intraspecies interactions. By using the Born-Oppenheimer approximation we find that in the former case the intraspecies interactions lead to a step-like behavior in the energy spectrum marking a crossover between regions dominated by the short-range vdW potential and the long-range Efimov potential. In the latter case, the formation of bound states is suppressed by the presence of the Li Fermi sea for sufficiently large k_F and the discrete Efimov scaling law is violated. However, a new discrete scaling law can be formulated by including k_F as an additional length scale. This may also give rise to new universal region ("window of

universality") which does not only depend on the characteristic range of two-body interactions, but also on the Fermi wavevector. Experimentally, the in-medium Efimov states may be mapped out analogously to previous experiments [Ulmanis et al., 2016b] via three-body losses with the new requirements of lower temperatures and higher densities for creation of a Fermi sea. The Feshbach resonances of the Li-Cs system around 843 G and 889 G also provide the possibility to investigate both negative and positive intraspecies interactions. More quantitative predictions on the positions of the bound states would, however, require calculations beyond the BO approximation which only deliver qualitative results. For the Li-Cs Efimov states in vacuum more quantitative results have been obtained in the spinless vdW theory [Häfner et al., 2017] in which the system is treated in a hyperspherical formalism with two-body interactions modeled by a Lennard Jones potential. Finally, in more realistic scenarios, finite temperatures and effects such as particle-hole formation due to scattering of the bound states with the Fermi sea, leading to an altered effective potential [MacNeill and Zhou, 2011], need to be considered.

Chapter 5

Scattering of two heavy Fermi polarons: Resonances and quasi-bound states

Parts of this chapter are based on the following publication:

Scattering of two heavy Fermi polarons: Resonances and quasibound states

T. Enss, [B. Tran](#), M. Rautenberg, M. Gerken, E. Lippi, M. Drescher, B. Zhu, M. Weidemüller, and Manfred Salmhofer
Physical Review A **102**, 063321 (2020)

In the previous chapter we have studied the effect of a Fermi sea on the three-body bound states in the strongly mass-imbalanced Li-Cs system. We now want to turn to the investigation of the scattering states ($E > 0$) where we consider two heavy impurities in a Fermi sea, or two heavy Fermi polarons. The possibility to create such quasiparticles with ultracold gases including the ability to enter the strongly interacting regime between impurity and Fermi sea has led to a number of realizations of Fermi polarons [Schirotzek et al., 2009; Nascimbène et al., 2009; Kohstall et al., 2012; Koschorreck et al., 2012; Cetina et al., 2016; Scazza et al., 2017; Yan et al., 2019; Ness et al., 2020; Fritsche et al., 2021] where e.g. the spectral properties have been mapped out. After studies of single-polaron properties, experimental investigations on fermion-mediated interactions [DeSalvo et al., 2019; Edri et al., 2020; Mukherjee et al., 2020], which were typically weak, have come into focus. Mediated interactions are of great interest due to their wide applicability across different areas of physics. In condensed matter physics, the RKKY interac-

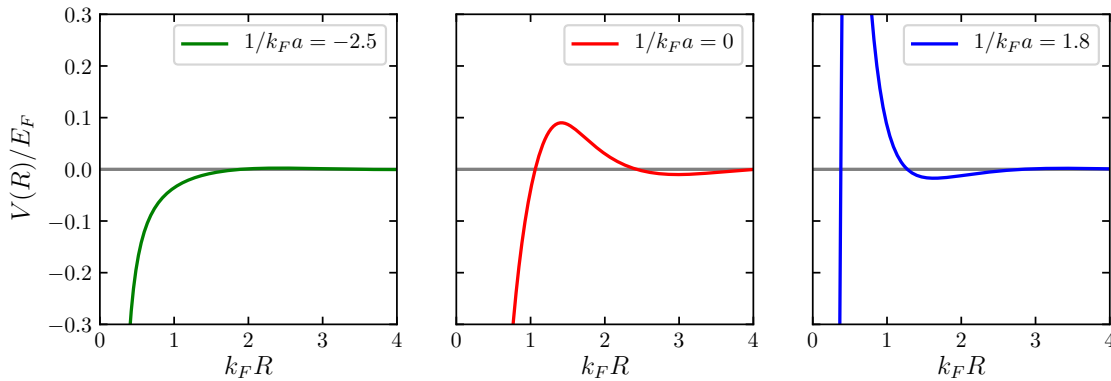


Figure 5.1: Effective potential between two heavy Cs atoms in a Li Fermi sea, shown for negative, resonant and positive interaction (from left to right).

tion serves as an indirect coupling between nuclear magnetic moments or localized electron moments via the conduction electrons in a metal. [Ruderman and Kittel, 1954]. In quantum field theory, the Casimir effect [Casimir, 1948] is a manifestation of mediated interactions between e.g. two conductor plates due to vacuum fluctuations. The Fermi sea in ultracold gases can be seen as an analogue of the vacuum in the Casimir effect [Nishida, 2009].

In the following we investigate the scattering properties of two Fermi polarons on the specific example of the Li-Cs system. Similarly to Ch. 4, we make use of the induced interaction potential in Born-Oppenheimer approximation [Nishida, 2009] to calculate the scattering phase shift and the induced scattering length between the impurities. In addition, we investigate if in-medium Efimov states can become quasi-bound states at positive energies where the induced interaction potential features a repulsive barrier. We start by introducing the variable phase method (Sec. 5.1) as a means to calculate the scattering properties. In Sec. 5.2 we first look at the Efimov bound state spectrum without intraspecies interactions before presenting our results for the scattering phase shift and our findings of resonances in the induced interactions in Sec. 5.3. Finally, the formation of quasi-bound states at positive energies is discussed in Sec. 5.4.

5.1 Variable phase method

Since in this chapter, we will only consider the effective potential between the heavy impurities (Fig. 5.1) without taking into account the intraspecies interactions, we omit the index $V(R) := V_{\text{eff}}(R)$. The heavy atoms are therefore governed by the

stationary Schrödinger equation

$$\left[-\frac{1}{M} \nabla_{\mathbf{R}}^2 + V(R) + 2\mu \right] \psi(\mathbf{R}) = E\psi(\mathbf{R}). \quad (5.1)$$

where 2μ is the energy of two free Fermi polarons (4.24). We can solve the Schrödinger equation directly to calculate the bound state energies, similarly to the results in Ch. 4. In addition to the bound state energies, we can calculate the scattering phase shift $\delta_{\ell}^{\text{ind}}(k)$ with angular momentum ℓ by comparing the phase of the scattered radial wavefunction to the free case. A more elegant way to calculate $\delta_{\ell}^{\text{ind}}(k)$ lies in the employment of the variable phase method [Calogero, 1967]. Instead of solving a second-order linear differential equation this method solves a first-order nonlinear differential equation (Riccati equation). The name *variable phase* comes from the fact that the dependent variable for which we solve is always directly linked to the scattering phase shift. Focusing on the s-wave phase shift ($\ell = 0$), we integrate the equation

$$k \partial_R \delta_{\ell=0}^{\text{ind}}(k, R) = -MV(R) \sin \left[kR + \delta_{\ell=0}^{\text{ind}}(k, R) \right]^2 \quad (5.2)$$

where the so-called phase function $\delta_{\ell=0}^{\text{ind}}(k, R)$ asymptotically approaches the scattering phase shift $\delta_{\ell=0}^{\text{ind}}(k, R \rightarrow \infty) = \delta_{\ell}^{\text{ind}}(k)$ with the boundary condition $\delta_{\ell=0}^{\text{ind}}(k, R = 0) = 0$. Via the effective range expansion (3.6) the scattering phase shift is related to the scattering length. An analogue variable equation can therefore be setup

$$\partial_R a_{\text{ind}}(R) = -MV(R)[R - a_{\text{ind}}(R)]^2 \quad (5.3)$$

with the boundary condition $a_{\text{ind}}(0) = 0$ and the induced scattering length $a_{\text{ind}} = a_{\text{ind}}(R \rightarrow \infty)$. Numerically, this equation cannot be solved straightforwardly by finite difference methods due to resonances in $a(R)$. By a change of variables [Ouerdane et al., 2003] $a(R) = \tan \theta(R)$ and $R = \tan \rho$ we instead solve the equation

$$\frac{d\theta(\rho)}{d\rho} = MV[\tan(\rho)] \sec^4 \rho \sin^2[\theta(\rho) - \rho] \quad (5.4)$$

for distances $[0, \pi/2)$. For all of the differential equations (5.1), (5.2), (5.4) we use an ordinary differential equation solver employing an explicit Runge-Kutta method of 8th order (DOP853).

Choice of short-range cutoff

Solving the above-mentioned equations requires a regularization since the singularity in the short-range effective potential $V(R \rightarrow 0) = -\alpha/R^2$ leads to a Hamiltonian which is only bounded from below for $\alpha < 1/4$. However, in a Li-Cs system, the large

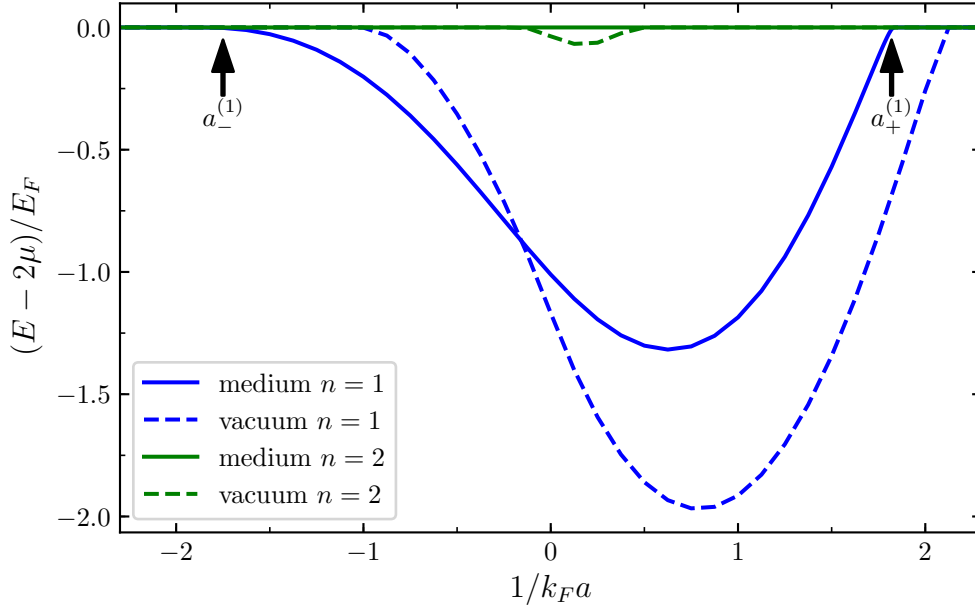


Figure 5.2: Efimov energy spectrum of two Cs atoms in the presence of one Li atom (vacuum, dashed line) or a Li Fermi sea (medium, solid line) relative to the scattering continuum 2μ . The medium shifts the scattering lengths $a_-^{(n)}$ (black arrows) where the Efimov states cross the continuum. In vacuum, the length and energy scales are $10R_0$ and $1/2m(10R_0^2)$, respectively (the Fermi energy has no physical meaning in this case).

mass ratio leads to $\alpha = (M/2m)c^2 \approx 3.6$. Therefore, we choose a hard cutoff R_0 such that the position of the Efimov ground state matches experimentally observed values. In [Häfner et al., 2017], an Efimov scattering resonance has been determined at $a_-^{(1)} = -2130a_0$, where a_0 is the Bohr radius. Correspondingly, the cutoff is calculated to be $R_0 = 220a_0$ or $k_F R_0 = 0.1$ if we assume a realistic fermion density of $n = 10^{13}\text{cm}^{-3}$, as used in typical Fermi polaron experiments [Cetina et al., 2016].

5.2 Efimov spectrum

We start by solving the Schrödinger equation for the heavy atoms (5.1) without intraspecies interactions for the Li-Cs system with $M/m = 22.17$ and a cutoff $R_0 = 220a_0$ as described above. The corresponding bound state energies are shown in Fig. 5.2. Compared to the three-body system (vacuum), the presence of the Li Fermi sea (medium) changes the binding energies and the scattering lengths $a_-^{(n)}$ where the energies hit the scattering continuum, as already seen in Ch. 4.4. For weak attraction, the Fermi sea facilitates binding and the scattering lengths $a_-^{(n)}$ shift

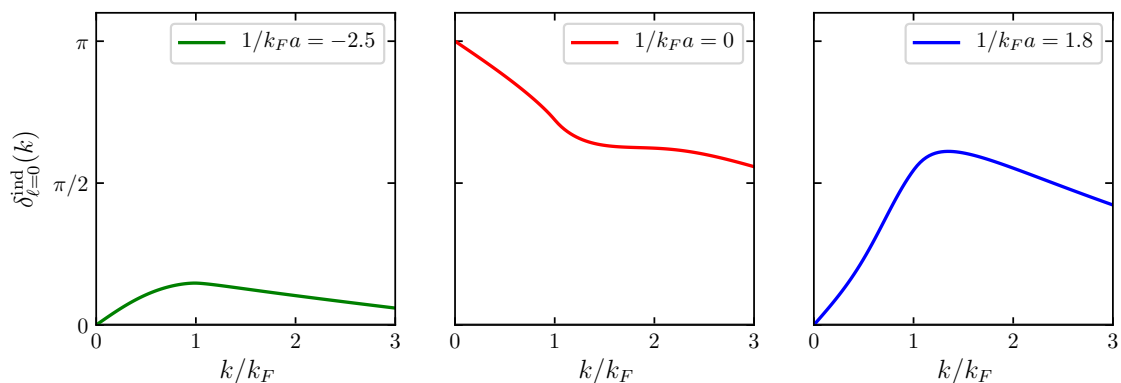


Figure 5.3: scattering phase shift at negative interaction, unitarity, and positive interaction.

towards smaller interaction strength. On the other hand, for positive scattering lengths, the repulsive barrier in the effective potential (Fig. 5.1) hinders binding and shifts $a_-^{(n)}$ towards larger interactions.

5.3 Scattering phase shift and induced scattering length

Besides the bound states we now want to investigate the scattering states. We therefore calculate the s-wave scattering phase shift $\delta_{\ell=0}^{\text{ind}}(k)$ by solving the variable phase equation (5.2) for different interaction regimes (Fig. 5.3). From these curves we can extract information on at least three important aspects: first, we recall that via the effective range expansion (3.6) the s-wave scattering length is related to the phase shift in the low energy limit:

$$a_{\text{ind}} = - \lim_{k \rightarrow 0} \frac{\tan \delta_{\ell=0}(k)}{k}. \quad (5.5)$$

Hence, the induced scattering length can be determined from the initial slope of the curves and yield values of $k_F a_{\text{ind}} = -0.8, +0.7, -1.0$ (from left to right) for the exemplary curves in Fig. 5.3. Second, using Levinson's theorem, the number of bound states n can be read off from the zero momentum phase shift

$$\delta_{\ell=0}(k \rightarrow 0) = n\pi. \quad (5.6)$$

At resonance, we therefore have one bound state, as also seen before in Fig. 5.2. Third, a rapid change of the scattering phase shift $\delta_{\ell=0}(k) = \pi/2, 3\pi/2, \dots$ through odd integers of $\pi/2$ leads to a maximum of the scattering cross section [Sakurai,

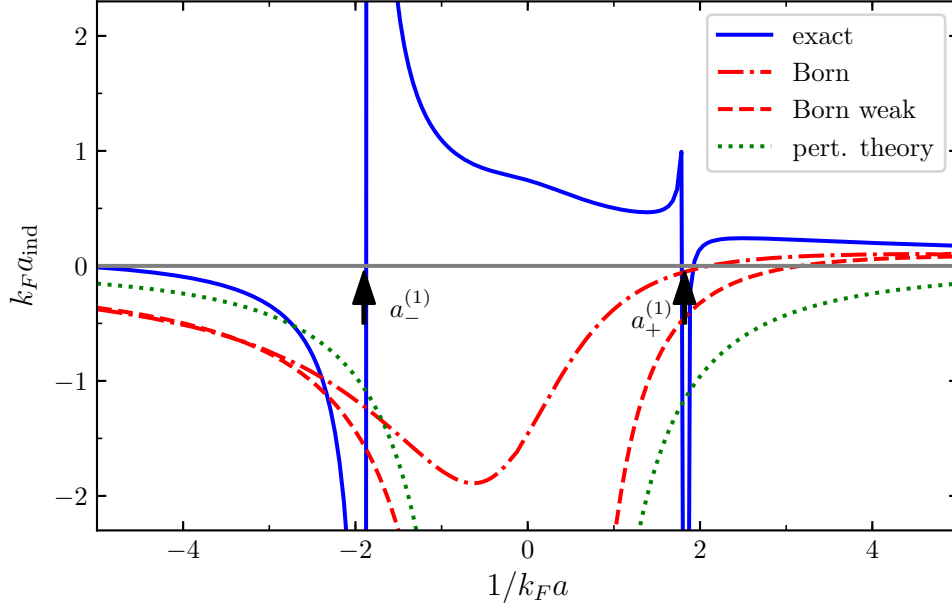


Figure 5.4: Induced scattering length between two Cs atoms in a Li Fermi sea. The exact solution of the Schrödinger equation (blue solid line) exhibits resonances at positions $a_{\pm}^{(1)}$ where the Efimov states cross the scattering continuum. In comparison, solutions using the Born approximation (red dotted-dashed line) in the weakly attractive limit (red dashed line) and second-order perturbation theory (green dotted line) are shown (see text for details).

1993]

$$\sigma_{\ell=0}(k) = \frac{4\pi}{k^2} \sin^2 \delta_{\ell=0}(k) = \frac{4\pi}{k^2} \frac{1}{1 + \cot^2 \delta_{\ell=0}(k)} \quad (5.7)$$

In the right panel of Fig. 5.3 we see that the phase shift steeply rises and crosses $\pi/2$. We will discuss in the next section in more detail how such a behavior might form quasibound states behind the repulsive barrier of the effective potential. Before that, we want to have a more detailed look on the induced scattering length and its dependence on the interspecies interaction.

The induced scattering length is obtained by solving the variable phase equation (5.3) and displayed in Fig. 5.4 (blue line). It exhibits two resonances, where one of each is located on the positive and negative coupling side. In order to understand the nature of these resonances we write down the analytical solution of (5.3) for the

short-range $-\alpha/R^2$ potential ($R_0 < R \ll |a|, k_F^{-1}$) in the interval $[R_0, R]$,

$$a_{\text{ind}}(R) = R \left[1 - \frac{1}{2\alpha} + \frac{s_0}{\alpha} \tan \left(\arctan \frac{1}{2s_0} - s_0 \log \frac{R}{R_0} \right) \right] \quad (5.8)$$

where $s_0 = \sqrt{\alpha - 1/4} > 0$. From this solution we find resonances with a log-periodicity and the solution is repeated whenever $s_0 \log(R/R_0)$ is a multiple of π . This corresponds to the typical periodicity of Efimov states [Petrov, 2012; Endo et al., 2011] with the scaling factor of $\lambda = \exp(\pi/s_0)$. In the solution including the full potential in Fig. 5.4 we can confirm that the position of the resonances correspond to the scattering lengths $a_-^{(1)}$ where the Efimov states cross the continuum in Fig. 5.2. For a smaller cutoff R_0 the potential supports more bound states [Sun and Cui, 2019] and we can find more resonances in the induced scattering length.

Let us now compare our solution to different theoretical approaches. For weakly repulsive impurities, the induced scattering length in second-order perturbation theory (PT) can be written as [Santamore and Timmermans, 2008]:

$$a_{\text{ind}}^{\text{PT}} = -\frac{k_F (M+m)^2}{2\pi Mm} a^2 + O(a^3). \quad (5.9)$$

PT therefore implies a negative induced interaction independent of the sign of the interspecies interaction. Compared to the exact solution of the Schrödinger equation we see no good agreement, even at weak coupling. We investigate this discrepancy by looking at the Born approximation. The Born approximation is a weak potential approximation assuming that the wavefunction is not substantially affected by the potential. In the variable phase method, the definition is taken that the phase function always stays small and never reaches multiples of $\pi/2$ [Calogero, 1967]. This corresponds to omitting the quadratic term in (5.3) and we can write

$$a_{\text{ind}}^{\text{Born}} = \int_0^\infty dR R^2 M V(R). \quad (5.10)$$

We note that in the Born approximation this equation is integrable without the necessity of a short-range cutoff R_0 . In the weakly attractive limit $1/k_F a \lesssim -1$ we can find an analytical solution with the potential

$$V_{\text{weak}} = -\frac{\Theta(|a| - R)}{2mR^2} \left(W(e^{R/|a|}) - \frac{R}{|a|} \right)^2 + \frac{a^2}{2m} \frac{2k_F R \cos(2k_F R) - \sin(2k_F R)}{2\pi R^4} + O((k_F a)^3) \quad (5.11)$$

where the first and second term correspond to the bound and scattering state con-

tribution, respectively (see Sec. 4.4). Inserting the potential (5.11) into (5.10) yields

$$a_{\text{weak}}^{\text{Born}} = \frac{M}{2m} \left(\gamma a - \frac{k_F}{\pi} a^2 + O(a^3) \right) \quad (5.12)$$

where $\gamma = \int_0^1 dx [W(\exp(x) - x)]^2 \approx 0.10$. We see that in addition to the quadratic dependence on the interspecies interaction a , which is also obtained in second-order PT (5.9), the Born approximation yields linear dependence on a coming from the bound state contribution of the potential. Therefore PT is not suitable to describe attractive impurities, even for weak coupling $R_0 < |a| < k_F^{-1}$ where the linear term is dominant.

Solving the induced scattering length in Born approximation (5.10) with the full potential, we find that it agrees well with (5.12) around $|1/k_F a| \gtrsim 3$. However, it still shows a significant discrepancy to the exact solution of the Schrödinger equation. We attribute this behavior to the singularity of the potential which might alter the wavefunction substantially beyond the validity of the Born approximation.

5.4 Quasibound states

Lastly, we want to investigate the possible existence of so-called quasibound states in our system. The repulsive barrier in the effective potential between the two heavy impurities (Fig. 5.1) raises the question whether in-medium Efimov states can be pushed towards positive energies $E > 0$ and survive behind the barrier, similar to those found in [Kartavtsev and Malykh, 2007]. Due to the finite height of the barrier and the possibility of quantum mechanical tunneling, the state will have a finite lifetime and will therefore be quasibound. As discussed above, the associated scattering phase shift of such a state rapidly rises through $n\pi/2$ (with $n = 1, 3, 5, \dots$) from below when the incident energy is resonant to the energy of the quasibound state and results in a maximum of the scattering cross section. More precisely, we identify a quasibound state if the resonance is of Breit-Wigner form. The Breit-Wigner formula is obtained by considering the s-wave scattering cross section (5.7) and expanding $\cot \delta_{\ell=0}(k)$ around the resonant energy E_{qbnd} assuming that it varies smoothly around the resonance. This yields

$$\cot \delta_{\ell=0}(k) = -\frac{2}{\Gamma_{\text{qbnd}}}(E - E_{\text{qbnd}}) + \dots \quad (5.13)$$

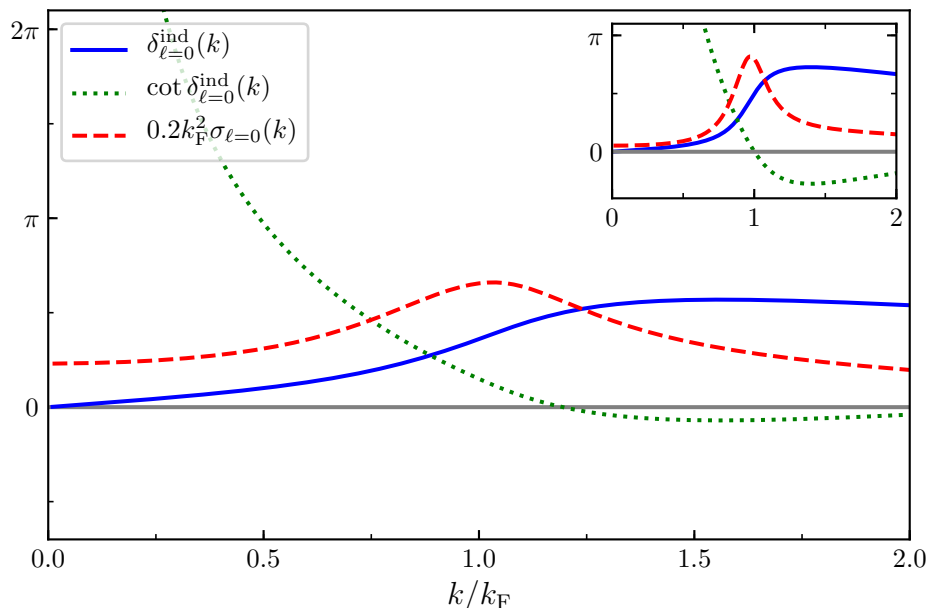


Figure 5.5: Scattering resonance and quasi-bound states. In the Li-Cs system enhanced scattering processes can be seen in the maximum of the scattering cross section (dashed red line). The phase shift (blue solid line) and its cotangent (green dotted line) cross the values of $\pi/2$ and 0, respectively, around $k = 1.12k_F$. The inset shows a well-defined quasibound state in a system with a larger mass ratio of $M/m = 44.33$.

where the definition $(d(\cot \delta_{\ell=0})/dk)_{E=E_{\text{qbnd}}} := 2/\Gamma_{\text{qbnd}}$ has been used. The Breit-Wigner formula in the s-wave scattering cross section is therefore

$$\sigma_{\ell=0}(k) = \frac{4\pi}{k^2} \frac{\Gamma_{\text{qbnd}}^2/4}{(E - E_{\text{qbnd}})^2 + \Gamma_{\text{qbnd}}^2/4} \quad (5.14)$$

where Γ_{qbnd} denotes the the full width at half maximum decay width.

For the Li-Cs system (Fig. 5.5) with $M/m = 22.17$ and a scattering length close to the resonance position $a_+^{(1)}$ ($1/k_F a = +1.87 \gtrsim 1/k_F a_+^{(1)} = +1.85$) the scattering cross-section shows a maximum at positive energies close to E_F . Accordingly the scattering phase shift (and its cotangent) rises from below (above) and crosses $\pi/2$ (zero), as expected. However, the width $\Gamma_{\text{qbnd}} > E_{\text{qbnd}}$ is still large such that we cannot assign this to a quasibound state, yet. Instead we only find enhanced scattering between the impurities which could lead to a greater mean-field shift in the impurity spectra. The lifetime of states trapped behind the repulsive barrier depends on its height which could be tuned by changing the mass ratio M/m which

scales linearly with the barrier height. Increasing the mass ratio, we find quasi-bound states for values of $M/m \gtrsim 40$. In the inset of Fig. 5.5 the calculation has been performed hypothetically for twice the Li-Cs mass ratio $M/m = 44.33$ and $1/k_F a = +2.780 \gtrsim 1/k_F a_+^{(1)} = +2.777$. In this regime, the in-medium Efimov state can live on behind the barrier and can form a well-defined quasibound state with $\Gamma_{\text{qbnd}} < E_{\text{qbnd}}$.

Experimentally, it does not seem feasible to observe quasibound states in a system of Cs impurities immersed in a Li Fermi sea. According to our calculations even the large Li-Cs mass ratio is not large enough to support long-lived states behind the repulsive barrier. More generally, quasibound states could be detected as a mean-field shift in the polaron spectrum (on the order of a few percent [Naidon, 2018]) or by radio-frequency association [Lompe et al., 2010].

Conclusions

In this chapter we have computed the scattering properties of two heavy Cs impurities immersed in a Li Fermi sea employing the Born-Oppenheimer approximation. We solved the Schrödinger using the variable phase method allowing us to extract the scattering phase shift and the induced scattering length in dependence of the interspecies scattering length. For very weak attractions on the order of $k_F a \approx 0.01$ the induced scattering length is similar to results from perturbation theory with an additional, small contribution arising from the bound states, consistent with experimental findings [DeSalvo et al., 2019; Edri et al., 2020]. On the other hand, our results are the first findings of resonant behavior in the induced scattering length in the Fermi polaron scenario. The resonances are found at interspecies scattering lengths at which the in-medium Efimov states cross the scattering continuum. For increasing positive interspecies scattering lengths the in-medium Efimov states can be shifted to positive energies to form quasiparticles behind the repulsive barrier of the induced interaction potential. Despite the large Li-Cs mass ratio, we only find long-lived quasibound states for $M/m \gtrsim 40$ making an experimental observation in our system infeasible. In general, beyond the current results, one might increase the impurity concentration where the induced interaction potential is simply the sum over pairwise interactions [Nishida, 2009; Bulgac and Wirzba, 2001]. In a finite temperature gas of impurities with thermal wavevector $k \sim \lambda_{dB}^{-1} = \sqrt{mk_B T}/2\pi$ an enhanced mean-field energy shift would be expected for $T \approx E_{\text{qbnd}}$.

Chapter 6

Conclusions

In this thesis we have presented a series of experimental and theoretical investigations from few-body Efimov physics to many-body Bose and Fermi polarons in an ultracold mixture of ${}^6\text{Li} - {}^{133}\text{Cs}$ with a large mass ratio.

Starting from an existing experimental apparatus which allowed for studies of Cs-Cs-Li Efimov trimers in the thermal regime, we reconstructed and improved the setup for an optimized production of quantum degenerate gases with the aim of creating polarons. Improved sub-Doppler laser cooling of ${}^{133}\text{Cs}$ via degenerate Raman sideband cooling and of ${}^6\text{Li}$ via gray molasses cooling with temperatures of $T_{\text{Cs}} < 1 \mu\text{K}$ and $T_{\text{Li}} = 42 \mu\text{K}$ allow for better initial conditions before further evaporative cooling. Loading of ${}^6\text{Li}$ and ${}^{133}\text{Cs}$ atoms into existing optical dipole traps has been improved and a new microtrap for tight confinement of ${}^6\text{Li}$ atoms in a ${}^{133}\text{Cs}$ BEC has been implemented. For the probing of polarons, the radio-frequency spectroscopy setup for ${}^6\text{Li}$ has been upgraded to allow for arbitrary waveform generation and Rabi frequencies of up to 13.5(1) kHz in the $\text{Li}|1\rangle \rightarrow \text{Li}|2\rangle$ transition. A microwave setup has been implemented for ${}^{133}\text{Cs}$ to drive $F = 3 \rightarrow F = 4$ transitions. We have used the latter to improve on the compensation of stray magnetic fields.

With the upgrade of the experimental apparatus we have presented our route towards the creation of Bose polarons. We have presented the realization of a ${}^{133}\text{Cs}$ BEC at high magnetic fields around $B = 895 \text{ G}$. We trap ${}^{133}\text{Cs}$ atoms in a magnetically levitated reservoir trap and make use of the dimple trick followed by evaporative cooling. In this way we achieve ${}^{133}\text{Cs}$ BECs with $N = 1 - 2 \times 10^4$ atoms. A characterization of the dimple trick revealed a small gain of < 4 in local phase-space density. An improvement of the dimple trick by a change of the relative volumes between reservoir trap and dimple trap is suggested to achieve BECs with higher atoms numbers. We have presented our preparation scheme of ultracold ${}^6\text{Li}$ atoms

with high evaporation efficiencies of up to $\gamma = 8.8$ in the dimple trap. This allows for the creation of molecular BECs with up to $N = 1 \times 10^5$ molecules. The ${}^6\text{Li}$ atoms can furthermore be transferred into the microtrap where they serve as impurities in the Bose polaron scenario. For mixing the ${}^6\text{Li}$ impurities with the ${}^{133}\text{Cs}$ BEC we have designed and proposed an experimental scheme which overcomes many of the challenges related to the high ${}^6\text{Li} - {}^{133}\text{Cs}$ mass ratio from efficient dipole trap loading to the spatial overlap of ${}^6\text{Li}$ and ${}^{133}\text{Cs}$ at ultralow temperatures. With this scheme we expect to be able to map out the polaron energy by means of radio-frequency spectroscopy.

On the theoretical side we have studied a system of two heavy ${}^{133}\text{Cs}$ atoms and one light ${}^6\text{Li}$ atom in the Born-Oppenheimer approximation. The fermion-mediated interactions between the two ${}^{133}\text{Cs}$ atoms give rise to an infinite series of Efimov three-body bound states. Including the intraspecies scattering length in the model, we have seen that it determines the three-body parameter and therefore the scaling factor between consecutive states. In the energy spectrum we have found a crossover between regions dominated by the short-range vdW potential and the long-range $-1/R^2$ potential when $a_{\text{CsCs}} \approx R_{\text{vdW}}$. Replacing the single ${}^6\text{Li}$ atom by a whole ${}^6\text{Li}$ Fermi sea we have found that bound state formation is weakened and eventually suppressed for sufficiently high k_F . The suppression of bound states is explained by a build-up of oscillations in the effective interaction potential. This leads to a violation of the discrete scaling law which is, however, replaced by a modified version including k_F as an additional length scale. Although our model only gives qualitative results within the Born-Oppenheimer approximation, it provides intuitive access to Efimov physics in a mass-imbalanced system. A better understanding may be gained by mapping out the bound state energies in the Fermi sea experimentally via atom-loss spectroscopy. In the ${}^6\text{Li} - {}^{133}\text{Cs}$ system the experiments could be performed in the vicinity of the s-wave Feshbach resonances at $B = 843$ G and $B = 889$ G, featuring a negative and positive intraspecies scattering length, respectively.

In addition to the bound state energies we have also investigated the scattering states of two heavy Cs atoms in a Li Fermi sea, or two Fermi polarons, in the Born-Oppenheimer approximation. We have calculated the scattering phase shift and the induced scattering length between the two Cs atoms mediated by the Fermi sea. For weak interspecies attractive interactions, the induced interaction is also weakly attractive consistent with recent experiments [DeSalvo et al., 2019; Edri et al., 2020]. However, for strong interspecies interaction, we have found resonances in the induced scattering length leading to a sign change. The position of these resonances is determined by the values of the interspecies scattering lengths where

the bound states cross the scattering continuum. This demonstrates the different nature of two attractive impurities in a Fermi sea compared to the RKKY interaction of between nuclear spins in an electron gas. While the long-range potential has the same oscillating form, the bound states arising in the short-range $-1/R^2$ potential alter the induced interactions. Finally, we have studied if the bound states can turn into quasibound states trapped behind the repulsive barrier of the interaction potential. Our calculations suggest that long-lived states can only form in systems with even larger mass ratios $M/m \gtrsim 40$. Experimentally, induced interactions between Fermi polarons may be measured by mapping out the impurity concentration dependence of the RF spectrum [Fritsche et al., 2021]. For increasing concentration and sufficiently low temperatures the impurity will eventually take over the role of the majority particle and form Bose polarons.

Appendix A

Appendix

Optical setup of Cs dimple trap

The optical setup of an alternative dimple trap for ^{133}Cs is shown in Fig. A.1. Since the currently implemented dimple trap (see Fig. 2.10) is used for both ^6Li and ^{133}Cs changes of the optical setup, always affect both species. For test purposes, an independent Cs dimple trap has been setup, which can be used to find the optimal volume ratio between reservoir trap and dimple trap in the context of the dimple trick (Ch. 3.2.3). The optical setup of the trap is depicted in Fig. A.1. The laser source is an ytterbium fiber laser¹ with a wavelength of $\lambda = 1064\text{ nm}$ and a maximum output power of $P = 3.6\text{ W}$. The fiber collimator is held in a home-built mount made out of a massive aluminum block in order to ensure a high pointing stability. The collimated output beam with a Gaussian beam diameter of $2w = 4\text{ mm}$ is demagnified by a Gaussian telescope to 1 mm . The beam passes an acousto-optical modulator² (AOM), which is used for switching, with a diffraction efficiency of about 90% in the first order. A first polarizing beam splitter (PBS) only transmits p-polarized light, before it is split to two single-mode polarizing maintaining optical fibers³. Without the first PBS fluctuations in the laser light polarization would translate into a different power ratio after the two fibers. The light is guided to the vacuum chamber table (Fig. A.1b)) and the two fibers output light with perpendicular, linear polarization with respect to each other in order to avoid interference. In both branches of the dipole trap the light is first magnified by a Galilean telescope before it is focused into the chamber. In this way, two beams cross under an angle of slightly below 90° and the current mean beam waist amounts to $w = 74\text{ }\mu\text{m}$. The setup, however, allows for an easy change of the beam waist by

¹IPG YLD-3-1064-LP

²Gooch and Housego, 3110-197

³Fibers: Thorlabs P3-780PM-FC-10, Fiber coupler: Schäfter + Kirchhoff, $f = 8\text{ mm}$, 60FC-4-M8-08

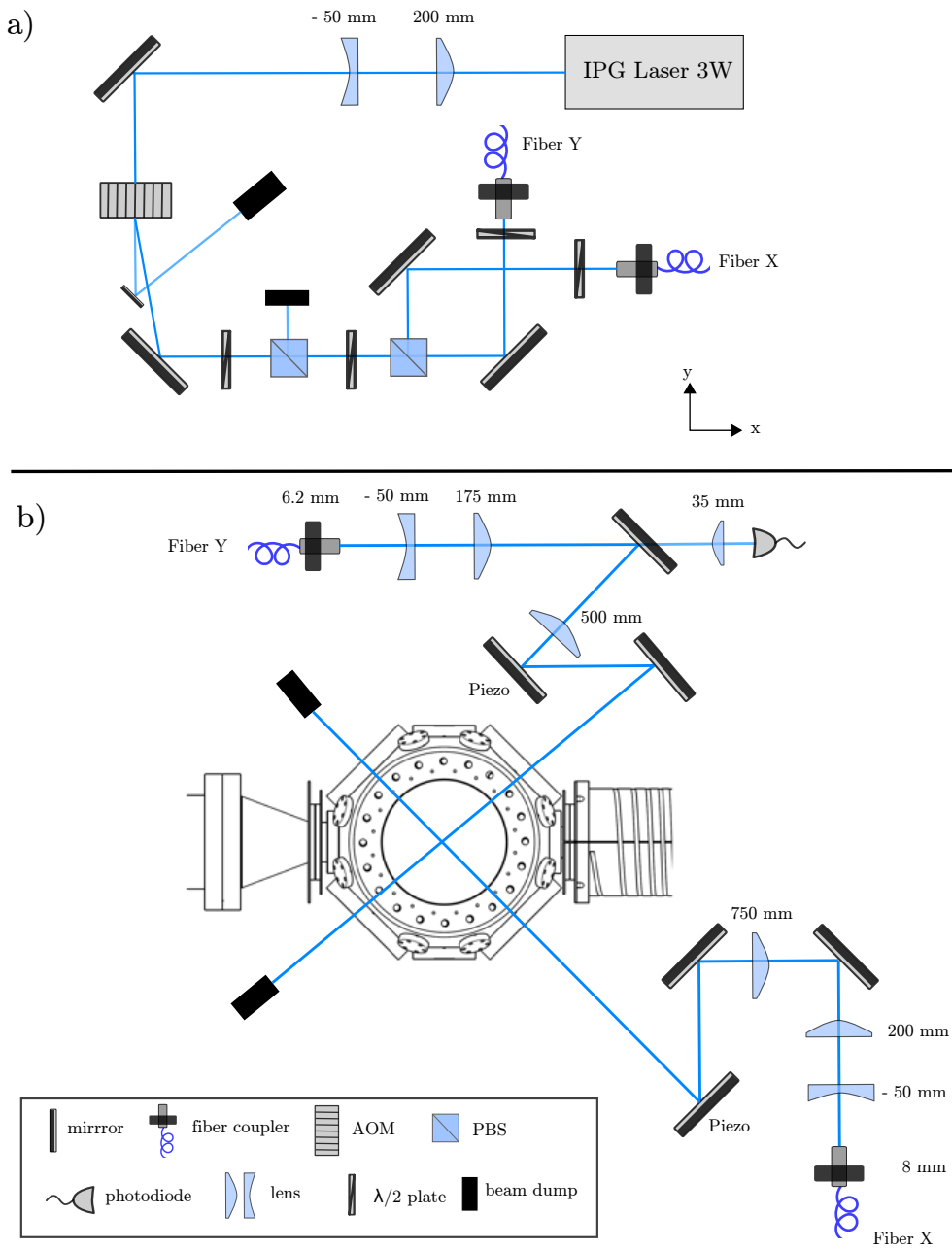


Figure A.1: Optical setup of the Cs dimple trap. a) On the laser table, the laser is switched by an AOM and guided to the vacuum chamber table via two fibers. b) The light in two optical branches is magnified and focused into the chamber under a crossing angle of nearly 90° .

replacing the second lens in the Galilean telescope which is realized in a cage mount. The laser power is stabilized by picking up light on a photodiode⁴ behind a mirror and feeding it into a home-built PID controller which controls the AOM RF power. In each branch of the dipole trap, a piezo mirror holder is implemented which can be used for fine adjustment of the beam position or to excite dipole oscillations of the atomic cloud to e.g. measure trap frequencies and map out the beam waist.

⁴Thorlabs PDA30B-EC, Ge amplified detector

Bibliography

- Anderson, M. H., Ensher, J. R., Matthews, M. R., Wieman, C. E., and Cornell, E. A. (1995). Observation of bose-einstein condensation in a dilute atomic vapor. *Science*, 269(5221):198–201.
- Arias, A. (2014). A reservoir optical dipole trap for creating a bose-einstein condensate of cs. Master’s thesis, Ruperto-Carola-University of Heidelberg.
- Arlt, J., Bance, P., Hopkins, S., Martin, J., Webster, S., Wilson, A., Zetie, K., and Foot, C. J. (1998). Suppression of collisional loss from a magnetic trap. *Journal of Physics B: Atomic, Molecular and Optical Physics*, 31(7):L321–L327.
- Barontini, G., Weber, C., Rabatti, F., Catani, J., Thalhammer, G., Inguscio, M., and Minardi, F. (2009). Observation of heteronuclear atomic efimov resonances. *Phys. Rev. Lett.*, 103:043201.
- Barontini, G., Weber, C., Rabatti, F., Catani, J., Thalhammer, G., Inguscio, M., and Minardi, F. (2010). Erratum: Observation of heteronuclear atomic efimov resonances [phys. rev. lett. 103, 043201 (2009)]. *Phys. Rev. Lett.*, 104:059901.
- Bartenstein, M., Altmeyer, A., Riedl, S., Geursen, R., Jochim, S., Chin, C., Denschlag, J. H., Grimm, R., Simoni, A., Tiesinga, E., Williams, C. J., and Julienne, P. S. (2005). Precise determination of ${}^6\text{Li}$ cold collision parameters by radio-frequency spectroscopy on weakly bound molecules. *Phys. Rev. Lett.*, 94:103201.
- Bedaque, P. F., Braaten, E., and Hammer, H.-W. (2000). Three-body recombination in bose gases with large scattering length. *Phys. Rev. Lett.*, 85:908–911.
- Bell, S. C., Junker, M., Jasperse, M., Turner, L. D., Lin, Y.-J., Spielman, I. B., and Scholten, R. E. (2010). A slow atom source using a collimated effusive oven and a single-layer variable pitch coil zeeman slower. *Review of Scientific Instruments*, 81(1):013105.
- Berninger, M., Zenesini, A., Huang, B., Harm, W., Nägerl, H.-C., Ferlaino, F., Grimm, R., Julienne, P. S., and Hutson, J. M. (2011). Universality of the

- three-body parameter for efimov states in ultracold cesium. *Phys. Rev. Lett.*, 107:120401.
- Berninger, M., Zenesini, A., Huang, B., Harm, W., Nägerl, H.-C., Ferlaino, F., Grimm, R., Julienne, P. S., and Hutson, J. M. (2013). Feshbach resonances, weakly bound molecular states, and coupled-channel potentials for cesium at high magnetic fields. *Phys. Rev. A*, 87:032517.
- Bhaduri, R. K., Chatterjee, A., and van Zyl, B. P. (2011). An elementary exposition of the efimov effect. *American Journal of Physics*, 79(3):274–281.
- Bloch, I., Dalibard, J., and Zwerger, W. (2008). Many-body physics with ultracold gases. *Rev. Mod. Phys.*, 80:885–964.
- Bloom, R. S., Hu, M.-G., Cumby, T. D., and Jin, D. S. (2013). Tests of universal three-body physics in an ultracold bose-fermi mixture. *Phys. Rev. Lett.*, 111:105301.
- Blume, D. (2012). Few-body physics with ultracold atomic and molecular systems in traps. *Reports on Progress in Physics*, 75(4):046401.
- Bourdel, T., Khaykovich, L., Cubizolles, J., Zhang, J., Chevy, F., Teichmann, M., Tarruell, L., Kokkelmans, S. J. J. M. F., and Salomon, C. (2004). Experimental study of the bec-bcs crossover region in lithium 6. *Phys. Rev. Lett.*, 93:050401.
- Braaten, E. and Hammer, H.-W. (2001). Three-body recombination into deep bound states in a bose gas with large scattering length. *Phys. Rev. Lett.*, 87:160407.
- Braaten, E. and Hammer, H.-W. (2006). Universality in few-body systems with large scattering length. *Physics Reports*, 428(5-6):259–390.
- Braaten, E. and Hammer, H.-W. (2007). Efimov physics in cold atoms. *Annals of Physics*, 322(1):120 – 163. January Special Issue 2007.
- Bradley, C. C., Sackett, C. A., Tollett, J. J., and Hulet, R. G. (1995). Evidence of bose-einstein condensation in an atomic gas with attractive interactions. *Phys. Rev. Lett.*, 75:1687–1690.
- Bradley, C. C., Sackett, C. A., Tollett, J. J., and Hulet, R. G. (1997). Evidence of bose-einstein condensation in an atomic gas with attractive interactions [phys. rev. lett. 75, 1687 (1995)]. *Phys. Rev. Lett.*, 79:1170–1170.
- Bransden, B. and Joachain, C. (2003). *Physics of Atoms and Molecules (Second Edition)*.

- Breit, G. and Rabi, I. I. (1931). Measurement of nuclear spin. *Phys. Rev.*, 38:2082–2083.
- Bulgac, A. and Wirzba, A. (2001). Casimir interaction among objects immersed in a fermionic environment. *Phys. Rev. Lett.*, 87:120404.
- Calogero, F. (1967). *Variable Phase Approach to Potential Scattering*. Academic Press, New York.
- Camacho-Guardian, A., Peña Ardila, L. A., Pohl, T., and Bruun, G. M. (2018). Bipolarons in a bose-einstein condensate. *Phys. Rev. Lett.*, 121:013401.
- Casimir, H. (1948). On the attraction between two perfectly conducting plates royal netherlands academy of arts and sciences. *Proc. Kon. Ned. Akad. Wet.* 51, 793.
- Casteels, W., Tempere, J., and Devreese, J. T. (2013). Bipolarons and multipolarons consisting of impurity atoms in a bose-einstein condensate. *Phys. Rev. A*, 88:013613.
- Catani, J., Lamporesi, G., Naik, D., Gring, M., Inguscio, M., Minardi, F., Kantian, A., and Giamarchi, T. (2012). Quantum dynamics of impurities in a one-dimensional bose gas. *Phys. Rev. A*, 85:023623.
- Cetina, M., Jag, M., Lous, R. S., Fritsche, I., Walraven, J. T. M., Grimm, R., Levinsen, J., Parish, M. M., Schmidt, R., Knap, M., and Demler, E. (2016). Ultrafast many-body interferometry of impurities coupled to a fermi sea. *Science*, 354(6308):96–99.
- Chin, C. (2011). Universal scaling of efimov resonance positions in cold atom systems.
- Chin, C., Bartenstein, M., Altmeyer, A., Riedl, S., Jochim, S., Denschlag, J. H., and Grimm, R. (2004a). Observation of the pairing gap in a strongly interacting fermi gas. *Science*, 305(5687):1128–1130.
- Chin, C., Grimm, R., Julienne, P., and Tiesinga, E. (2010). Feshbach resonances in ultracold gases. *Rev. Mod. Phys.*, 82:1225–1286.
- Chin, C., Vuletić, V., Kerman, A. J., and Chu, S. (2000). High resolution feshbach spectroscopy of cesium. *Phys. Rev. Lett.*, 85:2717–2720.
- Chin, C., Vuletić, V., Kerman, A. J., Chu, S., Tiesinga, E., Leo, P. J., and Williams, C. J. (2004b). Precision feshbach spectroscopy of ultracold cs_2 . *Phys. Rev. A*, 70:032701.

- Chu, S., Bjorkholm, J. E., Ashkin, A., and Cable, A. (1986). Experimental observation of optically trapped atoms. *Phys. Rev. Lett.*, 57:314–317.
- Combescot, R., Recati, A., Lobo, C., and Chevy, F. (2007). Normal state of highly polarized fermi gases: Simple many-body approaches. *Phys. Rev. Lett.*, 98:180402.
- Courteille, P., Freeland, R. S., Heinzen, D. J., van Abeelen, F. A., and Verhaar, B. J. (1998). Observation of a feshbach resonance in cold atom scattering. *Phys. Rev. Lett.*, 81:69–72.
- Dalibard, J. (1999). Collisional dynamics of ultra-cold atomic gases. In Inguscio, M., Stringari, S., and Wieman, C. E., editors, *Proceedings of the International School of Physics Enrico Fermi*, volume Course CXL, page 321. IOS Press, Amsterdam.
- Davis, K. B., Mewes, M. O., Andrews, M. R., van Druten, N. J., Durfee, D. S., Kurn, D. M., and Ketterle, W. (1995). Bose-einstein condensation in a gas of sodium atoms. *Phys. Rev. Lett.*, 75:3969–3973.
- DeMarco, B. and Jin, D. S. (1999). Onset of fermi degeneracy in a trapped atomic gas. *Science*, 285(5434):1703–1706.
- Demtröder, W. (2016). *Experimentalphysik 3: Atome, Moleküle und Festkörper*. Springer-Lehrbuch. Springer Berlin Heidelberg.
- DePue, M. T., McCormick, C., Winoto, S. L., Oliver, S., and Weiss, D. S. (1999). Unity occupation of sites in a 3d optical lattice. *Phys. Rev. Lett.*, 82:2262–2265.
- DeSalvo, B. J., Patel, K., Cai, G., and Chin, C. (2019). Observation of fermion-mediated interactions between bosonic atoms. *Nature*, 568(7750):61–64.
- Devreese, J. T. and Alexandrov, A. S. (2009). Fröhlich polaron and bipolaron: recent developments. *Reports on Progress in Physics*, 72(6):066501.
- Drewsen, M., Laurent, P., Nadir, A., Santarelli, G., Clairon, A., Castin, Y., Grison, D., and Salomon, C. (1994). Investigation of sub-doppler cooling effects in a cesium magneto-optical trap. *Applied Physics B*, 59(3):283–298.
- Edri, H., Raz, B., Matzliah, N., Davidson, N., and Ozeri, R. (2020). Observation of spin-spin fermion-mediated interactions between ultracold bosons. *Physical Review Letters*, 124(16):163401.
- Efimov, V. (1970). Energy levels arising from resonant two-body forces in a three-body system. *Physics Letters B*, 33(8):563 – 564.

- Eismann, U., Khaykovich, L., Laurent, S., Ferrier-Barbut, I., Rem, B. S., Grier, A. T., Delehay, M., Chevy, F., Salomon, C., Ha, L.-C., and Chin, C. (2016). Universal loss dynamics in a unitary bose gas. *Phys. Rev. X*, 6:021025.
- Endo, S., Naidon, P., and Ueda, M. (2011). Universal physics of 2+1 particles with non-zero angular momentum. *Few-Body Systems*, 51(2-4):207–217.
- Esry, B. D. and Greene, C. H. (2006). A ménage à trois laid bare. *Nature*, 440(7082):289–290.
- Esry, B. D., Greene, C. H., and Burke, J. P. (1999). Recombination of three atoms in the ultracold limit. *Phys. Rev. Lett.*, 83:1751–1754.
- Ferlaino, F., Zenesini, A., Berninger, M., Huang, B., Nägerl, H. C., and Grimm, R. (2011). Efimov resonances in ultracold quantum gases. *Few-Body Systems*, 51(2-4):113–133.
- Filzinger, M. (2018). Improved manipulation and detection of an ultracold li-cs mixture towards the investigation of the bose polaron. Master’s thesis, Ruperto-Carola-University of Heidelberg.
- Flambaum, V. V., Gribakin, G. F., and Harabati, C. (1999). Analytical calculation of cold-atom scattering. *Phys. Rev. A*, 59:1998–2005.
- Fonseca, A. C., Redish, E. F., and Shanley, P. (1979). Efimov effect in an analytically solvable model. *Nuclear Physics A*, 320(2):273 – 288.
- Freund, R. (2019). Switching polarity of a magnetic gradient field using an h bridge in an ultracold mixture of lithium and caesium. Bachelor’s Thesis, Ruperto-Carola-University of Heidelberg.
- Fröhlich, H. (1954). Electrons in lattice fields. *Advances in Physics*, 3(11):325–361.
- Friedel, J. (1952). Xiv. the distribution of electrons round impurities in monovalent metals. *The London, Edinburgh, and Dublin Philosophical Magazine and Journal of Science*, 43(337):153–189.
- Fritsche, I., Baroni, C., Dobler, E., Kirilov, E., Huang, B., Grimm, R., Bruun, G. M., and Massignan, P. (2021). Stability and breakdown of fermi polarons in a strongly interacting fermi-bose mixture. *Physical Review A*, 103(5):053314.
- Gehm, M. E. (2003). Properties of 6li.
- Gensemer, S. D. and Jin, D. S. (2001). Transition from collisionless to hydrodynamic behavior in an ultracold fermi gas. *Phys. Rev. Lett.*, 87:173201.

- Gerken, M. (2016). Gray molasses cooling of lithium-6 towards a degenerate fermi gas. Master's thesis, Ruperto-Carola-University of Heidelberg.
- Gerken, M. (2022). *Exploring p-wave resonances in ultracold lithium and lithium-cesium mixtures*. PhD thesis, Ruperto-Carola-University of Heidelberg.
- Gerken, M., Tran, B., Häfner, S., Tiemann, E., Zhu, B., and Weidemüller, M. (2019). Observation of dipolar splittings in high-resolution atom-loss spectroscopy of ${}^6\text{Li}$ p -wave feshbach resonances. *Phys. Rev. A*, 100:050701.
- Gribakin, G. F. and Flambaum, V. V. (1993). Calculation of the scattering length in atomic collisions using the semiclassical approximation. *Phys. Rev. A*, 48:546–553.
- Grimm, R., Weidemüller, M., and Ovchinnikov, Y. B. (2000). *Optical dipole traps for neutral atoms*, volume 42 of *ADVANCES IN ATOMIC MOLECULAR, AND OPTICAL PHYSICS, VOL. 42*, pages 95–170. Advances In Atomic Molecular and Optical Physics.
- Gross, N., Shotan, Z., Kokkelmans, S., and Khaykovich, L. (2009). Observation of universality in ultracold ${}^7\text{Li}$ three-body recombination. *Phys. Rev. Lett.*, 103:163202.
- Grusdt, F. and Demler, E. (2015). New theoretical approaches to bose polarons.
- Guery-Odelin, D., Soding, J., Desbiolles, P., and Dalibard, J. (1998). Is bose-einstein condensation of atomic cesium possible? *EUROPHYSICS LETTERS*, 44(1):25–30.
- Hadzibabic, Z., Stan, C. A., Dieckmann, K., Gupta, S., Zwierlein, M. W., Görlitz, A., and Ketterle, W. (2002). Two-species mixture of quantum degenerate bose and fermi gases. *Phys. Rev. Lett.*, 88:160401.
- Häfner, S., Ulmanis, J., Kuhnle, E. D., Wang, Y., Greene, C. H., and Weidemüller, M. (2017). Role of the intraspecies scattering length in the efimov scenario with large mass difference. *Phys. Rev. A*, 95:062708.
- He, J., dong Yang, B., jie Cheng, Y., cai Zhang, T., and min Wang, J. (2011). Extending the trapping lifetime of single atom in a microscopic far-off-resonance optical dipole trap. *Frontiers of Physics*, 6(3):262–270.
- Heck, R. (2012). All-optical formation of an ultracold gas of fermionic lithium close to quantum degeneracy. Master's thesis, Ruperto-Carola-University of Heidelberg.
- Häfner, S. (2017). *From two-body to many-body physics in an ultracold Bose-Fermi mixture of Li and Cs atoms*. PhD thesis, Ruperto-Carola-University of Heidelberg.

- Higgs, P. (1964). Broken symmetries, massless particles and gauge fields. *PHYSICS LETTERS*, 12(2):132–133.
- Hopkins, S. A., Webster, S., Arlt, J., Bance, P., Cornish, S., Maragò, O., and Foot, C. J. (2000). Measurement of elastic cross section for cold cesium collisions. *Phys. Rev. A*, 61:032707.
- Hu, M.-G., Van de Graaff, M. J., Kedar, D., Corson, J. P., Cornell, E. A., and Jin, D. S. (2016). Bose polarons in the strongly interacting regime. *Phys. Rev. Lett.*, 117:055301.
- Huang, K. and Yang, C. N. (1957). Quantum-mechanical many-body problem with hard-sphere interaction. *Phys. Rev.*, 105:767–775.
- Hung, C.-L., Zhang, X., Gemelke, N., and Chin, C. (2008). Accelerating evaporative cooling of atoms into bose-einstein condensation in optical traps. *Phys. Rev. A*, 78:011604.
- Hunklinger, S. (2017). *Festkörperphysik*. De Gruyter Oldenbourg.
- Inouye, S., Andrews, M. R., Stenger, J., Miesner, H.-J., Stamper-Kurn, D. M., and Ketterle, W. (1998). Observation of feshbach resonances in a bose-einstein condensate. *Nature*, 392(6672):151–154.
- Jochim, S. (2004). *Bose-Einstein Condensation of Molecules*. PhD thesis, Leopold-Franzens-Universität Innsbruck.
- Jochim, S., Bartenstein, M., Altmeyer, A., Hendl, G., Riedl, S., Chin, C., Denschlag, J. H., and Grimm, R. (2003). Bose-einstein condensation of molecules. *Science*, 302(5653):2101–2103.
- Jørgensen, N. B., Wacker, L., Skalmstang, K. T., Parish, M. M., Levinsen, J., Christensen, R. S., Bruun, G. M., and Arlt, J. J. (2016). Observation of attractive and repulsive polarons in a bose-einstein condensate. *Phys. Rev. Lett.*, 117:055302.
- Kartavtsev, O. I. and Malykh, A. V. (2007). Low-energy three-body dynamics in binary quantum gases. *Journal of Physics B: Atomic, Molecular and Optical Physics*, 40(7):1429–1441.
- Kastberg, A., Phillips, W. D., Rolston, S. L., Spreuw, R. J. C., and Jessen, P. S. (1995). Adiabatic cooling of cesium to 700 nk in an optical lattice. *Phys. Rev. Lett.*, 74:1542–1545.

- Kerman, A. J., Vuletić, V., Chin, C., and Chu, S. (2000). Beyond optical molasses: 3d raman sideband cooling of atomic cesium to high phase-space density. *Phys. Rev. Lett.*, 84:439–442.
- Ketterle, W. and Druten, N. V. (1996). Evaporative cooling of trapped atoms. volume 37 of *Advances In Atomic, Molecular, and Optical Physics*, pages 181–236. Academic Press.
- Ketterle, W., Durfee, D. S., and Stamper-Kurn, D. M. (1999). Making, probing and understanding Bose-Einstein condensates. In Inguscio, M., Stringari, S., and Wieman, C., editors, *Proceedings of the International School of Physics "Enrico Fermi"*, Course CXL, pages 67–176. IOS Press, Amsterdam.
- Klaus, L. (2019). Design and construction of an optical microtrap to study the polaron scenario in an ultracold li-cs mixture. Master’s thesis, Ruperto-Carola-University of Heidelberg.
- Knoop, S., Ferlaino, F., Mark, M., Berninger, M., Schöbel, H., Nägerl, H.-C., and Grimm, R. (2009). Observation of an efimov-like trimer resonance in ultracold atom–dimer scattering. *Nature Physics*, 5(3):227–230.
- Köhler, T., Góral, K., and Julienne, P. S. (2006). Production of cold molecules via magnetically tunable Feshbach resonances. *Rev. Mod. Phys.*, 78:1311–1361.
- Kohstall, C., Zaccanti, M., Jag, M., Trenkwalder, A., Massignan, P., Bruun, G. M., Schreck, F., and Grimm, R. (2012). Metastability and coherence of repulsive polarons in a strongly interacting fermi mixture. *Nature*, 485(7400):615–618.
- Kondo, J. (1964). Resistance Minimum in Dilute Magnetic Alloys. *Progress of Theoretical Physics*, 32(1):37–49.
- Koschorreck, M., Pertot, D., Vogt, E., Fröhlich, B., Feld, M., and Köhl, M. (2012). Attractive and repulsive fermi polarons in two dimensions. *Nature*, 485(7400):619–622.
- Kraemer, T., Mark, M., Waldburger, P., Danzl, J. G., Chin, C., Engeser, B., Lange, A. D., Pilch, K., Jaakkola, A., Nägerl, H.-C., and Grimm, R. (2006). Evidence for efimov quantum states in an ultracold gas of caesium atoms. *Nature*, 440(7082):315–318.
- Landau, L. D. (1933). Über Die Bewegung der Elektronen in Kristallgitter. *Phys. Z. Sowjetunion*, 3:644–645.
- LeBlanc, L. J. and Thywissen, J. H. (2007). Species-specific optical lattices. *Phys. Rev. A*, 75:053612.

- Levinsen, J., Parish, M. M., and Bruun, G. M. (2015). Impurity in a bose-einstein condensate and the efimov effect. *Phys. Rev. Lett.*, 115:125302.
- Lompe, T., Ottenstein, T. B., Serwane, F., Wenz, A. N., Zürn, G., and Jochim, S. (2010). Radio-frequency association of efimov trimers. *Science*, 330(6006):940–944.
- Luiten, O. J., Reynolds, M. W., and Walraven, J. T. M. (1996). Kinetic theory of the evaporative cooling of a trapped gas. *Phys. Rev. A*, 53:381–389.
- Ma, Z.-Y., Foot, C. J., and Cornish, S. L. (2004). Optimized evaporative cooling using a dimple potential: an efficient route to bose–einstein condensation. *Journal of Physics B: Atomic, Molecular and Optical Physics*, 37(15):3187–3195.
- MacNeill, D. J. and Zhou, F. (2011). Pauli blocking effect on efimov states near a feshbach resonance. *Phys. Rev. Lett.*, 106:145301.
- Martin, A. G., Helmerson, K., Bagnato, V. S., Lafyatis, G. P., and Pritchard, D. E. (1988). rf spectroscopy of trapped neutral atoms. *Phys. Rev. Lett.*, 61:2431–2434.
- Massignan, P., Zaccanti, M., and Bruun, G. M. (2014). Polarons, dressed molecules and itinerant ferromagnetism in ultracold fermi gases. *Reports on Progress in Physics*, 77(3):034401.
- Merzbacher, E. (1998). *Quantum Mechanics*. Wiley.
- Moerdijk, A. J., Verhaar, B. J., and Axelsson, A. (1995). Resonances in ultracold collisions of ${}^6\text{Li}$, ${}^7\text{Li}$, and ${}^{23}\text{Na}$. *Phys. Rev. A*, 51:4852–4861.
- Monroe, C. R., Cornell, E. A., Sackett, C. A., Myatt, C. J., and Wieman, C. E. (1993). Measurement of cs-cs elastic scattering at $t=30 \mu\text{k}$. *Phys. Rev. Lett.*, 70:414–417.
- Mudrich, M., Kraft, S., Singer, K., Grimm, R., Mosk, A., and Weidemüller, M. (2002). Sympathetic cooling with two atomic species in an optical trap. *Phys. Rev. Lett.*, 88:253001.
- Mukherjee, K., Mistakidis, S. I., Majumder, S., and Schmelcher, P. (2020). Induced interactions and quench dynamics of bosonic impurities immersed in a fermi sea. *Physical Review A*, 102(5):053317.
- Naidon, P. (2018). Two impurities in a bose–einstein condensate: From yukawa to efimov attracted polarons. *Journal of the Physical Society of Japan*, 87(4):043002.
- Naidon, P. and Endo, S. (2017). Efimov physics: a review. *Reports on Progress in Physics*, 80(5):056001.

- Nakajima, S., Horikoshi, M., Mukaiyama, T., Naidon, P., and Ueda, M. (2010). Nonuniversal efimov atom-dimer resonances in a three-component mixture of ${}^6\text{Li}$. *Phys. Rev. Lett.*, 105:023201.
- Nascimbène, S., Navon, N., Jiang, K. J., Tarruell, L., Teichmann, M., McKeever, J., Chevy, F., and Salomon, C. (2009). Collective oscillations of an imbalanced fermi gas: Axial compression modes and polaron effective mass. *Phys. Rev. Lett.*, 103:170402.
- Neiczner, M. (2018). Efficient creation of a molecular bose-einstein condensate of lithium-6 using a spatially modulated dipole trap. Master's thesis, Ruperto-Carola-University of Heidelberg.
- Ness, G., Shkedrov, C., Florshaim, Y., Diessel, O. K., von Milczewski, J., Schmidt, R., and Sagi, Y. (2020). Observation of a smooth polaron-molecule transition in a degenerate fermi gas. *Phys. Rev. X*, 10:041019.
- Nishida, Y. (2009). Casimir interaction among heavy fermions in the bcs-bec crossover. *Phys. Rev. A*, 79:013629.
- Nygaard, N. G. and Zinner, N. T. (2014). Efimov three-body states on top of a fermi sea. *New Journal of Physics*, 16(2):023026.
- Olson, A. J., Niffenegger, R. J., and Chen, Y. P. (2013). Optimizing the efficiency of evaporative cooling in optical dipole traps. *Phys. Rev. A*, 87:053613.
- Ospelkaus, S., Ospelkaus, C., Dinter, R., Fuchs, J., Nakat, M., Sengstock, K., and Bongs, K. (2007). Degenerate k-rb fermi-bose gas mixtures with large particle numbers. *Journal of Modern Optics*, 54(5):661–673.
- Ouerdane, H., Jamieson, M. J., Vranceanu, D., and Cavagnero, M. J. (2003). The variable phase method used to calculate and correct scattering lengths. *Journal of Physics B: Atomic, Molecular and Optical Physics*, 36(19):4055–4063.
- Palzer, S., Zipkes, C., Sias, C., and Köhl, M. (2009). Quantum transport through a tonks-girardeau gas. *Phys. Rev. Lett.*, 103:150601.
- Pekar, S. (1946). Autolocalization of the electron in an inertially polarizable dielectric medium. *Zh. Eksp. Teor. Fiz*, 16:335.
- Pethick, C. J. and Smith, H. (2002). *Bose-Einstein Condensation in Dilute Gases*. Cambridge University Press, 2 edition.
- Petrov, D. S. (2003). Three-body problem in fermi gases with short-range interparticle interaction. *Phys. Rev. A*, 67:010703.

- Petrov, D. S. (2012). *The few-atom problem. in Many-Body Physics with Ultracold Gases: Lecture Notes of the Les Houches SummerSchool: Volume 94, July 2010.* Oxford University Press.
- Petrov, D. S., Salomon, C., and Shlyapnikov, G. V. (2004). Weakly bound dimers of fermionic atoms. *Phys. Rev. Lett.*, 93:090404.
- Phillips, W. D. and Metcalf, H. (1982). Laser deceleration of an atomic beam. *Phys. Rev. Lett.*, 48:596–599.
- Pillai, M., Goglio, J., and Walker, T. (2012). Matrix numerov method for solving schrödinger’s equation. *American Journal of Physics*, 80:1017–1019.
- Pinkse, P. W. H., Mosk, A., Weidemüller, M., Reynolds, M. W., Hijmans, T. W., and Walraven, J. T. M. (1997). Adiabatically changing the phase-space density of a trapped bose gas. *Phys. Rev. Lett.*, 78:990–993.
- Pires, R. (2014). *Efimov Resonances in an Ultracold Mixture with Extreme Mass Imbalance.* PhD thesis, Ruperto-Carola-University of Heidelberg.
- Pires, R., Repp, M., Ulmanis, J., Kuhnle, E. D., Weidemüller, M., Tiecke, T. G., Greene, C. H., Ruzic, B. P., Bohn, J. L., and Tiemann, E. (2014a). Analyzing feshbach resonances: A ${}^6\text{Li} - {}^{133}\text{Cs}$ case study. *Phys. Rev. A*, 90:012710.
- Pires, R., Ulmanis, J., Häfner, S., Repp, M., Arias, A., Kuhnle, E. D., and Weidemüller, M. (2014b). Observation of efimov resonances in a mixture with extreme mass imbalance. *Phys. Rev. Lett.*, 112:250404.
- Pitaevskii, L., Pítajevskij, L., S. Stringari, L., Stringari, S., Stringari, S., and Press, O. U. (2003). *Bose-Einstein Condensation.* International Series of Monographs on Physics. Clarendon Press.
- Pollack, S. E., Dries, D., and Hulet, R. G. (2009). Universality in three- and four-body bound states of ultracold atoms. *Science*, 326(5960):1683–1685.
- Raab, E. L., Prentiss, M., Cable, A., Chu, S., and Pritchard, D. E. (1987). Trapping of neutral sodium atoms with radiation pressure. *Phys. Rev. Lett.*, 59:2631–2634.
- Rautenberg, M. (2021). Theoretical considerations concerning the relation of the efimov scenario to fermi polarons and upgrade of a polaron experiment. Master’s thesis, Ruperto-Carola-University of Heidelberg.
- Regal, C. A. and Jin, D. S. (2003). Measurement of positive and negative scattering lengths in a fermi gas of atoms. *Phys. Rev. Lett.*, 90:230404.

- Regal, C. A., Ticknor, C., Bohn, J. L., and Jin, D. S. (2003). Creation of ultracold molecules from a fermi gas of atoms. *Nature*, 424(6944):47–50.
- Rem, B. S., Grier, A. T., Ferrier-Barbut, I., Eismann, U., Langen, T., Navon, N., Khaykovich, L., Werner, F., Petrov, D. S., Chevy, F., and Salomon, C. (2013). Lifetime of the bose gas with resonant interactions. *Phys. Rev. Lett.*, 110:163202.
- Renner, C. (2014). Design and characterization of a dual-wavelength high-resolution imaging system.
- Rentrop, T., Trautmann, A., Olivares, F. A., Jendrzejewski, F., Komnik, A., and Oberthaler, M. K. (2016). Observation of the phononic lamb shift with a synthetic vacuum. *Phys. Rev. X*, 6:041041.
- Repp, M. (2013). *Interspecies Feshbach Resonances in an Ultracold, Optically Trapped Bose-Fermi Mixture of Cesium and Lithium*. PhD thesis, Ruprecht-Karls-Universität Heidelberg, Germany.
- Repp, M., Pires, R., Ulmanis, J., Heck, R., Kuhnle, E. D., Weidemüller, M., and Tiemann, E. (2013). Observation of interspecies 6Li - 133Cs feshbach resonances. *Phys. Rev. A*, 87:010701.
- Ruderman, M. A. and Kittel, C. (1954). Indirect exchange coupling of nuclear magnetic moments by conduction electrons. *Phys. Rev.*, 96:99–102.
- Sakurai, J. J. (1993). *Modern Quantum Mechanics (Revised Edition)*. Addison Wesley, 1 edition.
- Sanayei, A. and Mathey, L. (2020). Three-body bound states of an atom in a fermi mixture. *arXiv:2007.13511*.
- Santamore, D. H. and Timmermans, E. (2008). Fermion-mediated interactions in a dilute bose-einstein condensate. *Phys. Rev. A*, 78:013619.
- Savard, T. A., O’Hara, K. M., and Thomas, J. E. (1997). Laser-noise-induced heating in far-off resonance optical traps. *Phys. Rev. A*, 56:R1095–R1098.
- Scazza, F., Valtolina, G., Massignan, P., Recati, A., Amico, A., Burchianti, A., Fort, C., Inguscio, M., Zaccanti, M., and Roati, G. (2017). Repulsive fermi polarons in a resonant mixture of ultracold ${}^6\text{Li}$ atoms. *Phys. Rev. Lett.*, 118:083602.
- Scazza, F., Zaccanti, M., Massignan, P., Parish, M. M., and Levinsen, J. (2022). Repulsive fermi and bose polarons in quantum gases.

- Scelle, R., Rentrop, T., Trautmann, A., Schuster, T., and Oberthaler, M. K. (2013). Motional coherence of fermions immersed in a bose gas. *Phys. Rev. Lett.*, 111:070401.
- Schirotzek, A., Wu, C.-H., Sommer, A., and Zwierlein, M. W. (2009). Observation of fermi polarons in a tunable fermi liquid of ultracold atoms. *Phys. Rev. Lett.*, 102:230402.
- Schlöder, U., Engler, H., Schünemann, U., Grimm, R., and Weidemüller, M. (1999). Cold inelastic collisions between lithium and cesium in a two-species magneto-optical trap. *The European Physical Journal D - Atomic, Molecular, Optical and Plasma Physics*, 7(3):331–340.
- Schmidt, R., Knap, M., Ivanov, D. A., You, J.-S., Cetina, M., and Demler, E. (2018). Universal many-body response of heavy impurities coupled to a fermi sea: a review of recent progress. *Reports on Progress in Physics*, 81(2):024401.
- Schünemann, U., Engler, H., Grimm, R., Weidemüller, M., and Zielonkowski, M. (1999). Simple scheme for tunable frequency offset locking of two lasers. *Review of Scientific Instruments*, 70(1):242–243.
- Schönhals, A. (2013). Imaging of ultracold cesium atoms at high magnetic fields. Master’s thesis, Ruperto-Carola-University of Heidelberg.
- Silber, C., Günther, S., Marzok, C., Deh, B., Courteille, P. W., and Zimmermann, C. (2005). Quantum-degenerate mixture of fermionic lithium and bosonic rubidium gases. *Phys. Rev. Lett.*, 95:170408.
- Skou, M. G., Nielsen, K. K., Skov, T. G., Morgen, A. M., Jørgensen, N. B., Camacho-Guardian, A., Pohl, T., Bruun, G. M., and Arlt, J. J. (2022). Life and death of the bose polaron.
- Skou, M. G., Skov, T. G., Jørgensen, N. B., Nielsen, K. K., Camacho-Guardian, A., Pohl, T., Bruun, G. M., and Arlt, J. J. (2021). Non-equilibrium quantum dynamics and formation of the bose polaron. *Nature Physics*, 17(6):731–735.
- Söding, J., Guéry-Odelin, D., Desbiolles, P., Ferrari, G., and Dalibard, J. (1998). Giant spin relaxation of an ultracold cesium gas. *Phys. Rev. Lett.*, 80:1869–1872.
- Spethmann, N., Kindermann, F., John, S., Weber, C., Meschede, D., and Widera, A. (2012). Dynamics of single neutral impurity atoms immersed in an ultracold gas. *Phys. Rev. Lett.*, 109:235301.

- Spiegelhalder, F. M., Trenkwalder, A., Naik, D., Kerner, G., Wille, E., Hendl, G., Schreck, F., and Grimm, R. (2010). All-optical production of a degenerate mixture of ${}^6\text{Li}$ and ${}^{40}\text{K}$ and creation of heteronuclear molecules. *Phys. Rev. A*, 81:043637.
- Stamper-Kurn, D. M., Miesner, H.-J., Chikkatur, A. P., Inouye, S., Stenger, J., and Ketterle, W. (1998). Reversible formation of a bose-einstein condensate. *Phys. Rev. Lett.*, 81:2194–2197.
- Stan, C. A. and Ketterle, W. (2005). Multiple species atom source for laser-cooling experiments. *Review of Scientific Instruments*, 76(6):063113.
- Steck, D. A. (2008). alkali numbers.
- Sun, M. and Cui, X. (2017). Enhancing the efimov correlation in bose polarons with large mass imbalance. *Phys. Rev. A*, 96:022707.
- Sun, M. and Cui, X. (2019). Efimov physics in the presence of a fermi sea. *Phys. Rev. A*, 99:060701.
- Sun, M., Zhai, H., and Cui, X. (2017). Visualizing the efimov correlation in bose polarons. *Phys. Rev. Lett.*, 119:013401.
- Tempere, J., Casteels, W., Oberthaler, M. K., Knoop, S., Timmermans, E., and Devreese, J. T. (2009). Feynman path-integral treatment of the bec-impurity polaron. *Phys. Rev. B*, 80:184504.
- Tiesinga, E., Moerdijk, A. J., Verhaar, B. J., and Stoof, H. T. C. (1992). Conditions for bose-einstein condensation in magnetically trapped atomic cesium. *Phys. Rev. A*, 46:R1167–R1170.
- Timmermans, E., Tommasini, P., Hussein, M., and Kerman, A. (1999). Feshbach resonances in atomic bose-einstein and condensates. *Physics Reports* 315 199-230.
- Treutlein, P., Chung, K. Y., and Chu, S. (2001). High-brightness atom source for atomic fountains. *Phys. Rev. A*, 63:051401.
- Tung, S.-K., Jiménez-García, K., Johansen, J., Parker, C. V., and Chin, C. (2014). Geometric scaling of efimov states in a ${}^6\text{Li}$ – ${}^{133}\text{Cs}$ mixture. *Phys. Rev. Lett.*, 113:240402.
- Tung, S.-K., Parker, C., Johansen, J., Chin, C., Wang, Y., and Julienne, P. S. (2013). Ultracold mixtures of atomic ${}^6\text{Li}$ and ${}^{133}\text{Cs}$ with tunable interactions. *Phys. Rev. A*, 87:010702.

- Ulmanis, J. (2015). *Universality and non-universality in the heteronuclear Efimov scenario with large mass imbalance*. PhD thesis, Ruperto-Carola-University of Heidelberg.
- Ulmanis, J., Häfner, S., Pires, R., Kuhnle, E. D., Wang, Y., Greene, C. H., and Weidemüller, M. (2016a). Heteronuclear efimov scenario with positive intraspecies scattering length. *Phys. Rev. Lett.*, 117:153201.
- Ulmanis, J., Häfner, S., Pires, R., Werner, F., Petrov, D. S., Kuhnle, E. D., and Weidemüller, M. (2016b). Universal three-body recombination and efimov resonances in an ultracold li-cs mixture. *Phys. Rev. A*, 93:022707.
- Ulmanis, J., Häfner, S., Kuhnle, E. D., and Weidemüller, M. (2016c). Heteronuclear Efimov resonances in ultracold quantum gases. *National Science Review*, 3(2):174–188.
- Ulmanis, J., Häfner, S., Pires, R., Kuhnle, E., Weidemüller, M., and Tiemann, E. (2015). Universality of weakly bound dimers and efimov trimers close to li-cs feshbach resonances. *New Journal of Physics*, 17.
- Vuletic, V., Chin, C., Kerman, A. J., and Chu, S. (1998). Degenerate raman sideband cooling of trapped cesium atoms at very high atomic densities. *Phys. Rev. Lett.*, 81:5768–5771.
- Wang, Y., D’Incao, J. P., and Esry, B. D. (2013). Chapter 1 - ultracold few-body systems. In Arimondo, E., Berman, P. R., and Lin, C. C., editors, *Advances in Atomic, Molecular, and Optical Physics*, volume 62 of *Advances In Atomic, Molecular, and Optical Physics*, pages 1 – 115. Academic Press.
- Wang, Y., Julienne, P., and Greene, C. H. (2015). *Few-body physics of ultracold atoms and molecules with long-range interactions*, chapter Chapter 2, pages 77–134.
- Wang, Y., Wang, J., D’Incao, J. P., and Greene, C. H. (2012). Universal three-body parameter in heteronuclear atomic systems. *Phys. Rev. Lett.*, 109:243201.
- Weber, T. (2003). *Bose-Einstein Condensation of Optically Trapped Cesium*. PhD thesis, Leopold-Franzens-Universität Innsbruck.
- Weber, T., Herbig, J., Mark, M., Nägerl, H.-C., and Grimm, R. (2003a). Three-body recombination at large scattering lengths in an ultracold atomic gas. *Phys. Rev. Lett.*, 91:123201.
- Weber, T., Herbig, J., Mark, M., Nägerl, H.-C., and Grimm, R. (2003b). Bose-einstein condensation of cesium. *Science*, 299(5604):232–235.

- Weiner, J., Bagnato, V. S., Zilio, S., and Julienne, P. S. (1999). Experiments and theory in cold and ultracold collisions. *Rev. Mod. Phys.*, 71:1–85.
- Wild, R. J., Makotyn, P., Pino, J. M., Cornell, E. A., and Jin, D. S. (2012). Measurements of tan’s contact in an atomic bose-einstein condensate. *Phys. Rev. Lett.*, 108:145305.
- Williams, J. R., Hazlett, E. L., Huckans, J. H., Stites, R. W., Zhang, Y., and O’Hara, K. M. (2009). Evidence for an excited-state efimov trimer in a three-component fermi gas. *Phys. Rev. Lett.*, 103:130404.
- Yan, Z., Patel, P. B., Mukherjee, B., Fletcher, R. J., Struck, J., and Zwierlein, M. W. (2019). Boiling a unitary fermi liquid. *Physical Review Letters*, 122(9):093401.
- Yan, Z. Z., Ni, Y., Robens, C., and Zwierlein, M. W. (2020). Bose polarons near quantum criticality. *Science*, 368(6487):190–194.
- Yukawa, H. (1955). On the Interaction of Elementary Particles. I. *Progress of Theoretical Physics Supplement*, 1:1–10.
- Zaccanti, M., Deissler, B., D’Errico, C., Fattori, M., Jona-Lasinio, M., Müller, S., Roati, G., Inguscio, M., and Modugno, G. (2009). Observation of an efimov spectrum in an atomic system. *Nature Physics*, 5(8):586–591.
- Zinner, N. T. (2013). Efimov states of heavy impurities in a bose-einstein condensate. *EPL (Europhysics Letters)*, 101(6):60009.
- Zürn, G., Lompe, T., Wenz, A. N., Jochim, S., Julienne, P. S., and Hutson, J. M. (2013). Precise characterization of ${}^6\text{Li}$ feshbach resonances using trap-sideband-resolved rf spectroscopy of weakly bound molecules. *Phys. Rev. Lett.*, 110:135301.
- Zwierlein, M. W., Stan, C. A., Schunck, C. H., Raupach, S. M. F., Gupta, S., Hadzibabic, Z., and Ketterle, W. (2003). Observation of bose-einstein condensation of molecules. *Phys. Rev. Lett.*, 91:250401.

Danksagung

Diese Arbeit wäre nicht möglich gewesen ohne die tatkräftige und tolle Unterstützung von folgenden Personen, bei denen ich mich bedanken möchte:

Mein größter Dank gebührt meinem Betreuer und Mentor Prof. Matthias Weidemüller. Von Beginn an hast Du die nötigen Rahmenbedingungen geschaffen, um in der Gruppe erfolgreich zu arbeiten, von Teilnahmen an Schools bis zu ausreichenden Finanzierungsmöglichkeiten. In jeder Diskussion hast Du es geschafft, Dinge aus anderen Blickwinkeln zu betrachten, die niemand auf dem Schirm hatte. Ich konnte früh Verantwortung übernehmen und mich unter Deiner Betreuung fachlich und menschlich weiterentwickeln.

Bei Prof. Markus Oberthaler möchte ich für die Übernahme des Zweitgutachtens herzlich bedanken.

Ich danke Prof. Tilman Enss für die Zusammenarbeit am C03 Projekt, die vielen Meetings, in denen Du Fragen geduldig beantwortet hast und mit Deiner fachlichen Expertise Diskussionen immer einen Schritt weiterbringen konntest. Ebenfalls möchte ich mich bei den weiteren C03 Kollaboratoren Prof. Manfred Salmhofer und Dr. Moritz Drescher für eine gute Zusammenarbeit bedanken.

I thank JProf. Lauriane Chomaz for your input to the experiment since last year. Your analytical thinking is remarkable and having you on the team is such a big gain. Best wishes for the future!

Bei Juris Ulmanis und Stephan Häfner bedanke ich mich für die Einweisung in das Experiment. Wichtige Fähigkeiten, angefangen vom Einkoppeln optischer Fasern bis zu trick shots beim Tischkicker habe ich von Euch gelernt!

My fellow lab mates Manuel Gerken for your great intuition and problem solving skills in the lab, Eleonora Lippi for your optimism and determination, and Bing Zhu for the support in the first years. It was great to work in such a friendly atmosphere

ACKNOWLEDGEMENTS

and I also enjoyed our activities outside the lab.

Den neuen Doktoranden Tobias Krom und Michael Rautenberg danke ich für die Verbesserungsvorschläge an dieser Arbeit und wünsche eine erfolgreiche Zukunft am Experiment. Michael möchte ich besonders danken für Deinen Input in den gemeinsamen Projekten, die Du durch Deine beachtlichen Programmier- und Laborfähigkeiten weiterbringen konntest.

Ich danke den Master- und Bachelorstudent*innen Robert Freund, Melina Filzinger, Lauritz Klaus, Marcia Kroker, Jonas Matthies und Markus Neiczer für die Projekte und Verbesserungen am Experiment.

Ebenso möchte ich bei allen QD Gruppenmitgliedern bedanken, dafür, dass sie stets ein offenes Ohr haben und für eine tolle Arbeitsatmosphäre.

Bei den mechanischen und elektronischen Werkstätten des physikalischen Instituts möchte ich mich für die immer freundliche Unterstützung bedanken.

Für die Hilfe bei jeglichen Verwaltungsaufgaben danke ich besonders Claudia Krämer und den Mitarbeiterinnen in Einkauf und Verwaltung.

Ich hätte es nicht bis hierher geschafft ohne meine Freunde, die ich in Heidelberg kennenlernen durfte. Während des Studiums war mit Euch kein fachliches Problem unlösbar und die gemeinsame Zeit außerhalb der Uni bleibt für mich unvergesslich. Nicht unerwähnt kann ich lassen: Alex, Alex, Ale, Ben, Chris, Domi, Fine, Flo, Hannah, Jan Hendrik, Katja, Nele und Vivi. Vielen Dank!

Zuletzt danke ich meiner Familie, die mich zu jedem Zeitpunkt unterstützt hat und immer für mich da ist.